

Control of the colloidal deposition of cellulose nanocrystal films

Alican GENÇER

Supervisor:

Prof. Wim Thielemans

Members of the Examination Committee:

Prof. Pavlik Lettinga (Chair)

Prof. Jan K.G. Dhont

Prof. Bart Goderis

Prof. Christian Clasen

Prof. Simon Kuhn

Dissertation presented in partial fulfilment
of the requirements for the degree of
Doctor of Science (PhD): Chemistry

October 2018

© 2018 KU Leuven – Faculty of Science

Uitgegeven in eigen beheer, Alican Gençer, Kortrijk, Belgium

Alle rechten voorbehouden. Niets uit deze uitgave mag worden vermenigvuldigd en/of openbaar gemaakt worden door middel van druk, fotokopie, microfilm, elektronisch of op welke andere wijze ook zonder voorafgaandelijke schriftelijke toestemming van de uitgever.

All rights reserved. No part of the publication may be reproduced in any form by print, photoprint, microfilm, electronic or any other means without written permission from the publisher.

Abstract

Cellulose nanocrystals (CNCs) are a bio-based organic material that has unique properties, including renewability, biodegradability, sustainability, environmental friendliness, a high stiffness, an adaptable surface chemistry, chirality, a high surface area, and an anisotropic morphology. These properties make CNCs a promising candidate for applications in nanocomposites, films, paper products, membranes, cement, photonic devices, inks, and tissue engineering scaffolds. Cellulose nanocrystals are commonly obtained via sulfuric acid hydrolysis of cellulosic source yielding rod-like shaped and negatively charged nanocrystals which form stable aqueous colloidal dispersions.

One of the unique interests of CNCs originates from their ability to self-assemble in bulk suspension. Rod-like shaped CNCs exhibit a phase transition from an isotropic phase to a chiral nematic phase with increasing concentration of the suspension. The chiral nematic structure can be preserved upon solvent evaporation to obtain films that display structural color. This property can be utilized to manufacture inks, coatings, sensors, or optical devices. Structured CNC films can be produced via evaporation-induced self-assembly of colloidal drops. However, particle deposition onto a substrate is affected by the flow dynamics inside sessile droplets, and usually yields a ring-shaped deposition pattern commonly referred to as the coffee-ring effect. Therefore, a good understanding of film formation is required to improve the thickness uniformity of the films and to control the optical properties of the obtained films.

This thesis provides new insights into the colloidal deposition and its control for cellulose nanocrystal film formation. The structural coloration in CNC films obtained via evaporation of drop casted CNC suspensions onto solid substrates was studied. First, the role of particle concentration in the drying droplets on the deposition of CNCs was investigated. Determination of the concentration in the drying colloidal drop is crucial since CNCs exhibit different phases in the suspension at different concentration regimes. These are respectively from low to high concentration an isotropic phase, a biphasic transition regime, and a chiral nematic phase.

Furthermore, the helical pitch of the chiral nematically assembled phase changes as a function of the concentration. Therefore, an analytical method was formulated to determine the concentration inside the colloidal drop during drying.

In addition, the fluid flow inside the drying colloidal drops was characterized via analysis of Marangoni flow, particle diffusion, and the viscosity of the suspensions. After understanding the role of the concentration and fluid flow on the deposition pattern of CNC films, this study also aimed to control the colloidal deposition of CNCs, and to investigate the effect of the deposition pattern on the optical properties of the obtained films.

To modulate the deposition pattern, a methodology was developed to generate uniform films by harnessing solutal Marangoni flow during evaporation. For this, colloidal drops of CNCs were exposed to an air/ethanol atmosphere with varying vapor composition. The coffee-ring effect was suppressed by increasing the Marangoni flow relative to capillary flow inside the droplet. The colloidal stability of the CNC suspensions in the ethanol-water mixtures was also characterized by rheological and zeta potential measurements to optimize the optical properties of the obtained films through the desired structure formation. Consequently, iridescent films with a uniform thickness were produced.

Next, an alternative way to control the colloidal deposition was designed through restriction of the capillary flow inside a drying droplet by inducing gelation. The effect of gelation on the deposition pattern and on the self-assembly of CNCs was investigated for the dried films. CNC films were thus obtained by drop casting CNC suspensions containing NaCl and CaCl₂ salts. The system was studied using rheological measurements and depolarized dynamic light scattering. In addition, analysis of the suspension's surface tension, viscosity, and yield stress were used to gain a deeper insight into the deposition process. Lastly, the understanding of the gelation behavior in the drying droplet was used to exert control over the deposit where the coffee-ring deposit could be converted to a dome-shaped deposit.

Finally, the optical properties of the CNC films dried onto superhydrophobic substrates were also investigated. In this study, a method was proposed to investigate the contribution of the thermal Marangoni flow in the drying droplets.

To conclude, this research demonstrates key solutions to avoid problems related to non-uniform film formation in case of colloidal deposition of CNCs in drying droplets. The work presented here provides one of the first investigations into how strategies including exploiting solutal Marangoni flow and gelation-induced drying can be used to control the deposition of CNCs into films.

Samenvatting

Cellulose nanokristallen (CNCs) zijn biogebaseerde organische materialen met unieke eigenschappen zoals hernieuwbaarheid, biodegradeerbaarheid, duurzaamheid, milieuvriendelijkheid, een hoge stijfheid, modificeerbare oppervlaktechemie, chiraliteit, een hoog specifiek oppervlak, en een anisotrope vorm. Deze eigenschappen maken van CNCs een veelbelovend product voor toepassingen in nanocomposieten, films, papierproducten, membranen, cement, fotonische materialen, inkten, en poreuze netwerken voor celgroei. Cellulose nanokristallen worden gewoonlijk verkregen via een hydrolyse van natuurlijke cellulose met zwavelzuur. Dit geeft staafvormige nanokristallen met een negatieve lading aan het oppervlak, wat stabiele waterige colloïdale dispersies mogelijk maakt.

CNCs kunnen in suspensie op eigen kracht reguliere structuren vormen, wat hen zeer interessant maakt. De staafvormige CNCs ondergaan een fase-transitie van een isotrope (3D willekeurige oriëntatie) fase naar een chiraal nematische fase met toenemende concentratie in de suspensie. Deze chiraal nematische structuur kan behouden worden tijdens verdamping van het water, wat leidt tot films die een structurele kleur vertonen. Dit kan gebruikt worden in inkten, coatings, sensoren, en in optische toepassingen. Gestructureerde CNC films kunnen geproduceerd worden via de natuurlijke structurering van de CNCs tijdens het drogen van colloïdale CNC suspensiedruppels. Het depositiepatroon van de CNCs wordt echter beïnvloed door de interne vloeistofmechanica in de druppel en dit interne vloeigedrag leidt normaal tot een ringvormige depositie dat over het algemeen het koffiëringeffect genoemd wordt. Daarom is het noodzakelijk om de filmvorming beter te begrijpen zodat een uniforme dikte van de film gegarandeerd kan worden en om de optische eigenschappen van de gevormde film te kunnen controleren.

Dit eindwerk geeft nieuwe inzichten in de colloïdale depositie van en in de controle over de filmvorming tijdens het drogen van CNC suspensiedruppels. De structurele kleur die verkregen wordt tijdens het drogen van de CNC suspensiedruppels op vaste oppervlakken werd bestudeerd. Ten eerste werd de rol van de concentratie van nanodeeltjes in de suspensie op het depositiepatroon bestudeerd. Het bepalen van de

concentratie in de drogende druppel is cruciaal aangezien CNCs kunnen bestaan in verschillende staten van organisatie afhankelijk van hun concentratie. Deze zijn respectievelijk van lagen naar hoge concentratie: een isotrope fase, een tweefasig overgangsregime, en een chiraal nematische fase. Bovendien is de pitch van de chiraal nematische fase ook nog eens afhankelijk van de concentratie. Daarom werd een analytische methode ontwikkeld om de concentratie van de nanodeeltjes in de druppel tijdens het drogen te kunnen berekenen.

Daarnaast werden vloeistofstromingen in de drogende colloïdale druppel bestudeerd via analyse van Marangoni stroming, diffusie van de nanodeeltjes, en de viscositeit van de suspensie. Eens er voldoende kennis was opgebouwd over de rol van de deeltjesconcentratie en het interne vloeigedrag in de drogende druppel op het depositiepatroon van de CNC films, werd deze kennis gebruikt om de colloïdale depositie van CNCs te controleren en om het effect van het depositiepatroon op de optische eigenschappen van de gevormde films te bestuderen.

Om het depositiepatroon te veranderen werd een methodologie ontwikkeld om films met een uniforme dikte te bekomen door Marangoni stroming geïnduceerd door een extra opgeloste stof tijdens het drogen van de druppel te gebruiken. Hiervoor werden druppels gedroogd in een lucht/ethanol atmosfeer met variërende compositie. Het koffiëringeffect kon op deze manier geëlimineerd worden omdat atmosferisch ethanol oploste in de druppel en zo Marangoni stroming versterkte ten opzichte van capillaire stroming. De colloïdale stabiliteit van de CNC suspensies in water/ethanol mengsels werd ook in kaart gebracht met reologische en zeta potentiaalmetingen om de optische eigenschappen van de bekomen films te optimaliseren. Hierdoor werd het mogelijk om iriserende films met een uniforme filmdikte te maken.

Vervolgens werd een alternatieve manier ontworpen om colloïdale depositie te controleren: via het verminderen van capillaire stroming in de drogende druppel via gelvorming. Het effect van gelvorming op het depositiepatroon en op het zelf-structureren van de CNCs werd aldus bestudeerd. Hiervoor werden waterige suspensies van CNCs met opgeloste NaCl en CaCl₂ zouten gebruikt. Dit systeem werd dan bestudeerd via reologische en gedepolariseerde dynamische lichtverstrooiingsmetingen. Verder werden ook de oppervlaktespanning, viscositeit,

en vloeigrens van de gels bepaald om een dieper inzicht te krijgen in het gedrag van de zout-CNC suspensies. Ten slotte werd de opgedane kennis gebruikt om het depositiepatroon van de CNC suspensies te veranderen van een koffiëring patroon naar een koepelvormige afzetting.

Ten laatste werden de optische eigenschappen van CNC films gevormd door depositie op superhydrofobe oppervlakken bestudeerd. Hierbij werd ook een methode voorgesteld om de bijdrage van thermische Marangoni stroming in de drogende druppels te bestuderen.

Ter conclusie, het onderzoek in dit eindwerk demonstreert belangrijke oplossingen om problemen met niet-uniforme filmvorming tijdens colloïdale depositie van CNCs in drogende druppels te voorkomen. Dit werk vormt een van de eerste studies die Marangoni stroming onder invloed van extra opgeloste stoffen en die gelvorming in drogende colloïdale druppels gebruikt om het depositiepatroon van CNCs in films te controleren.

Acknowledgment

I have extended existing knowledge on several subjects during the course of my doctoral study. Of course, I was not alone in my journey of the exploration of the unknown. Firstly, I owe many thanks to all my teachers who educated me to be a scientist. I thank my teachers and scientists all around the world who give me an inspiration.

I would like to thank my academic supervisor Prof. Wim Thielemans who shared his experiences and knowledge. I shared the same office with very valuable people during my Ph.D. I thank Sam Eyley and Marianne Labet Eyley from whom I have learned a lot. They have been very friendly and helpful together with my friends and colleagues Salvatore Lombardo and Jonas Van Rie. Thanks for the nice memories. I enjoyed our discussions about science. It was especially nice to talk with Salvatore and Jonas about football and Mediterranean cuisine and enjoy dinners while supporting Inter, Club Brugge and Beşiktaş. Talking about food, I should not forget to appreciate Belgian chocolate and waffle.

I also thank members of our research group (Åsa Jerlhagen, Gertrude Kignelman, An Verfaillie, Jonas Blockx, Maarten Mees, Reeta Salminen, and Praveen Ramasamy) for the friendly environment.

Thanks to Kyongok Kang for supervising DDLS experiments and their hospitality in Jülich. Sam Eyley for XPS measurements, Anja Vananroye for technical assistance in Smart Lab, Christina Schütz for AFM measurement and Kevin Truyaert for IR camera images.

Thanks to staff members at KULAK (janitor, library, and restaurant). Special thanks to Cemil from Kortrijk for the delicious food.

I would like to thank my family, my mother Şeyma, my father Hamit and my brothers Alicenk and Mehmet Salih for their endless love and support.

List of Abbreviations

AGUs	Anhydroglucose units
AFM	Atomic force microscopy
CNCs	Cellulose nanocrystals
DDLs	Depolarized dynamic light scattering
GI-WAXS	Grazing-incidence wide angle X-ray scattering
LVE	Linear viscoelastic
OPD	Optical path difference
PEO	Polyethylene oxide
rpm	Revolutions per minute
SEM	Scanning electron microscopy
SAXS	Small angle X-ray scattering
SDS	Sodium dodecyl sulfate
TEOS	Tetraethyl orthosilicate
TGA	Thermogravimetric analysis
TEM	Transmission electron microscopy
wt%	Weight concentration

List of Symbols

Symbol	Description	Units
B_o	Bond number	[-]
P	Chiral nematic pitch	[m]
η^*	Complex viscosity	[Pa.s]
K	Consistency coefficient	[Pa.s ⁿ]
χ^c	Crystallinity index	[-]
Γ	Decay constant	[1/s]
D	Diffusion coefficient	[m ² /s]
G'	Elastic Modulus	[Pa]
v_c	Evaporation velocity	[m/s]
p	Fluid pressure	[Pa]
f	Focal length	[m]
ω	Frequency	[rad/s]
l_c	Length scale of the droplet	[m]
Ma	Marangoni number	[-]
ϵ	Modified capillary number	[-]
M	Molarity	[mol/L]
X	Mole fraction	[-]
u_n	Normal velocity	[m/s]
D_{par}	Parallel diffusion coefficient	[m ² /s]
Pe_E	Péclet evaporation number	[-]
Pe_{Ma}	Péclet Marangoni number	[-]
D_{per}	Perpendicular diffusion coefficient	[m ² /s]
n	Refractive index	[-]
τ	Relaxation time	[s]
D_{rot}	Rotational diffusion coefficient	[s ⁻¹]
σ	Stress	[Pa]
γ	Surface tension	[N/m]

u_t	Tangential velocity	[m/s]
h	Thickness of the film	[m]
η	Viscosity	[Pa.s]
G''	Viscous Modulus	[Pa]
λ	Wavelength of light	[m]
q	Wavevector	[m ⁻¹]
W_o	Worthington number	[-]
σ_y	Yield stress	[Pa]
ζ	Zeta potential	[V]

Contents

Abstract	III
Samenvatting.....	VII
Acknowledgment	XI
List of Abbreviations.....	XII
List of Symbols	XIII
1. Introduction	1
1.1. Background	1
1.2. Aim of the thesis research.....	3
1.3. Thesis Outline	4
2. State of the Art	7
2.1. Colloidal self-assembly.....	7
2.2. Evaporation-induced self-assembly	10
2.3. Structural coloration.....	16
2.4. Cellulose Nanocrystals (CNCs).....	22
2.4.1. Preparation of CNCs	22
2.4.2. Characterization of CNCs	26
2.5. CNC suspension behavior.....	29
2.6. Chiral nematic structure of CNCs.....	31
2.7. CNCs based films	35
2.8. Methods of film formation.....	38
2.9. Applications of CNC films	42
2.10. Conclusions.....	44
3. Materials and Methods	45
3.1. Materials	45
3.2. Preparation of Cellulose Nanocrystal (CNC) Suspensions.....	45
3.3. Characterization of Cellulose Nanocrystals.....	46
3.3.1. Crystallinity of Cellulose Nanocrystals	46
3.3.2. Size Distribution of Cellulose Nanocrystals	48
3.3.3. Determination of Sulfate Ester Groups.....	50
3.4. Film Deposition	51

3.5.	Droplet Imaging.....	54
3.6.	Cross-Polarized Light Microscopy.....	55
3.7.	Profilometry Measurements	55
3.8.	Pendant Drop Tensiometry.....	56
3.9.	Rheological Measurements	57
3.10.	Depolarized Dynamic Light Scattering (DDLS).....	57
3.11.	Zeta Potential Measurements	58
4.	Deposition of Cellulose Nanocrystal Films	61
4.1.	Introduction	61
4.2.	Results and Discussion	62
4.2.1.	Concentration determination in colloidal drops	62
4.2.2.	Optical properties of the films	69
4.2.3.	Fluid dynamics	75
4.3.	Conclusions	83
5.	Control of the Deposition by Solutal Marangoni Flow	85
5.1.	Introduction	85
5.2.	Results and Discussion	86
5.2.1.	Rheological characterization	87
5.2.2.	Solutal Marangoni flow	92
5.2.3.	Film analysis.....	96
5.3.	Conclusions	102
6.	Effect of Gelation on the Deposition of CNC Films	105
6.1.	Introduction	105
6.2.	Results and Discussion	106
6.2.1.	Marangoni flow for salt containing CNC suspensions.....	117
6.2.2.	Analysis of the film deposition.....	122
6.2.2.1.	Colloidal CNCs drop containing NaCl	122
6.2.2.2.	Colloidal CNCs drop with CaCl ₂	127
6.2.3.	Optical properties of the films	129
6.3.	Conclusions	131
7.	Drying of CNC Films on Superhydrophobic Surfaces	133

7.1.	Introduction.....	133
7.2.	Results and Discussion	134
7.2.1.	Thermal Marangoni flow	138
7.3.	Conclusions.....	141
8.	General Conclusions and Outlook.....	143
	Appendix A: The Michel-Lévy Interference Color Chart.....	147
	Appendix B: Fluid Stresses at the Interface.....	148
	References	149
	Curriculum Vitae.....	170
	List of Publications	171

1. Introduction

1.1. Background

Humankind has produced many materials using numerous resources throughout history. In order to adapt these resources to specific applications, they have to undergo a tailored functionalization. Therefore, their design becomes significant to make them fulfil their task and increase their efficiency. Understanding the structure-property relationships in materials is one of the essential requirements to achieve the desired properties in materials. In general, it is important to have control over the structure of the components at different dimensional scales such as the macro, micro, nano and molecular scales to modulate the functional properties such as mechanical, magnetic and optical properties which need to be achieved for the targeted applications.

At the same time, the selection of raw materials for the production of materials has to be optimized with alternative resources and methodologies to protect the environment and to avoid environmental problems such as climate change. To this end, raw materials which are sustainable, renewable, less polluting, and biodegradable appear to be ideal candidates to obtain new materials.

Advances in materials science enable new possibilities to create novel materials and technologies that sustain progress in industry, technology and science. While materials science traditionally provided developments in fields such as metallurgy, ceramics and polymer materials, there is a trend in studies of nanotechnology in recent years. Nanotechnology offers great potential for the production of materials with superior properties since a wide range of material properties could differ from those of the bulk material properties at the nanometre scale.¹ For instance, the mechanical properties of the bulk materials are scale independent and are defined by continuum mechanics.² On the other hand, the mechanical properties of nanoparticles do not obey this continuum approximation and change as a function of the size of the particles.³ In addition, nanoparticles possess large surface areas which can be employed to increase reactivity as in catalysis applications.⁴ Another distinctive property of the nanomaterials is the observance of quantum confinement effects which can be used to

alter the electrical properties of the materials.⁵ As a result, an immense amount of investments have been made to produce and develop nanomaterials in recent years. For example, the U.S. invested about \$ 25 billion in nanotechnology related R&D between 2001 and 2018.⁶ In general, the nanotechnology market is estimated to reach \$ 3 trillion encompassing 6 million jobs by 2020.^{7,8}

A lot of developments have already been witnessed in nanotechnology enabling novel computing systems, electric cars, cognitive technologies, and new approaches to diagnosis and treatment of diseases like cancer dating back to the 20th century.⁸ In addition, many technological advances in fields such as communication, medicine, and electronics due to nanotechnological developments have significantly impacted our daily lives. For example, with nanotechnology major advances have been achieved in computing and electronics, leading to faster, smaller, and more portable systems that can manage and store larger amounts of information.⁷ In materials science, lightweight strong materials such as nanocomposites can be produced that increase cost- and fuel-efficiency in transportation. In medicine, targeted drug delivery is achieved with nanoparticles which can increase the efficiency to cure diseases.⁹

The design and fabrication of nanomaterials is crucial to achieve the desired properties in these produced materials. In addition, obtaining a hierarchical and tunable structure in nanomaterial can lead to better control over electronic, optical, mechanical, and catalytic functionalities that can be advantageous in many different applications. For this reason, research is widely carried out to achieve control over structure formation in the produced nanomaterials.

It is also known that in nature animals, plants, and minerals already form nanoscale structures for the production of color in their bodies. This phenomenon, referred to as structural coloration can be mimicked to fabricate materials such as photonic crystals to control and manipulate light.¹⁰ Structural color formation can also be obtained via periodical arrangement of colloidal particles. One straightforward way of succeeding this is to make use of self-assembled colloidal nanoparticles that can achieve long-range order. For instance, rod-like cellulose nanocrystals (CNCs) are shown to produce iridescent and light-diffracting films in this manner.^{11,12,13,14}

Cellulose nanocrystals are a bio-based, sustainable and non-toxic material which can surpass alternative materials such as inorganic pigments or dyes in ink applications since photobleaching is non-existent in structural coloration. CNCs self-assemble in suspension above a critical concentration into chiral nematic structures.^{12,15,16} This long-range order can be retained in dried films leading to color formation associated with the chiral nematic order of the CNCs. Although there have been several studies to control the chiral nematic assembly of CNCs in aqueous suspension and films, there has been no investigation to control the colloidal deposition of these CNCs.

1.2. Aim of the thesis research

The main aim of this thesis is to understand and control the colloidal deposition of cellulose nanocrystals films. Meanwhile, structural color formation in these cellulose nanocrystal films is investigated. In a first instance, the deposition process of cellulose nanocrystals from evaporating sessile colloidal drops on solid substrates was studied. The influence of the suspension concentration and the fluid flow on the formation of CNC films are described.

The characteristics of the particle deposition process together with the self-assembly in the drying suspension has a direct effect on the optical properties of the obtained films. Particle deposition onto a substrate is affected by the flow dynamics inside sessile droplets and usually yields a ring-shaped deposition pattern commonly referred to as the coffee-ring effect. For this reason, different strategies to suppress the coffee-ring effect were investigated in order to achieve homogeneous deposition of CNCs in drying colloidal films. In general, fluid flow can be manipulated to counteract the capillary flow which is responsible for the coffee-ring effect.

A dimensionless number analysis was carried out to understand the fluid dynamics and to examine the effect of influencing factors on the deposition profile of the films. Firstly, it is aimed to achieve a control over the colloidal deposition of CNCs in evaporating sessile droplets by generating Marangoni flow which is induced by surface tension gradients and can reduce the impact of the capillary flow. The magnitude of this flow can be manipulated by changing the gradient of the surface

tension along the interface. Consequently, homogeneity of the deposit can be attained by finding a balance between the competing flows inside the drying drop.

In another strategy, colloidal deposition is proposed to be controlled by inducing gelation in the CNC suspensions. The addition of ions to CNC suspensions results in the formation of gels which is due to changed electrostatic interactions between the CNCs. The rheological properties of the suspensions can be altered by the type and the concentration of ions added.

1.3. Thesis Outline

After this introduction, the thesis will define the state of the art. In this chapter, colloidal self-assembly is introduced briefly, followed by a description of evaporation-induced self-assembly. Then, examples of structural coloration observed in various instances in nature are described. Finally, a comprehensive literature review on CNCs is given which includes preparation and properties of CNCs, their suspension behavior and chiral nematic assembly, CNC based films, and methods of film formation and their applications.

In Chapter 3, the materials and the experimental methods that were used in this thesis are described. Common characterization information for produced CNCs is also given and explained in detail.

In Chapter 4, the behavior of the suspensions during colloidal drop drying is studied in terms of concentration changes, fluid flow and particle deposition. First, an understanding of the deposition of CNCs and of the concentration changes of the suspensions during the drying of the sessile droplets is developed. To this end, a new analytical approach to determine the deposition rate of the particles is described. Dimensionless numbers are introduced to characterize the fluid dynamics and to be able to describe the contributing factors to the deposition profile.

The influence of solutal Marangoni flow as a possible way to suppress the coffee-ring effect is investigated in Chapter 5. In this scenario, induced surface tension gradients are designed to create an inward flow which can counteract capillary flow. At the same time, the colloidal stability of the suspensions is checked to assure structure formation in the depositing CNC films.

In Chapter 6, the effect of induced elastic resistance on the colloidal deposition of drying colloidal drops is studied. Thus, the effect of ion-mediated gelation on the colloidal deposition of CNC films is introduced. Through gelation, particle transfer toward the edge of the drying drop is expected to be reduced thereby limiting or eliminating the coffee-ring effect. CNC films are obtained by drop casting CNC suspensions containing NaCl and CaCl₂. Finally, the effect of gelation on the colloidal deposition of CNCs is studied.

In Chapter 7, the self-assembly behavior of CNCs is studied via drop-casting CNC suspensions onto the superhydrophobic substrates. This method gives an alternative evaporation mechanism in case of evaporation-induced self-assembly processes of CNCs.

In the last chapter, general conclusions are given together with an outlook of further research possibilities.

2. State of the Art

Nanostructured materials can be obtained via top-down or bottom-up approaches based on the direction of changes at the length scales to create a hierarchy in their constituents.¹⁷ Top-down approaches resemble sculpting in which a bulk material is reduced in size to reach the desired dimension.^{18,19} Examples of the top-down approach in nanotechnology include photolithography, nanoimprint lithography and scanning beam lithography which are widely employed in the semiconductor industry to manufacture integrated circuits and other nanodevices.^{20,21} Although this approach is efficient to create structures at the nanometre scale, it requires specific accessories such as photomasks and photoresists which can set a limit on the achievable structure and limits usable substrates, typically silicon.

Alternatively, bottom-up approaches can be used to produce nanostructured materials starting from the molecular level and obtaining building blocks by chemical synthesis or assembly.²² Bottom-up approaches are more practical and cost-efficient compared to top-down methods in terms of the equipment needed for the production of complex patterns.²³ However, the choice of building blocks can be limited to certain atoms or molecules. Colloidal self-assembly of nanoparticles can be considered a bottom-up approach which has been applied to many systems to obtain complex nanostructured materials in a relatively simple way compared to other methods. This is owing to the accessibility of range of particle shape and sizes, particle interactions, and the availability of different experimental routes.

2.1. Colloidal self-assembly

Functional nanomaterials can be produced by employing self-assembly of colloidal nanoparticles in which individual constituents arrange into an ordered structure. In general, the self-assembly of organic or inorganic building blocks occurs spontaneously or is directed by other molecules, specific particle interactions or external forces.²⁴ Some of the particle interactions that can be used such as van der Waals forces, electrostatic interactions, and hydrogen bonding, are already applied extensively in supramolecular chemistry where molecules are assembled.^{25,26} The control over self-assembly starts with the size and shape of the individual components

as depicted in the core section in Figure 2-1.²² Colloidal particles can assemble into an ordered array to form colloidal crystals. Both isotropic and anisotropic particles can be used to obtain colloidal crystals.²⁷ However, the size distribution of the particles is a key factor for the crystallization of colloidal crystals without any defects. For that reason, chemical procedures such as emulsion polymerization or sol-gel processes are used to obtain monodisperse spherical particles^{28,29} whereas seed-mediated-growth methods are developed to control the aspect ratio of the rod-shaped nanoparticles.³⁰ For rod-shaped particles, the diameter of the rods can also be controlled via template-mediated fabrication using pore arrays.³¹

It is also known that rod-like particles can exhibit liquid crystalline behavior. Liquid crystals are an intermediate state of matter with the characteristics of both liquids (fluidity) and solid crystals (long-range order).³² Different types of liquid crystal phases exist depending on the degree of order of the particles. Examples of the liquid crystal phases are isotropic, nematic, smectic and chiral nematic.³² In the case of the nematic liquid crystal phase, rod-like particles possess orientational order in which the particles align their long axes oriented in a particular direction but particles do not have positional order. Colloidal suspensions of rod-like particles including fd virus, boehmite and tobacco mosaic virus were reported to form nematic phase.^{33,34,35} On the other hand, rod-like cellulose nanocrystals are known to assemble in chiral nematic phase in which the particles have helicoidal arrangement.¹⁶

In addition to shape properties of the particles, the surface chemistry of the particles plays an important role in the stabilization of the colloidal systems and in the control over self-assembly process. Steric stabilization can be achieved via the adsorption of surfactants or polymers onto particle surfaces whereas electrostatic stabilization is maintained by the manipulation of the surface charges of the particles and the ionic strength of the medium.^{36,37,38} Directed self-assembly of colloidal particles has been achieved via modulation of particle interactions or applying external forces such as electric fields, magnetic fields, or macroscopic deformation (e.g. fluid flow).^{24,39}

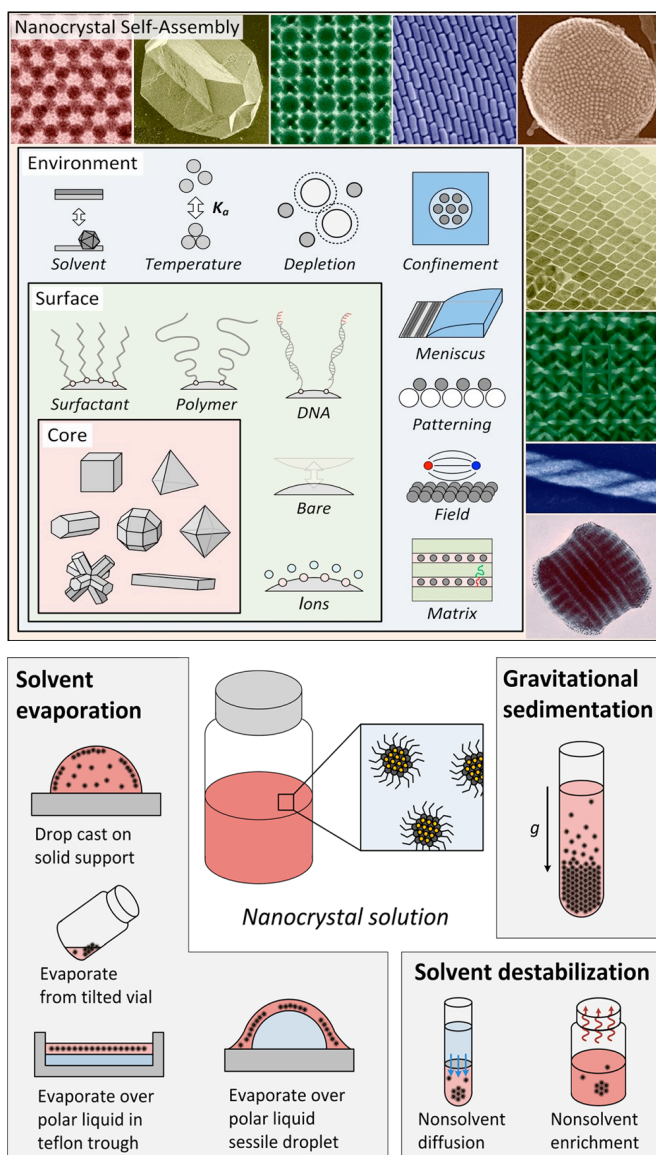


Figure 2-1 Control of nanocrystal self-assembly in different length scales and experimental approaches (Reproduced with permission from the publisher ²²)

2.2. Evaporation-induced self-assembly

Several experimental approaches have been introduced to study colloidal self-assembly based on evaporation, deposition, and sedimentation of particles. Those alternative fabrication techniques for self-assembled nanostructures are illustrated in Figure 2-1.²² The evaporation induced self-assembly process is generally exploited to obtain nanostructured thin films via drying of a colloidal dispersions, whereas destabilization or sedimentation of particles is used to generate three dimensional structures of particles.⁴⁰

Evaporation induced self-assembly of particles can be carried out in different configurations such as sessile or pendant drop evaporation, evaporation under confinement which include wedge, parallel plate, or cylindrical confinement, and vertical deposition such as dip-coating.³⁹ Frequently, a drop of solvent laden with particles is allowed to dry freely and spontaneous assembly of individual components is achieved via solvent evaporation. However, understanding of the drying process and the deposition of the colloidal particles is crucial to be able to manipulate the self-assembly of micro- or nanoparticles.^{41,42,43,44} For instance, a sessile drop evaporating on a solid hydrophilic substrate has a higher evaporation rate (blue arrows) towards the contact line (Figure 2-2). This edge enhancement of the evaporation arises from the higher probability of an evaporating molecule's escape when leaving from the edge than when leaving from the center of the surface of the drop.⁴⁵ In other words, the probability of an evaporating molecule's reabsorption to the drop is affected by its point of departure. A random walk initiated at the center of the drop results in the molecule being reabsorbed at a higher probability so that the evaporation is not completed. However, the same random walk initiated from the edge allows the evaporating molecule to escape from the liquid phase to the vapor phase. The higher evaporation at the perimeter of the drop induces an outward fluid flow within drop to replenish the evaporated fluid as shown in Figure 2-2. In the presence of particles, this outward flow, called the capillary flow, carries the particles from the bulk drop towards the edge of the drop where they deposit and form a ring shaped deposit, generally referred to as the coffee-ring effect.⁴⁶

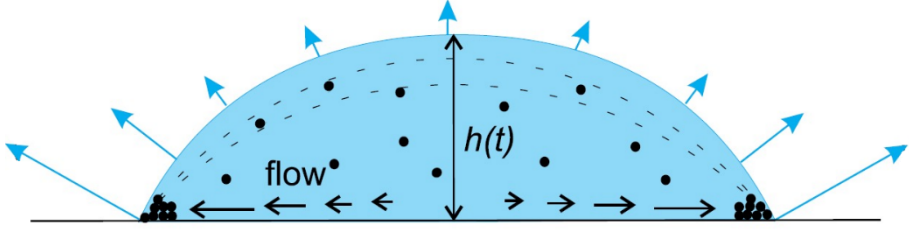


Figure 2-2 Capillary flow inside an evaporating droplet (Reproduced with permission from the publisher ⁴⁷)

The growth of mass of the particles in the ring, m_R was described by Deegan *et al.* taking into account the evaporation rate (Equation 2.1).⁴⁵

$$m_r = m_0 \left[1 - (t/t_f)^{(1+\lambda)/2} \right]^{2/(1+\lambda)} \quad (2.1)$$

where m_0 is the total mass of the particles, t_f is the total drying time, λ is equal to $(\pi - 2\theta_c)/(2\pi - 2\theta_c)$ and θ_c is the contact angle of the drop.

At the same time, evaporation induced self-assembly is a dynamic process in which properties of the suspension including concentration, viscosity and surface tension are subject to change due to loss of solvent. Understanding these complex phenomena brought many disciplines such as physics, mechanical engineering, chemistry and chemical engineering together to solve problems in many applications where a uniform particle deposition is required, such as inkjet printing, spray coating, assembly of photonic components, and the manufacture of DNA microarrays. Numerous researches have been carried out to control the deposition of films in the case of inkjet printing applications.^{48,49,50,51} Consequently, inkjet printing of arrays of colloidal drops enables many possibilities to create patterned structures.⁴⁹ For instance, several companies including Samsung, LG, and Visionox have invested in inkjet printing methods for the fabrication of organic light-emitting diodes (OLED), quantum light-emitting diodes (QLED), and thin-film transistors.⁵²

Knowing that colloidal deposition is linked to fluid flow behavior, the internal flow inside a drop has to be characterized to understand the formation of ring deposits. One way of achieving this is by direct visualization of tracer particles within a drying drop.⁵³ Velocity fields of individual micron-sized or fluorescent particles can be mapped to understand the magnitude of the capillary flow.^{54,55,56} However, the method of direct visualization of tracer particles is limited to micron-sized particles due to the optical resolution of optical microscopes. To be able to study colloidal drops containing nano-sized particles, there is a need for another approach since direct visualization of nanoparticles is not feasible with optical microscopy. At the same time the addition of tracer particles to colloidal suspensions can cause aggregation of nanoparticles. For this reason, a numerical solutions of the flow field inside drying drop can be used applying a finite element algorithm which solves simultaneously for the vapor concentration and the flow field inside the droplet.⁵⁷ Such numerical solutions are based on solving the Navier-Stokes equations (for a Newtonian fluid) (Equation 2.2).

$$\rho \left(\frac{\partial u}{\partial t} + u \cdot \nabla u \right) = -\nabla p + \eta \nabla^2 u + F \quad (2.2)$$

where ρ is the fluid density, u is the velocity field, p is the fluid pressure, η is the viscosity and F is the body force acting on a fluid. Nondimensionalization of Navier-Stokes equations and the surface boundary conditions yields dimensionless numbers which can be used to provide physical insight into the importance of various terms in the system of governing equations.⁵⁸

Several studies have been carried out using numerical simulations of the flow field inside drying drops to have an understanding of the colloidal deposition.^{59,60,61} The numerical results were compared to experimental results of deposited films in which deposit shapes were related to the different flow patterns. It was pointed out that the change of evaporation dynamics across the surface has an effect on the capillary flow.⁶² In principle, the evaporation rate in a drying drop is higher towards the contact line, and evaporated solvent is replenished from the bulk by means of capillary flow. Therefore, the geometry of the droplet can be manipulated to control the evaporation

rate across the surface.⁶³ It was also reported that the evaporation flux becomes more uniform at the drop surface when a drop has a more spherical shape rather than being a spherical cap. For a spherical cap the predominant length scale is the radius compared to the height as shown in Figure 2-2. In another example, molecular simulations were used to investigate the evaporation flux distribution of sessile drops. It was shown that the evaporation flux across the surface of the droplet changed for drying drops when cast onto either hydrophilic or hydrophobic substrates.⁶⁴

Many methodologies have been developed to manage the flow dynamics in evaporating colloidal drops to reduce the effect of capillary flow and to control the deposition process of particles.^{65,66} This requires a good understanding of the flow behavior and related features such as evaporation dynamics, mechanical instabilities, and rheological properties of the medium.⁶⁷ Researchers have focused on the manipulation of the flow inside a drop during the drying process which is responsible for the transfer of the particles. For instance, suppression of the coffee-ring effect was achieved by enhancing Marangoni flow which is induced by surface tension gradients at the liquid interface.⁶⁸ Historically, Gustave Van der Mensbrugghe reviewed all possible instances of surface movements due to local differences of interfacial tension in 1869.⁶⁹ He was then challenged by Carlo Marangoni who claimed his work was earlier and described the flow behavior at liquid interfaces induced by surface tension gradients in 1871.^{70,71} Surface tension gradients arise for example due to solute concentration gradients and/or temperature gradients. Since then, related works have been named after Marangoni in forms of Marangoni flow, Marangoni eddies and Marangoni instabilities. Much research has been carried out on different aspects of Marangoni flow in terms of different effects that induce surface tension gradients such as thermal^{72,73}, optical^{74,75} and solutal^{76,77} Marangoni flow. In all cases, surface tension gradients create Marangoni stresses which are balanced by shear stress at the liquid interface and leads to Marangoni flow as shown in Figure 2-3.

The concept of thermal Marangoni flow has been studied for patterning of polymers to create internal structure or to introduce topographic features.⁷⁸

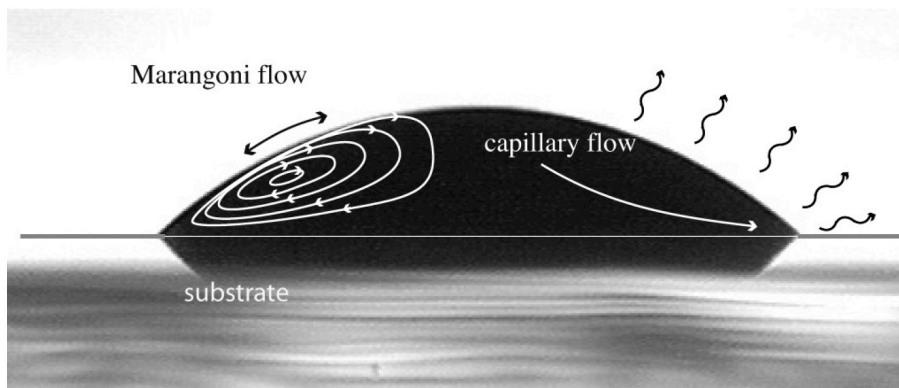


Figure 2-3 Comparison of Marangoni flow and capillary flow (Reproduced with permission from the publisher ⁷⁹)

In other works covering Marangoni flow, the effect of addition of surfactants on surface tension gradients and alterations of fluid flow were investigated.⁸⁰ An example of surfactant-induced Marangoni flow is shown in Figure 2-4. In this work, the uniform deposition of spherical polystyrene particles was achieved after evaporation of colloidal drop which includes an ionic surfactant i.e. sodium dodecyl sulfate (SDS). The coffee-ring effect was prevented through Marangoni flow which was induced by the variation of SDS concentration along the air-liquid interface. In a similar example, a surfactant-like polymer, polyethylene glycol (PEG), was used to induce surface tension gradients to control the deposition of the spherical particles.⁸¹

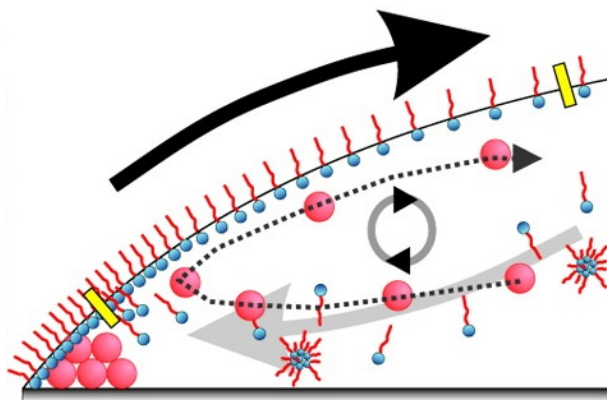


Figure 2-4 Surfactant-induced Marangoni flow controlling the transfer of the spherical particles (Reproduced with permission from the publisher ⁸²)

Other research was carried out studying sequential Marangoni flows including solutal and surfactant-induced Marangoni flow during drying of a drop of whisky.⁸³ It was reported that the preferential evaporation of ethanol in the drying drop created a solutal Marangoni flow. However, this flow was not enough to generate uniform deposits, thus a combination of surfactant and surface-adsorbed polymer was added to drying droplets to enhance the surface tension gradients. It was concluded that the addition of both surface-adsorbed molecules including surfactant, sodium dodecyl sulfate (SDS) and surface-adsorbed polymer, polyethylene oxide (PEO) was needed to achieve a uniform deposit. However, those additives caused problems associated with impurities in the obtained films. This problem can be avoided by solvent-mediated Marangoni flow in which the mixture of solvents with different surface tension values dried consecutively. For instance, adding high-boiling-point solvents such as diethylene glycol and formamide to water-based colloidal drop was demonstrated to exert control over the deposition of monodispersed silica microspheres.⁸⁴

In another example, photosensitive surfactants were used to control the colloidal deposition of polystyrene particles.⁸⁵ Adsorption of the photosensitive surfactant

AzoTAB (an amphiphilic molecule composed of a cationic head and a hydrophobic tail containing an azobenzene moiety) at the air–liquid interface was changed via irradiation of the drop with blue ($\lambda = 440$ nm) or UV ($\lambda = 365$ nm) light, since photoisomerization of the azobenzene group of the surfactant between its trans (less polar) and cis (more polar) states controls the adsorption behavior at the interface. Although Marangoni flow was not enough to control the deposition in this specific case, uniform deposition of particles was achieved by trapping the particles at the air–liquid interface by selective irradiation with light. The same strategy was also applied with increased concentrations of AzoTAB to be able to induce optical Marangoni flow in the drying drop and thus to control the colloidal deposition of the particles.^{74,75} The effect of particle shapes has also been studied for its ability to suppress the coffee-ring effect. For instance, ellipsoidal particles were shown to yield a uniform deposition since their structuring at the air–liquid interface by interparticle attractions prevents the suspended particles from reaching the drop edge.⁸⁶ It was discussed that the particle deposition was influenced by the competition between particle assembly at the drop surface and the evaporation-driven particle motion to the contact line. All in all, evaporation-induced self-assembly is a versatile method which can be used to generate structured films and the colloidal deposition can be controlled with different strategies.

2.3. Structural coloration

One of the most important applications of colloidal assembly is the fabrication of photonic crystals and nanostructures.^{87,88} Periodic arrangement of particles can lead to the generation of structural colors without the use of dyes or colorants. This structural color formation is observed in nature for many animals and plants.⁸⁹ A good example of this method of color formation is witnessed in the wing of a butterfly due to the structure it possesses (Figure 2-5).⁹⁰ Vertical separation between the shelves in the wing causes light interference in which blue light is selectively reflected. Features of colloidal assembly such as ordering of colloidal particles in a controlled manner can be used to fabricate such structures. Another example of structural coloration in

nature is observed in opal which is an amorphous form of silica. When monodispersed spheres of silica stacks in an ordered, closed-packed fashion, they produce colors by coherent scattering in the visible light range. In coherent scattering, there is a phase relationship between the scattered waves by ordered silica and it usually yields iridescence.⁹¹ Iridescent materials show luminous colours that seem to change when seen from different angles. Thus, structural colors can be generated from the patterning of the geometric hierarchy or refractive indices of the materials.⁹²

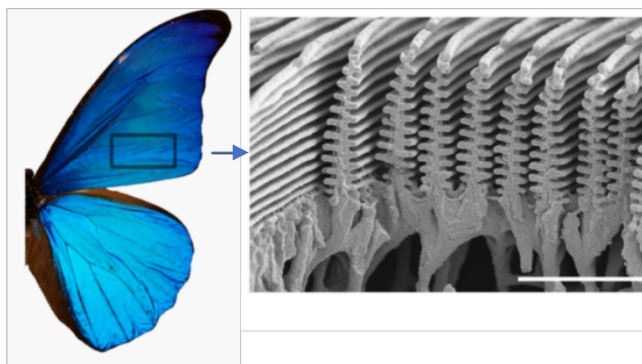


Figure 2-5 Image of Morpho butterfly and SEM image of wing (scale bar 2 μm , Reproduced with permission from the publisher ⁹³)

In the 17th century, Robert Hooke first defined structural color in his book titled “Micrographia” in which he described the microscopic observation of the feathers of peacocks, birds and ducks. He further discussed the phenomenon of changeable colors in these animals and postulated that their occurrence was due to the same causes and the textures they possess in their parts of the body.⁹⁴ For instance, he speculated that alternate layer of thin plates and air might strongly reflect light. Since then, natural products having optical properties gave inspiration to researchers to manufacture artificially tunable photonic materials having similar properties to those existing in nature. Many methods including top-down and bottom-up strategies have been developed to artificially mimic structural colors found in nature.⁹¹

The advantages of structural color formation are twofold when compared to color formation using pigments or dyes. First, there is no photobleaching thus fading of

colors will not occur in structurally colored materials as long as the structure is maintained. This is not the case for pigments since excitation of electron hole pairs via absorption of photons causes color loss over time.⁹⁵ This is due to generation of chemically reactive free radicals which can react with the dye to change its chemical structure. Secondly, special color effects such as iridescence or environmentally-induced color change can be generated by structural colors which is not the case for the pigments.

Utilization of nanoparticles in non-living colored objects is also distinguished. For example, the Lycurgus cup is a 4th century glass object that displays colors due to dispersed colloidal nanoparticles such as gold and silver (Figure 2-6, today preserved in British Museum in London).⁹⁶ This cup exhibits unique dichroic effects owing to the presence of the gold and silver nanoparticles. The cup looks green when light shines on it due to the reflection of light, yet the color changes to red when a light shine in it due to absorption and transmission of the light. It is known that this color formation depends on the concentration, size and shape of particles in colloidal suspensions.^{97,98,99} In the 8th century, quantitative recipes for colored glass were written down by Jabir ibn Hayyan.¹⁰⁰ These recipes describe the methods and ingredients to prepare glass with a variety of colors and even iridescence.



Figure 2-6 Lycurgus Cup

Optical processes related to structural colors can be classified into five classes which are thin-film interference, multilayer interference, diffraction grating, scattering and photonic crystals.^{92,101,102} Thin-film interference (Figure 2-7a) is typically observed in soap bubbles and occurs when light is reflected and interferes at the upper and lower boundaries of layers. Reflectivity of light depends on the thickness of the film layer, the refractive index of the film and the angle of incidence light.¹⁰² Constructive or destructive interference arises depending on the phases of the reflected light. The multilayer (multi-film) interference film (Figure 2-7b) is generated via an infinite number of pairs of thin layers piled up periodically.¹⁰³ In multilayer interference, color-dependent reflections arise from the interference caused by sharp periodic boundaries in the refractive index. An example of this type of color formation can be seen in the Morpho butterfly (Figure 2-5). In case of diffraction grating (Figure 2-7c), light reflectivity is similar to a periodic multilayer stack, except for the orientation of the periodicity of layers. Examples of diffraction grating includes the metallic-like colored holograms found on credit cards and foil-type wrapping paper.¹⁰⁴ Scattering of the light can be divided in two classes; coherent (Figure 2-7d) and incoherent (Figure 2-7e) scattering. Coherent scattering is responsible for the color formation in opals which results in iridescence.¹⁰⁵ For incoherent scattering, the scattering is random which leads to a diffuse appearance in reflection.⁹¹

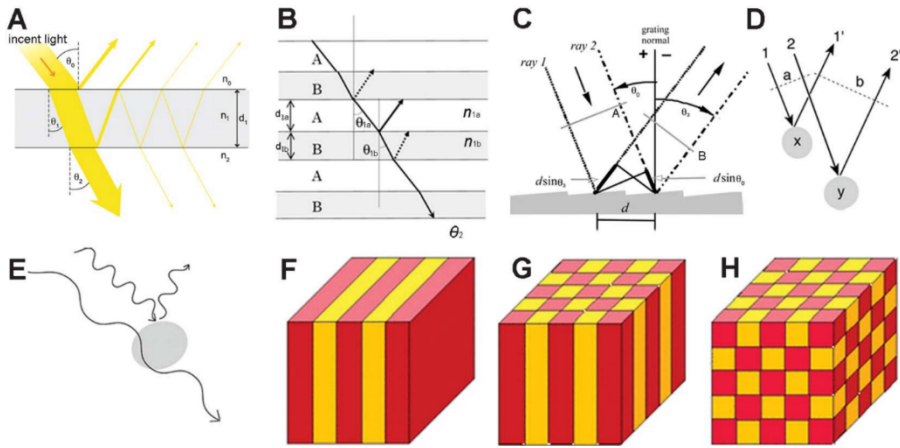


Figure 2-7 Structural colors arise via (a) thin-film interference, (b) multi-film interference (c) diffraction grating (d and e) scattering (coherent and incoherent scattering) and (f-h) photonic crystals (one-, two- and three dimensional photonic crystals) (Reproduced with permission from the publisher¹⁰²)

In the 20th century, Eli Yablonovitch founded the field of photonic crystals, which have an artificial periodic structure that results in different refractive indexes as shown in Figure 2-7f-h.¹⁰⁶ These crystals have specific optical properties such as a photonic band gap in which a range of wavelengths of light is blocked by the material.¹⁰⁷ The first photonic crystal was formed by drilling three intersecting arrays of holes into a block of ceramic material.¹⁰ Photonic crystals can also be obtained by a bottom-up assembly approach and are employed in several applications such as optical devices, anti-counterfeiting technologies, light waveguides, full-color displays, and sensors.^{108,109}

Examples of structural color formation are also observed in the case of helicoidal periodic structures. Such structures can be formed by cellulose nanocrystals or chitin. Indeed, the coloration of cellulose-based *Pollia condensata* fruit and chitin-based exoskeleton of some beetles occurs via helicoidal structure formation.¹¹⁰ For the beetle *C. gloriosa*, the bright green color, with silver stripes is observed in unpolarized light or with a left circular polarizer, whereas the green color is mostly lost when seen with a right circular polarizer (Figure 2-8).¹¹¹ In the case of *Pollia condensata*, blue iridescence is seen which is generated by helicoidally stacked cellulose microfibrils that form multilayers in the cell walls of the epicarp (Figure 2-8).

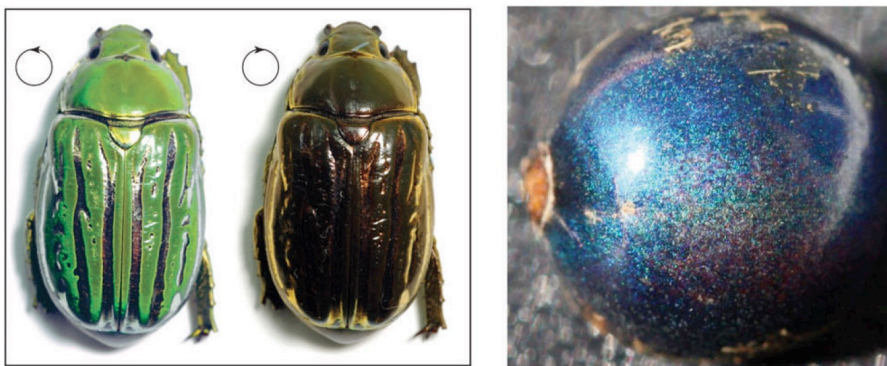


Figure 2-8 The beetle *C. gloriosa* (left) and *Pollia condensata* fruit (right). (Reproduced with permission from the publisher ^{110,111})

2.4. Cellulose Nanocrystals (CNCs)

In this thesis work, cellulose nanocrystals, which have the potential to self-assemble are chosen as a model system to generate structural color formation. Cellulose is a polymer present in many plants and animals such as wood, algae, and tunicates. In 1947, Nickerson and Habrle employed an acid hydrolysis process to isolate CNCs from the disordered intercrystalline regions of the networks of cellulose chains.¹¹² Later in 1959, Marchessault *et al.* studied that liquid crystalline order could be achieved in colloidal suspensions of CNCs.¹¹³ In 1992, Revol *et al.* produced stable chiral nematic liquid crystalline phase in aqueous suspensions of CNCs.¹⁶ In order to exploit the stable behavior of cellulose nanocrystal dispersions and to increase the mechanical properties of polymer materials, nanocomposites were prepared by Favier *et al.* from aqueous solutions of polymers using CNCs as a filler.¹¹⁴

CNCs have been described as sustainable, biocompatible, and their high stiffness can be employed in functional materials such as composites, hydrogels, foams, films, and medical applications.^{115,116} Market and scenario analysis showed that manufacturing costs for CNCs production ranged from 3632 \$/t to 4420 \$/t of CNCs (dry equivalent).¹¹⁷ Although pilot facilities have been constructed with production capacities as high as 1000 kg/day, there is not enough information from companies in terms of production of CNCs because the data is generally confidential and rarely shared.

The biological impact on human health and environmental risk that CNCs possess is under debate although earlier work has reported that CNCs display low toxicity potential and environmental risk.^{118,119,120,121}

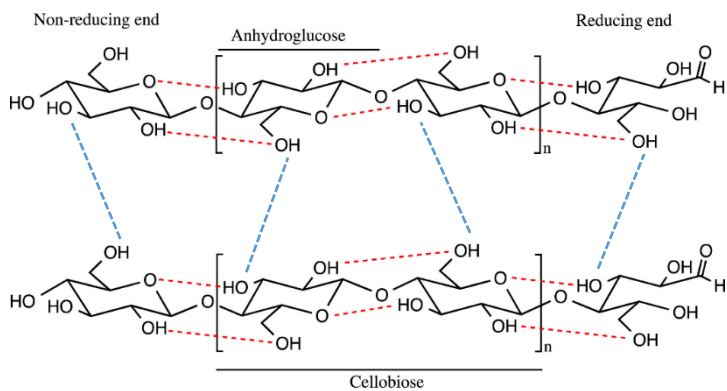
2.4.1. Preparation of CNCs

Cellulose is a semicrystalline polycarbohydrate composed of anhydroglucose units (AGUs) linked by chemical β -1,4-glycosidic bonds (Figure 2-9a).¹²² Each unit has three hydroxyl groups; one primary and two secondary, while the repeating AGUs take on the thermodynamically favorable chair conformation. Hydrogen bonds exist between adjacent anhydroglucose units (intra-hydrogen bonding) which result in chain rigidity and between chains (inter-molecular hydrogen bonding) (hydrogen

bonds are indicated with dashed lines in Figure 2-9a).¹²² The cellulose chain consists at one end with a non-reducing end and the other end with a reducing end which is in equilibrium with the aldehyde structure (Figure 2-9a).

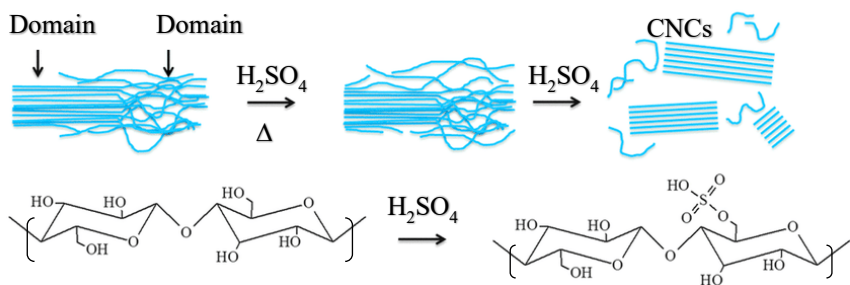
Cellulose nanocrystals (CNCs) are isolated from naturally occurring cellulosic sources.¹²³ Several patents have been registered describing different preparation methods of CNCs such as acid hydrolysis and enzymatically catalysed procedures.¹²⁴ Recent progress on production of CNCs including the sources and methods have been reviewed extensively in the literature.^{125,126,127} Various acids such as sulfuric acid, hydrobromic acid, hydrochloric acid, phosphoric acid, maleic acid, and hydrogen peroxide have been analysed to extract CNCs from different resources.¹²⁵ CNCs are generally produced by sulfuric acid hydrolysis of the cellulose polymer. CNC surface charges occur from sulfate ester groups which are induced during preparation with sulfuric acid hydrolysis as shown in Figure 2-9b. It was reported that CNCs isolated using hydrochloric acid (HCl) are uncharged which causes flocculation of CNCs.¹²⁸ In another study, HCl hydrolysis of cellulose was catalyzed by inorganic chlorides under hydrothermal conditions.¹²⁹ It was observed that the introduction of inorganic chlorides enhanced the hydrolysis process through faster degradation of the disordered region of cellulose. The procedure for CNC preparation involves an acid-induced hydrolysis of the disordered domains along the cellulose fibrils via diffusion of H^+ into cellulose microfibrils. The protons ingress results in the hydrolysis of the β -1,4-glycosidic bonds and the cellulose fibrils into rod-like CNCs as illustrated in Figure 2-9b.¹³⁰ Acid hydrolysis of cellulose takes place by rapid protonation of glucosidic oxygen or cyclic oxygen by protons from the acid, followed by a slow splitting of glucosidic bonds induced by the addition of water as shown in Figure 2-9c.¹³¹

(a)



(b)

Crystalline Disordered



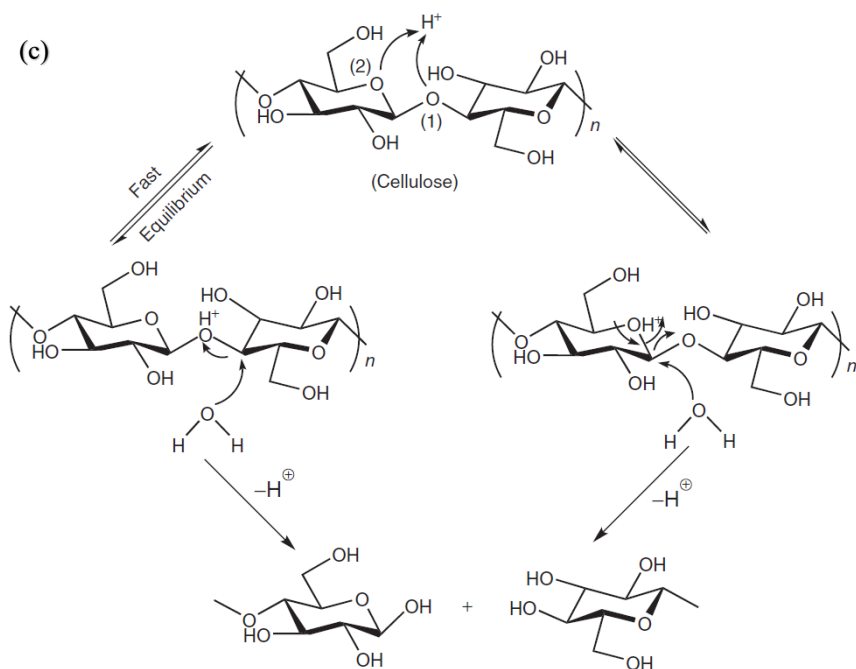


Figure 2-9 (a) Cellulose structure with the intra- (red) and inter-chain (blue) hydrogen bonds (b) Physical description of acid hydrolysis of cellulose nanocrystals (CNCs) and (c) Hydrolysis mechanism of cellulose chain (Reproduced with permission from the publishers^{130,131,132})

The cellulose source has significant importance for the characteristics of obtained CNCs in terms of size and aspect ratio of particles as illustrated with TEM images in Figure 2-10. The size and surface chemistry of cellulose nanocrystals are determined by the hydrolysis conditions such as duration of the hydrolysis, the acid reagents and their concentration, and the reaction temperature.^{133,134} Cellulose nanocrystals obtained via sulfuric acid hydrolysis of cellulose polymer form stable aqueous colloidal dispersions. This is attributed to electrostatic repulsion due to negatively charged sulfate esters groups introduced during the acid hydrolysis.

The surface of CNCs can also be modified chemically to disperse them in organic solvents and to use in different applications such as composite processing.^{135,136,137}

The main classes of reactions carried out on cellulose nanocrystals are oxidations, esterifications, amidations, carbamations and etherifications.¹³⁶ In addition CNCs can be coated with surfactants to increase dispersibility in organic solvents or to compatibilize them in hydrophobic polymer matrices.¹³⁸

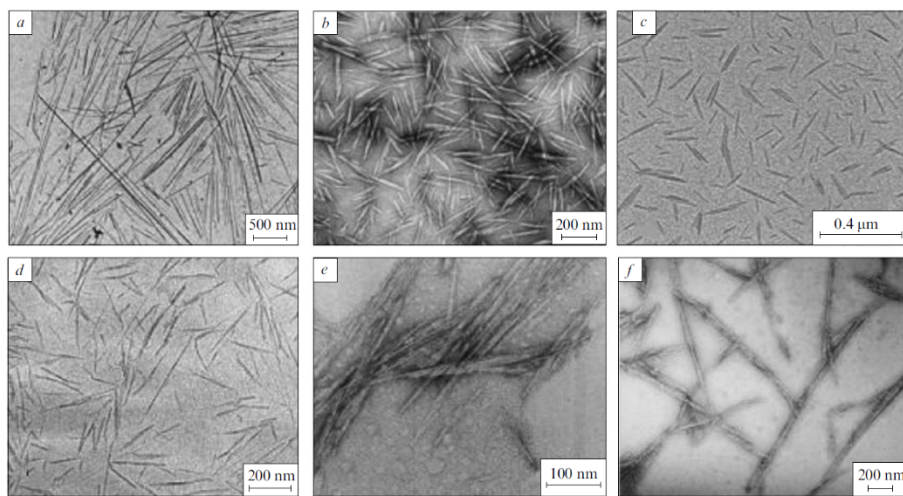


Figure 2-10 Transmission electron microscopy (TEM) images of CNCs obtained by acid hydrolysis of tunicin (a) China grass (ramie) (b) cotton (c) sugar beet (d) microcrystalline cellulose (e) and bacterial cellulose (f) (Reproduced with permission from the publisher¹³⁹)

2.4.2. Characterization of CNCs

Electron micrographs are most often used to characterize the morphology of CNCs, however it is difficult to image individual CNCs at high resolution because of their low electron density. In order to increase the resolution of the images, samples are stained with a heavy metal salt which enhances the contrast. However, staining of CNCs may also cause the aggregation of the particles. Several alternatives including alteration of grid surface and stain type were explored to achieve high contrast TEM images of individual CNCs.¹⁴⁰

In addition to electron microscopy studies, atomic force microscopy is frequently employed to determine the shape and the size distribution of CNCs.^{141,142,143,144}

Both TEM and AFM images can be studied complementarily to provide information on the shape and size distribution of the particles. Particles size analysis of the samples by AFM requires well-dispersed particles which are deposited on a flat substrate. Aggregated particles cannot be effectively measured as tip convolution makes particle edges indistinguishable. This is why sample preparation becomes crucial prior to AFM measurement. Drop casting or spin coating can be used to prepare CNC films for AFM measurement if the substrate is modified with a cationic polymer. Poly(allylamine hydrochloride) and poly-L-lysine (0.01–0.1 wt%), or amine-terminated monolayers, are commonly used as cationic adhesion layers and can be deposited by dip-coating or by spin coating followed by thorough rinsing.^{145,146}

Scattering techniques including small-angle X-ray scattering (SAXS) and small-angle neutron scattering (SANS) have also been used to determine the dimensions of cellulose nanocrystals.^{147,148} In these methods, structural information of CNC is obtained via the modelling of a suitable form factor of cellulose nanocrystals. For this reason, the choice of model and fitting process become crucial to get accurate results. For instance, it was found that CNC particles could not be fitted by a simple rigid rod model for the consideration of polydispersity.¹⁴⁹ Instead, a parallelepiped model with three characteristic lengths: particle length L , thickness a , and width b are typically used for a more correct modelling and size determination of CNCs.¹⁴⁷ Scattering measurements are carried out using dilute CNC suspensions to avoid interparticle scattering and structure contributions to the scattering pattern. For more concentrated suspensions, interparticle scattering has also to be taken into account and the scattering intensity will also depend on structuring of CNCs, e.g. alignment of the ribbon-like particles, in the suspension, making interpretation more complex.

The crystal structure of CNCs has been studied by different methods such as X-ray diffraction, Raman spectroscopy, and solid state NMR spectroscopy.¹²⁶ Different allomorphs of cellulose exist namely I_α , I_β , II, III, III_{II}, IV_I, IV_{II} (Figure 2-11).¹⁵⁰ Native crystalline cellulose has I_α or I_β structures which have parallel chain configurations (chains are oriented in the same direction with respect to reducing or non-reducing end). They differ in their crystalline structure where I_α has a triclinic one chain unit cell and I_β has a monoclinic two chains unit cell.^{128,151}

In general, the I_β structure (Figure 2-11) is dominant in higher plants such as wood or cotton whereas I_α is prevalent in bacterial cellulose and algae. Regeneration from solution or alkali treatment of cellulose I yields cellulose II which has an antiparallel chain configuration (chains are oriented in different direction with respect to reducing or non-reducing end).^{152,153} X-ray diffraction studies are carried out to analyze crystal structure changes or the degree of crystallinity upon chemical treatment of CNCs.^{136,154}

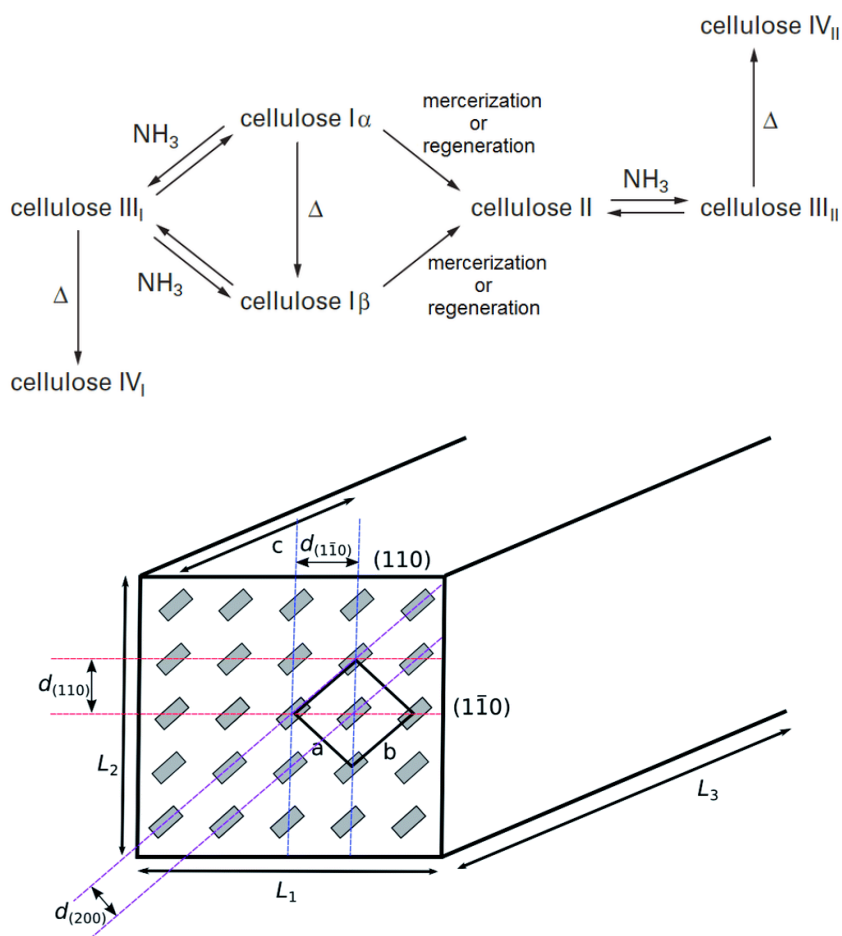


Figure 2-11 Cellulose allomorphs and cellulose I_β structure with cellulose chain ends in grey and corresponding crystal planes (Reproduced with permission from the publishers^{136,155})

After understanding the morphology of CNCs, it becomes important to characterize the surface charges of CNCs. Surface charges on the CNC surface have been shown to influence the structuring of the CNCs in suspension and the viscosity of CNC suspensions.¹⁵⁶ Several methods have been applied to determine the negatively charged sulfate ester groups of CNCs, including conductometric titration and acid-base titration.^{146,157} In addition, elemental analysis can be used to identify heteroatoms such as sulfur in a CNC sample to verify ionic grafts containing heteroatoms (e.g. sulfate half esters from sulfuric acid hydrolysis). Carbon, hydrogen, nitrogen, and sulfur elemental analysis (CHNS EA) is typically used to characterize cellulose.

2.5. CNC suspension behavior

Behavior of CNC suspensions including liquid crystalline phase behavior, viscosity, and surface tension were shown to depend on the source of cellulose.¹⁵⁸ The dependence of the source of cellulose on the properties of CNCs and thus its effect on self-assembly behavior have been studied in the literature.^{158,159} It was shown that CNC suspensions obtained from cotton or wood exhibit different liquid crystalline behavior, even though their dimensions are similar.¹⁵⁸ Rheological properties and liquid crystalline behavior of the suspensions have also been shown to vary with respect to the morphology and surface charge of the particles.^{160,161,162}

The concentration of CNC suspensions additionally has an effect on the rheological properties of the suspension. The viscosity of the suspensions increases with increasing concentration of particles.¹⁶³ At the same time, shear thinning has been observed for CNC suspensions at increased shear rates which is due to the alignment of the rod-like CNC particles in the direction of flow.¹⁶⁴ Viscoelastic properties of the CNC suspensions have also been analyzed to understand the behavior of rheological properties including complex viscosity, elastic modulus and viscous modulus. In a low concentration regime (<10 vol%), the suspensions behaved as a viscous fluid whereas at higher concentrations (>12 vol%), the suspensions started to display mainly elastic behavior.¹⁶³ In another study, the viscosity of CNC suspension significantly altered after applying ultrasound energy.¹⁶⁵ It was found that increasing the amount of applied ultrasound energy significantly decreased the viscosity of CNC

suspensions. The decrease in viscosity values with applied ultrasound energy was attributed to the breakage of aggregates in the suspension.

The effects of additional components mixed with the CNCs has been investigated for polymers^{166,167,168,169} or salts^{170,171,172} to understand how these additives affect the CNC self-assembly in the suspension. Nanocrystals can form network structures and this occurs at lower concentrations as the ionic strength is increased.^{173,174,175} In this scenario, each nanocrystal acts as a collector, and nanocrystals will deposit onto each other due to screening of electrostatic repulsions.¹⁷⁶ Full analysis of this behavior is very complex because of the shape of the cellulose nanocrystals, their longitudinal twist, and local surface charge information. Previously, molecular dynamics simulations have been used to understand the structure and charge distribution of the cellulose nanocrystals with added NaCl.¹⁷⁷ An analysis of the 3D maps of the Na⁺ density distribution confirmed that an increase in electrolyte concentration shrinks the electric interfacial layer and weakens the effective repulsion between charged CNCs.¹⁷⁷

Other aqueous CNC-cation interactions have also been studied by mixing CNCs with different salts resulting in the formation of hydrogels, where the formation of a network was proven through rheological measurements.¹⁷⁸ Furthermore, the aggregation¹⁷³ and the gelation^{178,179} of CNCs with changes in ionic strength of the CNC suspensions have also been investigated using SANS,¹⁷³ SAXS,¹⁷⁸ and Monte Carlo simulations.¹⁸⁰ In addition, the gelation kinetics and the gel structure of CNCs have been studied in the literature using confocal laser scanning microscopy and light scattering.¹⁷⁴

CNCs are also used to stabilize Pickering emulsions since CNCs can be adsorbed at the oil-water interface.^{181,182} Pickering emulsions employ solid particles as stabilizers which accumulate at the interface between two immiscible liquids and stabilize droplets against coalescence.¹⁸³ The adsorption process of the CNCs at the oil-water interface was attributed to the (2 0 0) crystalline plane of the CNC which is believed to be more hydrophobic than the other CNC faces. The crystal planes (1 1 0) and (1 -1 0) of CNCs are more hydrophilic and moderately rough which are responsible for the good dispersibility in water. On the other hand, the (2 0 0) plane of CNC is flat

and includes CH groups which orient toward the oil phase in the case of Pickering emulsions.¹⁸² In addition, the CNC particle surface must be partially wetted both by water and oil in order to stabilize emulsions. The contact angle of the particles at the oil-water interface give an indication of the wettability of the particles.¹⁸⁴ For rod-shaped CNC particles, the contact angle of the particles at the oil-water interface is below 90° and they are wet preferably by the water phase, leading to oil-in-water (O/W) emulsions.¹⁸⁵

2.6. Chiral nematic structure of CNCs

Cellulose nanocrystals are good candidates to obtain structurally colored films since they form chiral nematic structures.¹⁶ An example of such structural coloration was already shown in Pollia fruit (Figure 2-8). In the case of colloidal suspensions, CNCs are isotropically oriented at very low concentrations whereas at increasing concentration CNCs in suspension align and develop long-range order. Owing to their longitudinal twist CNCs assemble into a helicoidal arrangement at increased concentrations.¹²⁸ This is called a chiral nematic (cholesteric) phase. The chiral nematic self-assembly consists of layers of particles that align along a vector (director), with the orientation of each director rotated slightly about the helicoidal (cholesteric) axis from one layer to the next as illustrated in Figure 2-12a.¹¹

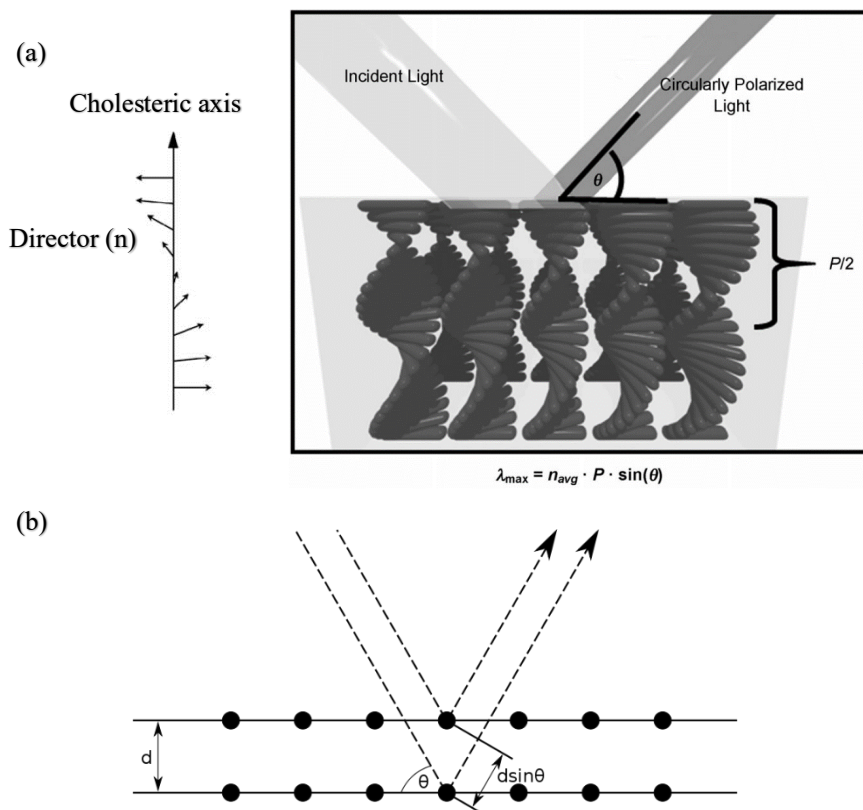


Figure 2-12 (a) Chiral nematic structure of CNCs with a helical pitch length, P and (b) Bragg diffraction (Reproduced with permission from the publisher¹⁸⁶)

Beginning of the formation of this assembly can be proved with the observance of tactoids (Figure 2-13). These initial assemblies, the tactoids, can merge and coalesce at increased concentration of particles to form larger tactoids. The main characteristic of this behavior can be attained by visualization of the fingerprint textures when these samples are viewed under cross-polarized light.¹⁸⁷

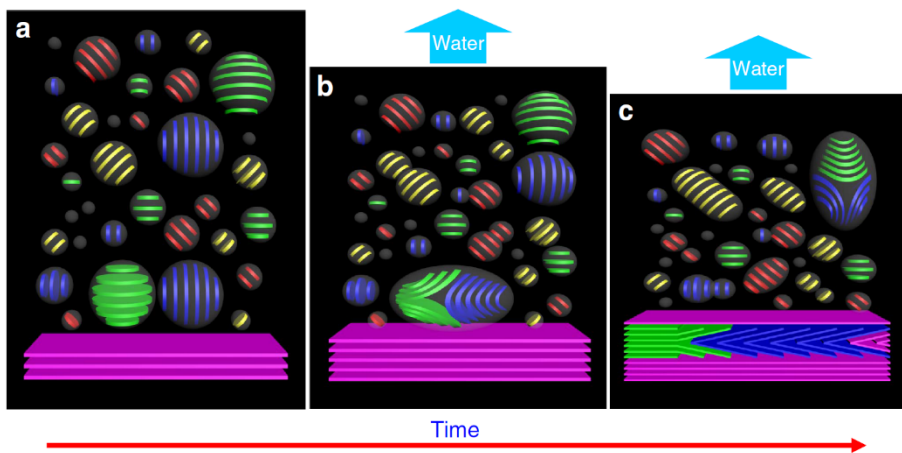


Figure 2-13 Cartoon depictions of the tactoids and their transformations as the solvent evaporates from the CNC suspension (Reproduced with permission from the publisher¹⁸⁸)

Colloidal CNCs can be assembled via evaporation-induced self-assembly. Interaction of light with these assemblies can be understood by Bragg diffraction since twisted layers resemble crystal lattices. Bragg diffraction (Figure 2-12b) occurs when electromagnetic radiation having a wavelength comparable to consecutive crystallographic planes is scattered by different lattice planes that remain separated by the d interplanar distance. Therefore, depending on the wavelength of the incident wave (λ), these scattered waves are able to interfere constructively according to Bragg law (Equation 2.3):

$$m\lambda = 2d\sin(\theta) \quad (2.3)$$

where m is a positive integer and θ is the incident angle.

The relation between the pitch length of the chiral nematic assembly, i.e. the distance required to complete a full rotation of the director, and reflected wavelength is then formulated by Equation 2.4, where λ_{max} is the reflected light wavelength, n is the refractive index of the film, P is the helical pitch and θ is the incident angle of the light with respect to the surface of the film (Figure 2-12a).^{92,189,190}

$$\lambda_{max} = nP \sin(\theta) \quad (2.4)$$

Thus, the pitch length of the chiral nematic assembly must be controlled to achieve the desired wavelength of the reflected light. For instance, it has been reported that the concentration of the CNCs in drying colloidal films has an influence on the pitch distance (P) as depicted (Figure 2-14).¹⁹¹ In the dilute regime CNC suspensions are isotropic and they do not have any helical assembly. When a critical concentration is reached, chiral nematic phases form and coexist with the isotropic phase. The volume fraction of each phase in this biphasic region depends on the characteristics of CNCs and suspension behavior.¹⁵ Increasing the concentration further reduces the isotropic phase to zero and the suspension exhibits a fully chiral nematic phase. Further increases in concentration of the suspension then causes a linear decrease in the helical pitch length.¹² The pitch values follow a power law of $P \propto c^{-1}$ as explained by Straley.¹⁹² In this model, the pitch length is proportional to the ratio of two elastic constants (K_t/K_{22}). K_t is called twist constant which is characterized by the contribution of the free energy of a chiral nematics influenced by the torque a chiral molecule exerts on its neighbor whereas K_{22} is called twist elastic constant (Frank elastic constant) which defines the creation of an elastically distorted state described in the Frank-Oseen elastic free energy density.^{193,194} It has been reported that K_{22} is dependent on the concentration changes for rod-like viruses which gives an account of the dependence of the pitch length on the concentration of the suspension.¹⁹³ For CNC suspension, the power law is followed by a possible gel formation which constrains a further decrease in P . Lastly, the final pitch of the CNC film depends on where along the line A–E the structure of the suspension is frozen.

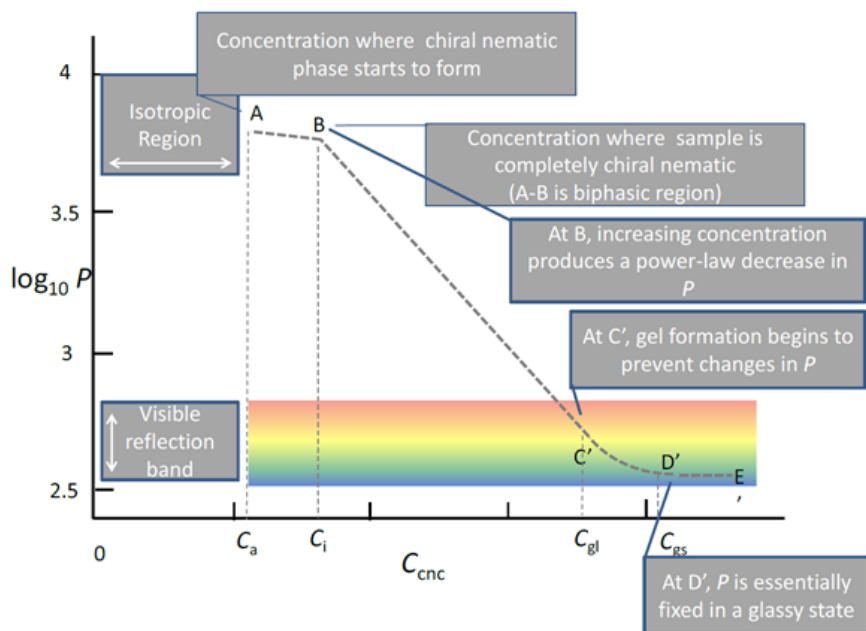


Figure 2-14 Concentration dependence of the chiral nematic pitch length and range of pitch length that reflect visible light (Reproduced with permission from the publisher¹⁹¹)

2.7. CNCs based films

The chiral nematic structures of the CNCs could also be retained upon solvent evaporation to obtain solid films showing iridescence.¹¹ SEM images of the cross section of the films after film fracture surface give a clear indication of the pitch, handedness and direction of the chiral nematic director.¹⁹⁵ Self-assembly of colloidal CNCs in dried films are governed by initial suspension behavior and its changes during drying process. Several parameters determine the assembly of CNCs in aqueous suspensions. These are mainly the shape of the CNCs, the electrostatic interactions between particles and the ionic strength of the medium.¹⁹⁶ In addition, external elements such as exposure to magnetic, electric, or shear fields can be employed to control the alignment of CNCs.^{197,198,199,200} For instance, the orientation of cholesteric phases of CNCs could be controlled at low electric fields whereas

unwinding of the cholesteric structure was achieved at high electric fields.¹⁹⁸ However in such studies, CNCs were dispersed in an apolar solvent (toluene) to be able to apply strong electric fields over large distances in the suspension to align the CNCs parallel to the electric field. To avoid aggregation of CNCs, surfactants were added to CNC dispersions in toluene. In another example, NdFeB magnets were used to improve the homogeneity of the chiral nematic pitch and the orientation of the particles.¹⁹⁹ The orientation of cholesteric suspensions in magnetic fields is attributed to the intrinsic anisotropic diamagnetic susceptibility of the individual CNCs.²⁰¹ In addition, shear-oriented CNC films have been obtained to characterize the effect of the alignment of CNCs on the coefficient of thermal expansion of the films.²⁰⁰ It was concluded that the oriented CNC films, obtained by applying shear, exhibited a highly anisotropic in-plane thermal expansion whereas CNC films without preferential orientation displayed isotropic thermal expansion. The effect of the shear speed on the orientational order of CNC suspension was also studied by grazing incidence wide-angle X-ray scattering (GI-WAXS).²⁰² It was reported that the shear speed was controlling the alignment of CNCs at low casting temperatures whereas evaporation affected the film formation at the high casting temperatures.

Several parameters such as ionic strength, temperature, and suspension concentration controlling chiral nematic structure of CNCs have also been introduced and their effect on the pitch length distance in dried films was analyzed.¹⁷¹ It was reported that the chiral nematic pitch of the anisotropic phase decreased with increasing particle concentration and with added electrolyte concentration (HCl, NaCl, and KCl).¹⁷⁶ Pitch length can also be tuned by sonication of the CNC suspension.^{203,204} In addition to the fact that ultrasound treatment of CNC suspension increased the chiral nematic pitch (Equation 2.4), increased energy of ultrasound in CNC suspension prior to drying also induced a red-shift in the reflection wavelength of CNC films.

Furthermore, the addition of salt^{171,172,205}, polymers such as poly(vinyl alcohol) (PVA)¹⁶⁷, anionic polyacrylate¹⁶⁸, and waterborne polyurethane²⁰⁶, organic linkers such as glycerol²⁰⁷, poly(ethylene glycol) (PEG)²⁰⁸, or inorganic nanoparticles such as gold^{209,210} and silver²¹¹ to CNC suspension have also been studied to understand the effects of these additives on the self-assembly behavior of cellulose nanocrystals.

The selection of the additives depends on the desired property to be modified. For instance, an anionic polymer, sodium polyacrylate (PAAS), was used to modulate the CNC film coloration, while a neutral polymer, polyethylene glycol (PEG), was used to improve the CNC film flexibility.¹⁶⁹ In another example, chiral plasmonic films were formed by combination of gold nanorods and CNCs.²¹² The concentration, size, and surface charge of spherical gold nanoparticles were altered to modify the structure and optical properties of the CNC films. It was concluded that the concentration of gold nanoparticles had the strongest effect on the properties of the composite films, when compared to the effect of gold nanoparticle size and surface charge. Ionic liquids were also used to modify the mechanical, optical and thermal processability of CNC films.²¹³ It was shown that the flexibility of CNC films was increased with the addition of 1-allyl-3-methylimidazolium chloride (AmimCl) which also induced a red-shift in the reflected wavelength of the produced films. The red shift of reflected wavelength is attributed to some changes in n and P as explained in Equation 2.4.

2.8. Methods of film formation

Several methodologies (Figure 2-15) have been reported to obtain CNC films, including blade coating,²⁰⁰ dip coating,²¹⁴ Langmuir–Schaeffer,²¹⁵ Langmuir–Blodgett,²¹⁶ layer-by-layer assembly,²¹⁷ spin coating,^{218,219} a combination of spin coating and layer-by-layer assembly,²²⁰ and drop-casting^{12,221,222}. Each method has its own merit to control film thickness or packing density. For example, the Langmuir–Blodgett and Langmuir–Schaeffer methods have the ability to control the packing density of the particles whereas spin coating and dip coating cannot achieve the same level of control.²¹⁶ In the Langmuir–Schaeffer method, a CNC suspension was first mixed with cationic surfactant which enabled CNCs to transfer from the air-liquid interface to a solid substrate during horizontal deposition (Figure 2-15b).²¹⁵ The packing density in the obtained films was controlled by changes in the surface pressure at the air-liquid interface prior to the deposition. Spin coating can be a good alternative to produce film with uniform thickness, however, there is no direct control of particle orientation for non-spherical particles in the dried films. It has been observed that spin coating a CNC film caused a loss of iridescence and nanocrystals aligned in the direction of shear.²²³ Research has also been carried out to describe the effect of shear-induced alignment with blade coating or oscillatory microfluidic control of CNC films.^{200,224,225} The results obtained in these studies showed an increased alignment of CNC by balancing the capillary and the shear forces within the film. Application of shear is also demonstrated to be efficient for the mechanical improvements of the composite materials^{226,227} and the break-up of aggregates²²⁸ however, applied shear can also be strong enough to disturb the assembly of CNCs.²²⁹

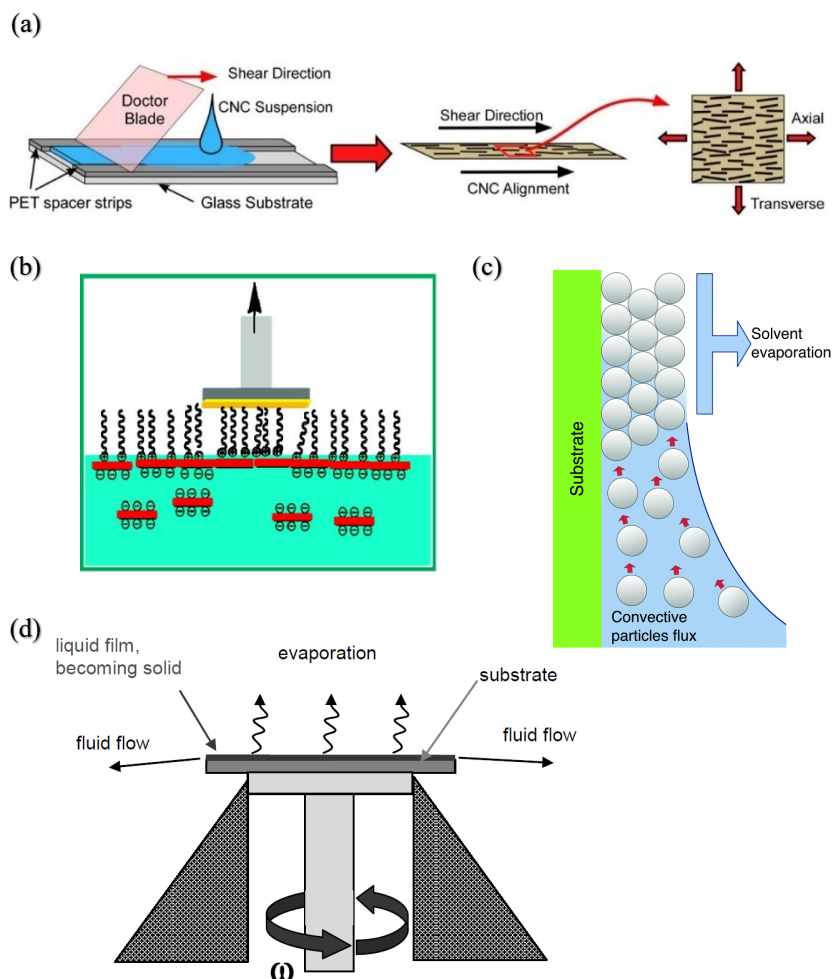


Figure 2-15 Methods of film formation (a) Blade-coating²⁰⁰ (b) Langmuir-Schaeffer²¹⁵ (c) Dip coating⁹¹ and (d) spin coating²³⁰ (Reproduced with permission from the publishers)

Another study was carried out to investigate the color formation in evaporation-induced self-assembly of cellulose nanocrystal films in which the CNC suspension was evaporated inside a petri dish.¹¹ Multi-colored domains have been observed due to the differences in self-assembly of particles in different domains. Confined assembly of CNCs have been studied via several approaches.

For instance, aligned CNCs deposits on a surface were obtained *via* a wrinkled template-mediated printing process.^{231,232} This method was adapted from a process developed to obtain gold nanoparticle arrays.^{233,234} In this approach, CNCs were aligned within pre-wrinkled template polydimethylsiloxane (PDMS) grooves and cast onto the substrate. In another example, the self-assembly of cellulose nanocrystals was achieved within shrinking, micron-sized aqueous droplets.¹⁵ The study showed the effects of the confined geometry on the chiral nematic assembly of CNCs which correlates the concentration of the particles and pitch length of the chiral nematic assembly. In other words, this configuration enables the observation of the microdroplet shrinkage process by polarized optical microscopy and thus the evolution of pitch, which depicts the behavior of the cholesteric phase from low concentration at the equilibrium towards the final dry state. CNC films were also obtained via drying CNC suspension between two glass substrates to investigate the effect of surface anchoring on the evolution of chiral nematic helix orientation and pitch during drying.²³⁵ It was shown that slow drying of anchored CNC dispersions on an orbital mixer resulted in films with larger areas of uniform color reflectance. Alternatively, drop-casting and evaporation of CNC suspensions have also been investigated.^{12,221} Drop-casting is a relatively simple method which does not require advanced instrumentation and films can be generated onto relatively small substrates without wasting material. One of the biggest drawbacks of drop-casting is that the obtained films tend to have a non-uniform film thickness due to differences in evaporation rates across the drop causing capillary flow inside drop. There have been several attempts to avoid this problem for CNC films. For example, inkjet printing of CNC films has been carried out onto the aqua regia cleaned quartz substrates to induce attractive electrostatic interactions between the nanocrystals and the substrate.⁴⁸ However, inkjet printing was limited to less concentrated systems and there was no proof of iridescent formation in obtained CNCs films (Figure 2-16). Besides, deposits exhibit coffee-ring pattern as shown in Figure 2-16.

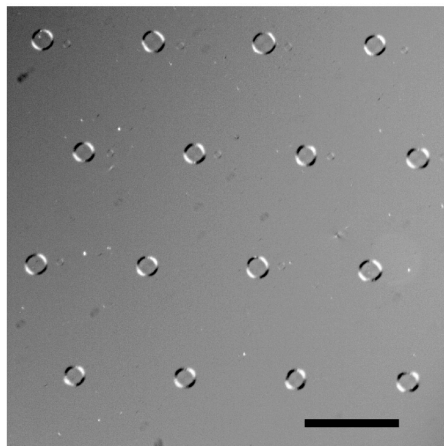


Figure 2-16 Cellulose micropattern on glass obtained by printing a 0.76 wt% cellulose nanocrystal suspension into a ring deposits (Scale bar: 300 μm) (Reproduced with permission from the publisher ⁴⁸)

In other examples, the coffee-ring effect has been observed in dried CNC films and the control over the chiral nematic pitch length was achieved by adding glucose to the suspension prior to drying.^{12,221} A qualitative explanation of pitch length changes in different concentration regimes was described and these changes were related to the reflected wavelength of light.¹² In a similar example, self-assembly of CNCs were studied by drying colloidal drop onto a meshed supports.²³⁶ The process of thin film formation is illustrated in Figure 2-17 where the particle concentration increases upon drying, which leads to CNC self-assembly into larger structures, i.e. tactoids that form the suspended film. The effect of mesh morphology on the optical properties of CNC films was further investigated. Using larger mesh opening sizes resulted in thicker and less even films. Despite all this work, there still remains a need for the characterization of dynamic evolution of colloidal drops in terms of the concentration changes and the surface behavior during drying.

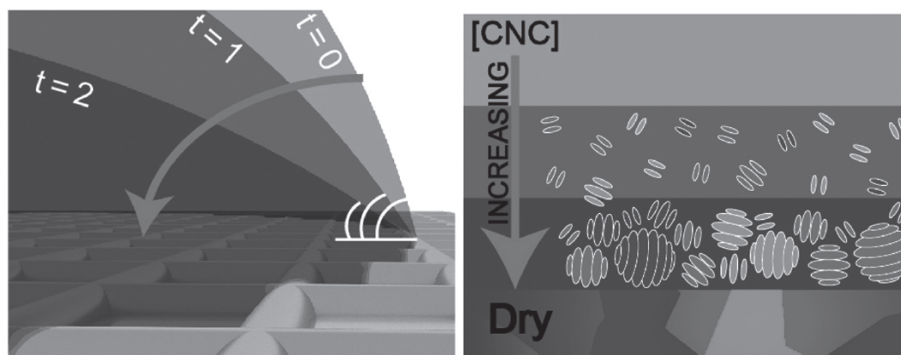


Figure 2-17 Evaporation of sessile colloidal drop of CNCs onto a meshed substrate (Reproduced with permission from the publisher ²³⁶)

2.9. Applications of CNC films

In the case of CNC films, research has mainly focused on the application of photonic materials, anti-counterfeit, decorative, and antireflective coatings, and optical filters.^{123,196,237} These are the main interests in the development of new materials as CNC suspensions readily form a chiral nematic phase. On the other hand, CNCs can also be used as a template to produce chiral nematic mesoporous resins.²³⁸ In principle, chiral mesoporous material can be prepared by the selective removal of one component in a composite of CNCs and the material of interest such as silica or polymer.²³⁹ Thus, chirality can be induced for porous inorganic solids which can be used to produce new types of materials for chiral separation, stereospecific catalysis, chiral recognition and photonic materials after removal of the CNC template. In a similar manner, the self-assembly of CNCs with hydrogel precursors leads to nanocomposites with long-range chiral nematic order. In such applications, hydrogel swelling can be controlled to have tunable iridescence.²⁴⁰ Stimuli-responsive films can be used for instance as humidity sensors which can be used in the food industry.²⁴¹ Dense films of CNCs can be used as scaffold material for cell cultures in applications of tissue engineering.²⁴² In another example, detection of aldehyde gases was achieved by CNC films.²⁴³ The surface of CNCs were grafted with amine groups to produce

colorimetric sensors that change color when exposed to aldehyde gases such as formaldehyde or propanal.

In general, solvent casting is a preferred strategy to fabricate nanocomposite films containing CNCs as nanofillers. Other methods such as 3D printing are also investigated for CNC suspensions and to provide iridescence throughout the film while maintaining the chiral structure. Viscoelastic inks from CNC suspensions can be produced for patterning 3D objects by direct ink writing.²⁴⁴ For instance, 3D printing of CNC particles suspended in either water or a photopolymerizable monomer solution is used to produce three dimensional CNC based architectures.^{245,246} In order to have control over extrusion and patterning, finite yield stresses are required for the suspensions. These rheological properties can be achieved with higher weight concentrated suspensions or thickening agent for low concentrated systems. In addition, the alignment of CNCs can be achieved by the applied shear forces during the extrusion process. CNCs have also been reported to show great potential in printed electronic applications.²⁴⁷ CNCs can be used as an additive in conductive ink formulations to be used as stabilizing agent or they can be employed as a bio-template or a capping agent for metallic nanoparticles synthesis.

2.10. Conclusions

CNCs can be used to produce films which exhibit structural color. This structural color occurs because of the interaction of light with chiral nematic structures preserved in the films, causing a diffraction of light of a specific wavelength. There have been several studies to control chiral nematic assembly as explained in Section 2.7. These studies have mostly focused on the self-assembly behavior in the aqueous phase. On the other hand, there is a need for understanding the film formation to regulate structural color formation in dried films.

A number of methods have been employed to produce CNC films (Section 2.8), however there is a lack of achieving control over the colloidal deposition of CNCs. One of the examples of this case is observed for the evaporation of drop-casted CNC suspension. Although there have been some studies where CNC films were obtained by drop-casting, the colloidal deposition of the particles was not controlled to suppress the coffee-ring effect. Non-uniform deposition of the particles can be problematic for the applications such as ink-jet printing, spray coating, and evaporation-induced colloidal self-assembly. In addition, the changes of the concentration in drying CNC drops were not determined which is crucial to characterize the suspension behavior including viscosity and liquid crystalline phase behavior. In this work, a new approach is introduced to determine the concentration changes in drying colloidal drops. The flow behavior inside the drying drops is analyzed by interpreting the dimensionless numbers which enable to direct the colloidal deposition pattern. Following that, several strategies will be investigated to control the colloidal deposition of CNCs and to analyze the effects of this control on the structural color formation.

3. Materials and Methods

3.1. Materials

Cotton wool (German pharmacopeia grade, Hartmann, Germany), isopropanol (99.5%, HPLC grade), sodium hydroxide (99%, pellets) and calcium chloride (96 %, granular) were purchased from Carl Roth GmbH. Sodium chloride (99.5%) was purchased from Fisher Scientific. Sulfuric acid (95 %, RECTAPUR) and ethanol (96%, Analar Normapur) were purchased from VWR International. Tetraethyl orthosilicate (TEOS, 99.9% trace metals basis), poly-L-lysine solution (0.1% w/v in water) and ammonium hydroxide were purchased from Sigma Aldrich.

H₁H₁H₂H₂H-Perfluorooctyltriethoxysilane (FAS) was obtained from J&K Scientific. Dialysis membranes (molecular weight cut-off 12–14 kDa) were purchased from SpectrumLabs. Amberlite MB-6113 (for ion chromatography, mixed resin) and potassium carbonate (99%) were purchased from Acros Organics. Glass microscope slides (soda-lime glass) were produced by Knittel Glaser (Germany) and were made in accordance to international standard ISO 8037/1 ($n = 1,53 \pm 0,02$) and were purchased from MLS NV (Belgium). Glass circular cover slides (borosilicate, 10 mm diameter, ($n = 1,52 \pm 0,01$)) were purchased from Agar Scientific (U.K.). Wilmad ® NMR tubes (5 mm diameter) used in DDLS measurements were purchased from Sigma Aldrich. Capillary tubes (rectangular glass 0.4x4.0 mm) were purchased from VitroCom. All materials were used as received unless otherwise stated.

3.2. Preparation of Cellulose Nanocrystal (CNC)

Suspensions

A cellulose nanocrystal suspension was obtained via sulfuric acid (10.06 M) hydrolysis of cotton wool over 40 min at 45 °C using the same procedure for all suspensions used in this thesis. Cotton wool pieces were added to pre-heated (45 °C) sulfuric acid solution (10.06 M) and mixed with a mechanical overhead stirrer (Heidolph Instruments).

At the end of the hydrolysis, the obtained product was diluted with 1 L water and centrifuged 5 times at 10 °C, 10000 rpm with intermitted distilled water washes and

decantation of the supernatant to remove excess acid. After the centrifugation steps, samples were dialyzed against deionized water for 48 h using a dialysis membrane (MWCO 12–14 kDa). The nanocrystal suspension was homogenized using a Branson Digital Sonifier, aliquots of 300 mL of suspension were sonicated for 3 minutes at amplitude 25% before filtration through a No. 2 fritted filter to remove remaining aggregates. The suspension was then mixed with Amberlite MB6113 resin to remove excess non-H⁺ and OH⁻ ions in solution. The resin was subsequently removed by filtration. The obtained initial aqueous suspension was then concentrated to the desired concentrations by evaporating excess water by rotary evaporation. The bath temperature of the rotary evaporator was increased to 60 °C and vacuum pressure was set to 72 mbar. The weight concentration of the cellulose nanocrystal suspensions was then determined by thermogravimetric analysis. Thermogravimetric analysis (TGA) was carried out with a Netzsch F3 Tarsus under nitrogen atmosphere. The CNC suspensions were heated at 10 °C min⁻¹ to 85 °C, followed by an isothermal period for 30 min. The concentration of stock suspensions was determined from three measurements of the residual mass and the standard deviation was calculated to be 0.2 wt%.

3.3. Characterization of Cellulose Nanocrystals

3.3.1. Crystallinity of Cellulose Nanocrystals

X-ray diffraction was used to determine the index of crystallinity of the prepared CNCs. In order to carry out measurements, solid CNCs were obtained via freeze drying of a CNC suspension after it was flash-frozen in liquid nitrogen. The CNC powder was analyzed on a zero-background silicon sample holder. X-ray diffractograms were recorded on a PANalytical X'Pert Pro multi-purpose diffractometer in Bragg-Brentano parafocusing geometry, with monochromated Cu K_α ($\lambda = 1.5406\text{\AA}$, 45 kV, 40 mA) radiation, automated divergence and receiving slits (10 mm illuminated length), 10 mm beam mask, 0.04 rad soller slits, and a step size of 0.02°. The empty sample holder was used as an instrumental background. Profex software was used to perform Rietveld refinement fitting the experimental data using

the cellulose I_β pattern from Nishiyama *et al.*²⁴⁸ The experimental data and calculated refinement fit are shown in Figure 3-1. It was observed that the diffraction intensities are influenced by the sample orientation. The diffraction pattern of the cellulose I_β from Nishiyama *et al.*²⁴⁸ includes preferred orientation which causes a difference in the fitted profile at around 21° (Figure 3-1). The crystallinity index (χ_c) of cellulose was calculated based on the method by Thygesen *et al.*²⁴⁹ as described by Equation 3.1 where $I_c(s)$ is the intensity at a particular vector due to crystalline material, $I(s)$ is the total intensity at a particular vector where the scattering vector (s) is given by $s = 2 \sin\theta / \lambda$. The limits of integration were chosen as s_0 at $2\theta = 10^\circ$ and s_1 at $2\theta = 40^\circ$.

$$\chi_c = \int_{s_0}^{s_1} I_c(s) s^2 ds / \int_{s_0}^{s_1} I(s) s^2 ds \quad (3.1)$$

The crystallinity index (χ_c) was calculated to be ~ 0.84 using the data in Figure 3-1. Concha *et al.*²⁵⁰ reported the crystallinity index of cotton cellulose as 0.90. However, it has to be noted that the analysis method can significantly alter the determined crystallinity index as studied by Svedström *et al.*²⁵¹

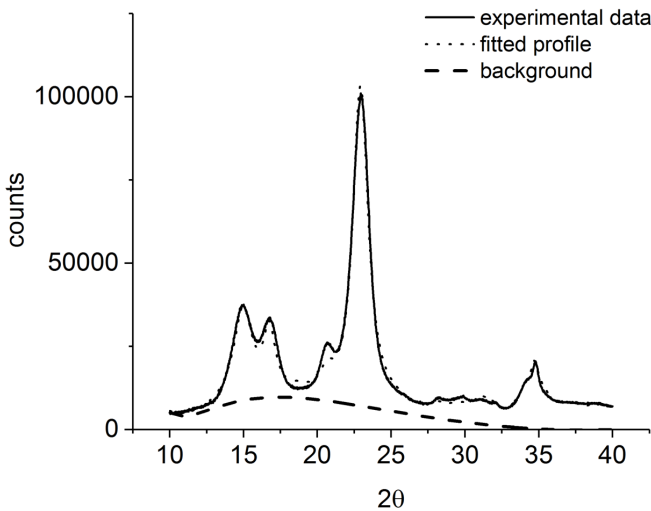


Figure 3-1 Diffractogram of CNCs and refinement data

3.3.2. Size Distribution of Cellulose Nanocrystals

There are several methods proposed to characterize the size distribution of CNCs. They include transmission electron microscopy (TEM), atomic force microscopy (AFM), small-angle X-ray scattering as described in Section 2.4.2.^{144,141,147} Examples of TEM images can be seen in Figure 2-5 in which a small number of particles can be visualized directly.¹³⁹ Although TEM images gave an idea about the size and shape of the particles, it gets difficult to analyze the size distribution of the particles since the number of particles imaged are limited. Increasing the concentration of initial suspensions to be able to record larger number of the particles causes problems associated with the aggregation of the particles during drying.¹⁴⁰ In addition, the contrast in TEM images is affected by the electron density of the material. This also causes problems in case of the imaging of cellulosic materials which are made of carbon having low electron density. A stain containing heavy metal salt such as uranyl acetate is often used to increase the contrast of the images. Staining procedure can also cause aggregation of CNCs which impair the characterization of individual nanocrystals. Besides, uranyl acetate which is commonly used as a stain is a toxic and radioactive material which has to be used in a cautious manner for health and environmental safety.¹⁴⁶

In order to characterize the size distribution of CNCs, atomic force microscopy (AFM) was used in this work. Sample preparation is easier for AFM measurements with respect to TEM experiments since it does not require staining of the samples. Particles size analysis of the samples by AFM also requires well-dispersed particles which are deposited on a flat substrate. Additionally, the anchoring of the CNCs are necessary to avoid slipping problem of the particles due to dragging by the AFM tip. For this reason, a cationic polymer adhesive was deposited onto the substrates prior to CNC deposition. In this work, 20 μ L poly-L-lysine solution (Sigma Aldrich, 0.1% w/v in water) was deposited on a freshly cleaved mica surface (NanoAndMore GMBH) for 3 minutes and subsequently rinsed with deionized water. The surface treated mica was dried with compressed air. 20 μ L of a CNC dispersion (0.001 wt%) was placed on the treated surface for 3 minutes, then rinsed with deionized water, and dried with

compressed air. The sample were left in a vacuum oven at 40°C overnight before analysis. A Multi-mode V AFM (Digital instruments Nanoscope Veeco) was used in tapping mode with AFM probes from Budget Sensors (Tap300 Al-G, resonance frequency 300 kHz and force constant 40 N/m) to image the samples. The length of 300 particles was measured manually using ImageJ and the mean length and standard deviation were determined. The average and standard deviation is 225 ± 93 nm and the log-normal fit resulted in 201 nm as shown in Figure 3-2. The width of particles cannot be determined accurately due to AFM tip broadening.

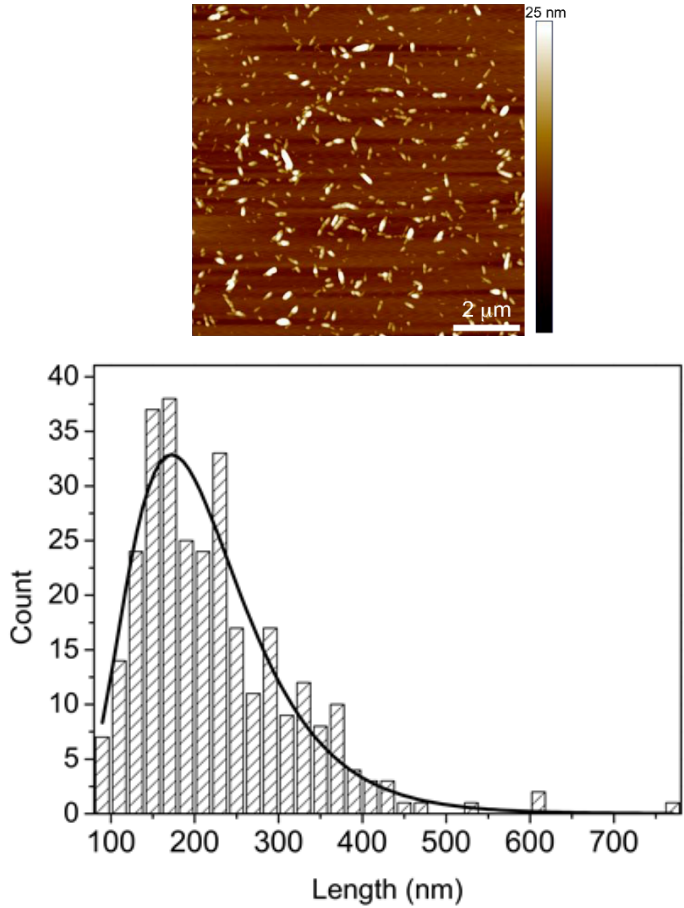


Figure 3-2 Atomic force microscopy image of cellulose nanocrystals and length distribution extracted from AFM image

3.3.3. Determination of Sulfate Ester Groups

The number of sulfate ester groups was determined independently by elemental analysis and by acid-base titration, as previously reported.¹⁵⁷ Comparable results were obtained, as shown in Table 3.1. Elemental analysis data (nitrogen, sulfur) were collected on a Thermo Flash 2000 elemental analyzer (Thermo Fisher Scientific, Inc.) using enriched phenanthrene as a calibration standard with linear calibration. Nitrogen and sulfur content were reported as mass percentage of the total sample. Acid-base titration was performed using a SI Analytics Titroline 6000 autotitrator. Three independent titrations shown in Figure 3-3 were performed using sodium hydroxide (99%, p.a., ISO, in pellets, purchased from Carl Roth), which was previously standardized with oxalic acid (> 99.5%, purchased from VWR). The concentration of cellulose nanocrystals used in the acid-base experiment was 2.6 wt%, as previously determined by thermogravimetric analysis (TGA).

Table 3.1 Concentration of sulfate ester groups of CNCs determined from two independent techniques

Technique employed	Concentration of sulfate ester groups (mmoles/gCNCs)
Elemental analysis	0.24 ± 0.01
Acid base titration	0.28 ± 0.01

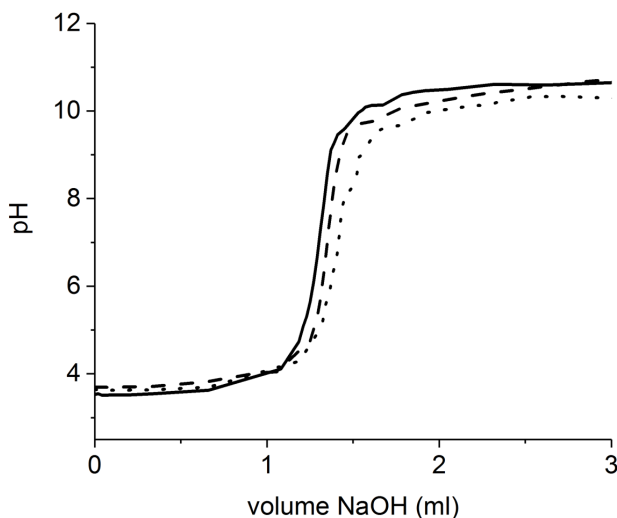


Figure 3-3 Titration of sulfated CNCs (2 mL, 2.6 wt%) with sodium hydroxide (0.01 M)

3.4. Film Deposition

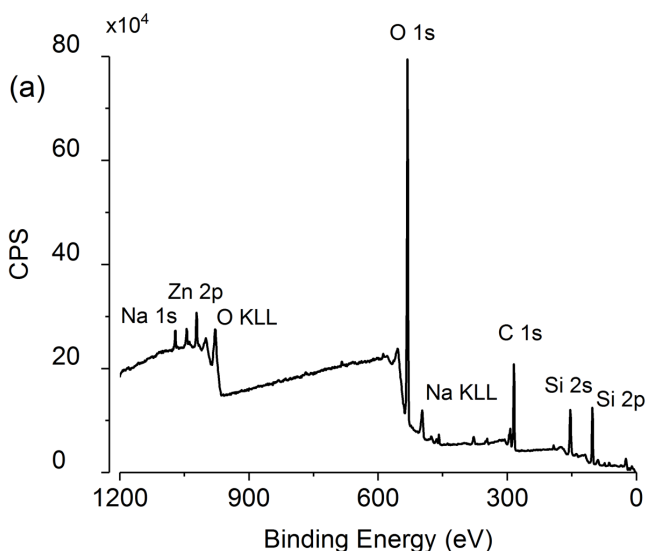
In a typical experiment a droplet of aqueous CNC suspension is deposited on a glass substrate and allowed to evaporate. Glass microscope slides and cover slides were rinsed with isopropanol and dried with compressed air prior to film casting. Glass slides being transparent are chosen for the ease of optical characterization of the CNC films. An aluminum optical breadboard (Thorlabs) was used to achieve stability and consistency in the deposition setup. Leveling of the sample stage is fundamental to obtain symmetric films. Glass slides were put on a goniometer stage (Thorlabs, GN2) which is mounted on the aluminum optical breadboard. A round bubble level (Manutan) was used to assure the leveling of the stage. Each film was prepared by depositing 10 μL of a suspension of cellulose nanocrystals with a specific concentration or component. For pipetting, Eppendorf research plus single channel pipette (10 μL) and tips (Eppendorf epT.I.P.S.) were used which are tested in accordance to international standard ISO8655:2002.

The weight concentration of the initial cellulose nanocrystal suspensions was determined by thermogravimetric analysis as described earlier in Section 3.2. Saturated aqueous solutions of K_2CO_3 (40% RH) were used in a closed desiccator (25 cm nominal size) to obtain environment with a controlled specific relative humidity.²⁵² In chapter 5, ethanol was mixed with desired amount of water to 100 mL inside a closed desiccator (25 cm nominal size) to obtain an environment containing a controlled amount of ethanol vapor.

In chapter 6, cellulose nanocrystal suspension were mixed with sodium chloride or calcium chloride to obtain the desired ionic strength prior to casting onto a dust-free cover slide. Drops were cast immediately after the CNC suspension was mixed with the desired salt to avoid gelation time effects, as it was noticed that leaving the suspension to equilibrate led to the formation of hydrogels at higher ionic strength as expected from other literature reports.^{172,178,179}

In chapter 7, superhydrophobic substrates were prepared via coating glass substrates by sol evaporation.²⁵³ In order to prepare the sol, Tetraethyl orthosilicate (TEOS, 5 mL), together with 1H,1H,2H,2H-Perfluorooctyltriethoxysilane (FAS, 1 mL) was dissolved in 25 mL ethanol. The solution was mixed with ammonium hydroxide/ethanol solution (6 mL 28% $NH_3 \cdot H_2O$ in 25 mL ethanol), and stirred intensively at room temperature for 24 hr. The mixture was sonicated in a bath sonicator for half an hour and 10 mm glass covers were coated with a drop of a mixture and dried at room temperature and cured at 100 °C.

X-ray photoelectron spectroscopy was employed to characterize the elemental composition on the surface of glass before and after the coating. XPS spectra (Figure 3-4) was recorded on a Kratos Axis Supra photoelectron spectrometer employing a monochromated aluminium $K\alpha$ ($h\nu = 1486.7$ eV, 150 W emission) X-ray source, hybrid combined magnetic-electrostatic optics, a hemisphere analyser and delay-line detector. The analyser was operated in fixed-analyser transmission mode with a pass energy of 160 eV. Charge neutralization was performed using a low-energy electron flood gun within the field of the magnetic immersion lens. Analysis chamber pressure was $<5 \times 10^{-8}$ mbar during analyses. Binding energy was referenced to aliphatic carbon at 285 eV. Empirical relative sensitivity factors supplied by Kratos Analytical (Manchester, UK) were used for quantification. Homogeneous sample composition within the information depth was assumed and no correction was made for matrix effects. The XPS peak at 688 eV is attributable to F 1s, suggesting that the glass was coated with fluorinated alkyl silane (FAS) (Figure 3-4b). A peltier heating stage (PE 120, Linkam) was used to regulate the temperature of the substrate in thermal Marangoni flow studies (Section 7.2.1.).



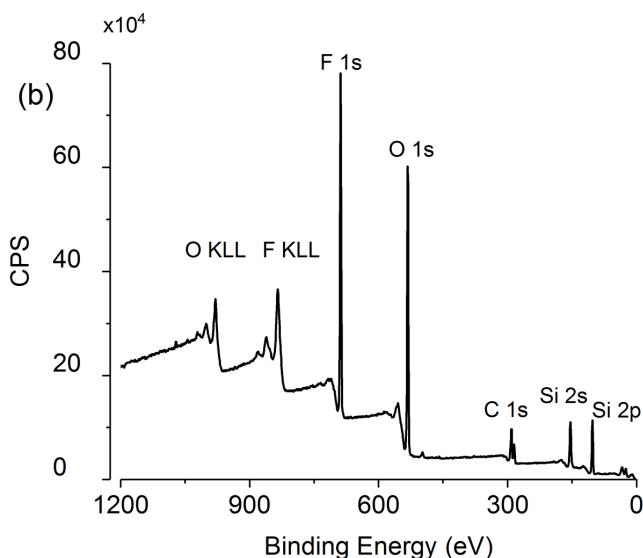


Figure 3-4 XPS spectra of the (a) glass cover slide and (b) coated glass

Table 3.2 XPS data for glass and coated glass

Orbital	Concentration (At. %)	
	Glass	Coated Glass
Na 1s	1.14	0.24
F 1s	0.46	30.65
O 1s	47.19	33.91
C 1s	27.90	20.58
Si 2p	16.52	14.62

3.5. Droplet Imaging

In chapter 4, sessile droplets were monitored from side with a system adapted from study²⁵⁴. A Canon EOS 1200D camera was coupled with a Plano-Convex Lens $f=50$ mm (Thorlabs) to capture images of sessile droplets. LED lighting was used in the background with a diffuser to create the required contrast between the drop and air. Measurements were analyzed with ImageJ and drop shape analysis software.²⁵⁵ In chapter 6, images of drying droplets were recorded with a camera (DCC 3240C,

Thorlabs) fitted with a zoom lens (MVL7000, Thorlabs) and analyzed with ImageJ to derive the droplet volume versus time. Drop volumes were obtained by acquiring images over time at frame intervals 100 s and fitting the droplet shape with a spherical cap.²⁵⁶ Volume of the drop is given by, $V_{cap} = \frac{1}{6}\pi h(3r^2 + h^2)$ where h is the height of the droplet and r is the contact radius of the droplet. In chapter 7, in order to characterize the temperature gradients at the air-liquid interface of the drop, the drying process of the colloidal drops was monitored with an infrared (IR) camera (A6703sc, FLIR Systems Inc.).

3.6. Cross-Polarized Light Microscopy

Cross-polarized light microscopy images were taken with an Olympus BX51 microscope. The glass slide with a deposited film was placed between crossed polarizers and images were recorded using a digital colour CCD camera (Lumenera Infinity 2 Mpx). For the characterization of the liquid crystalline behavior of CNC suspensions, 30 μL of the suspension were put inside capillary tubes and observed between crossed polarizers.

3.7. Profilometry Measurements

Profilometry was used to determine the height profile of the deposited films through the center point of the deposited films. Profilometer traces were obtained with a Taylor-Hobson 120-L Form Talysurf using a diamond tip with a radius of 2.5 μm and a measurement speed of 0.5 mm/s. This device works with a 120 mm traverse unit with a HeNe laser interferometric transducer (phase grating interferometer). In a typical experiment, a diamond stylus is moved vertically in contact with a sample and then moved laterally across the sample for a specified distance and specified contact force. Surface height variations are measured by tracking the displacement of the stylus tip as a function of position.²⁵⁷ This is done mechanically with a feedback loop that monitors the force from the sample pushing up against the probe as it scans along the surface using phase grating interferometry. A feedback system is used to keep the arm loaded with a specific amount of torque. Changes in the vertical position of the arm holder can then be used to reconstruct the surface.

3.8. Pendant Drop Tensiometry

The surface tension of pendant drops containing different concentrations of CNCs and/or salts was measured with a CAM200 (KSV NIMA) at room temperature. A CCD firewire camera (512x480) with telecentric zoom optics combined with LED based background lighting were used to produce grayscale images of pendant drops for drop shape analysis. Dispense tips (Nordson EFD) with an outer diameter of 0.82 mm and inner diameter of 0.51 mm were selected to create the pendant drops. Before analyzing the shape of the drops, the camera image was calibrated with a solid sphere with a diameter of 2.75 mm. During the measurements, gray level values were assured to be in the optimum range for the required contrast between the drop and the air. The measurement precision was determined using the Worthington number, W_o ,²⁵⁸ which was calculated to be ~ 0.8 . The Worthington number is given by Equation (3.2);

$$W_o = \frac{\Delta\rho g V_d}{\pi\gamma D_n} \quad (3.2)$$

where $\Delta\rho$ is the density difference between drop and the air, g is gravitational acceleration, V_d is the volume of the drop, γ is the surface tension and D_n is the needle diameter. It was reported that including the volume of the drop and the needle diameter in dimensionless number analysis increased the measurement precision.²⁵⁸ In chapter 6, in addition to Worthington number, the accuracy of the surface tension determination of CNC suspensions with added salt was confirmed by the Bond number (Equation 3.3) which was calculated to be ~ 0.3 .

$$B_o = \frac{\Delta\rho g R_d^2}{\gamma} \quad (3.3)$$

where $\Delta\rho$ is the density difference between drop and the air, g is gravitational acceleration, γ is the surface tension and R_d is the radius of the drop. Bond number is a dimensionless number measuring the importance of gravitational forces compared to surface tension. Thus, if the gravitational effects are too small then Bond number gets close to zero.

3.9. Rheological Measurements

An AR-G2 stress-controlled rotational rheometer (TA Instruments) was used to determine the rheological properties (viscosity changes and gelation) of the suspensions. Temperature control was achieved using a Peltier plate with an upper heated fluid bath. All of the suspensions were tested at 20 °C using a double-wall concentric cylinder geometry with gap sizes of 380 and 420 μm . The instrument and the geometry were calibrated prior to testing of the samples in terms of friction and instrument inertia. This geometry was chosen since it has the highest sensitivity for low viscous samples. For each test mentioned in this dissertation, 7 mL of suspension was put inside the geometry. A solvent trap was used to avoid ethanol evaporation for CNC suspensions containing ethanol. Steady shear viscosity versus shear rate curves were obtained for each sample at shear rates between 10 to 100 s^{-1} . The time required to reach steady state was determined by a transient test. For frequency sweep experiments, the linear viscoelastic (LVE) limit was determined by carrying out an amplitude sweep experiment at a frequency of 1.6 Hz.

In chapter 6, the desired concentrations of CNC and salt suspension were reached by adding different concentrations of CNC and salt in water with a volume ratio of 9:1 v/v. Time sweep experiments were carried out at 5% strain and a frequency of 1 Hz. The yield stress values were obtained by fitting steady shear flow data with the Herschel-Bulkley model.²⁵⁹ In order to avoid shear induced reduction of the yield stress values of the mixtures, salt solutions were mixed with CNC suspensions which were already loaded to the geometry.

3.10. Depolarized Dynamic Light Scattering (DDLS)

DDLS measurements were carried out on an ALV 5000 autocorrelator to determine the scattered light electric field time autocorrelation function for each suspension. All measurements were carried out between 30-120 degrees with an angular step of 5 degrees for 300 s. A toluene bath was used around the sample tubes to control the temperature and match the refractive index of the glass sample holder (Wilmad ® NMR tubes 5 mm). Assuming Gaussian statistics for the scattered field, the normalized second-order (intensity) autocorrelation function, $g_2(t)$, is related to the

normalized first-order (electric field) autocorrelation function by the Siegert relation (Equation 3.4).^{260,261}

The normalized first-order (electric field) autocorrelation function, $g_I(t)$, was analyzed to extract the diffusion coefficients as described elsewhere.²⁶² The correlation function, $g_I(t)$, was fitted with Equation 3.5 to obtain the decay constant Γ , where $\Gamma_{VH,1} = 1/\tau_1$ and $\Gamma_{VH,2} = 1/\tau_2$, with τ_i the relaxation time for the slow mode (τ_1) and fast mode (τ_2). The obtained decay constant Γ_{VH} was subsequently fitted with Equation 3.6 to get the rotational and translational diffusion coefficients.²⁶³

$$g_2(t) = 1 + |g_1(t)|^2 \quad (3.4)$$

$$g_1(t) = A_1 \exp(-(\Gamma_{VH,1})t) + A_2 \exp(-(\Gamma_{VH,2})t)^\beta + B \quad (3.5)$$

$$\Gamma_{VH} = q^2 D_T + 6D_R \quad (3.6)$$

The wavevector (q) is given by, $q = \frac{4\pi n}{\lambda} \sin \frac{\theta}{2}$, where n is the refractive index of the medium, λ is the wavelength of the light, and θ the scattering angle i.e. the angle between the propagation direction of the incident light and that of the detected light.

3.11. Zeta Potential Measurements

Zeta potential measurements were carried out on a NanoBrook Omni (Brookhaven) using phase analysis light scattering.^{264,265,266,267} The instrument used a laser light with a wavelength of 640 nm. In this work, a BI-SREL electrode (Solvent resistant electrode assembly) was used for measurements including ethanol whereas BI-ZEL electrode (Electrode assembly for aqueous systems) was used for aqueous CNC suspensions. Consecutive measurements were taken at 20 °C degree for each sample (2 mL) to assure the stability of the cell and laser. To determine the zeta potential of CNCs in water-ethanol mixtures, the cellulose nanocrystal suspension in water was mixed with the desired amount of ethanol whereas for CNC suspensions containing salt, the mixtures were obtained with desired concentrations of salt within the cell. Dielectric constants (permittivity) for ethanol mixtures were taken from reference²⁶⁸.

For all measurements the Smoluchowski model was applied (Equation 3.6).^{266,269,270,271}

$$\mu = \frac{\varepsilon\varepsilon_0\zeta}{\eta} \quad (3.6)$$

Zeta potential, ζ is determined from electrophoretic mobility, μ where ε and ε_0 are the relative and vacuum permittivity respectively and η is the viscosity of the medium. (Water permittivity = 80.56 at 20 °C). In the Smoluchowski limit ($\kappa a \gg 1$), infinitely long rods are oriented parallel to the electric field and ($\kappa L/2 \gg 1$) where κ^{-1} is the double layer thickness, a is the rod radius and L is the length of the rod.²⁷⁰

The content of this chapter was published:

Gençer, A.; Schütz, C.; Thielemans, W., Influence of the Particle Concentration and Marangoni Flow on the Formation of Cellulose Nanocrystal Films. *Langmuir* **2017**, 33 (1), 228-234.

Author Contributions:

A.G. and W.T. developed the concept for the study. A.G. performed the experiments, processed the data, and wrote the manuscript. A.G., C.S., and W.T. interpreted the data and reviewed the manuscript.

4. Deposition of Cellulose Nanocrystal Films

4.1. Introduction

Cellulose nanocrystals (CNCs), rod-like crystalline nanoparticles are a bio-based material that can be a great alternative to obtain films with tunable optical properties. Iridescent and light-diffracting films can be readily obtained by drying a suspension of these CNCs. One of the aims of this research is to understand the colloidal deposition and its effects on the structural color formation in CNC films that is produced via evaporation of the water from the colloidal drop.

Evaporation based colloidal film formation is a dynamic process that involves solvent evaporation, particle transfer, and deposition. As the solvent evaporates some of the properties of the suspension such as the concentration, viscosity and surface tension are subject to change. These changes influence both the self-assembly of the particles and the fluid flow during the drying process. In addition, the fluid flow inside the drying drop governs the transfer of particles, which determines the final shape of the film. Thus, it becomes crucial to understand the characteristics of the particle deposition process together with the self-assembly in the precluding suspension since they have a direct effect on the optical properties and the deposition pattern of the obtained films.

In this chapter we set out to understand the deposition behavior of the particles and the fluid dynamics to be able to control the colloidal deposition pattern and thus the final optical properties of the dried films.

In the first part of this chapter, the determination of the concentration in the colloidal drop during drying is addressed. This will enable us to have a quantitative understanding over the evaporation induced self-assembly of the particles since phase transitions from isotropic to chiral nematic occur as a function of the concentration of the rod-shaped CNCs. We developed a new analytical approach to calculate the concentration changes in drying drop-cast suspensions. This approach is based on the determination of the deposition rate of the film and thus the deposited mass of the film

as a function of time. This information is then used to calculate the remaining mass of particles in the drying drop, which together with information on the time resolved drop volume gives us access to the average particle concentration in the drop during drying. Afterwards, the optical properties of the CNC films are described while analyzing the morphology of the obtained films and looking into detail in the concentration changes in the drying colloidal drops.

In the last part of this chapter, the dynamics of the deposition process are investigated in terms of flow behavior and governing factors including Marangoni flow, particle diffusion, and suspension viscosity. Understanding the effect of each factor on the colloidal deposition using a dimensionless number approach is then used to guide manipulation of the desired parameters to alter the fluid flow and thus the deposition pattern of the films in the following chapters.

4.2. Results and Discussion

4.2.1. Concentration determination in colloidal drops

One of the most important parameters controlling the self-assembly of CNCs is the concentration of the suspension which governs the phase transitions and helical pitch length as described in Section 2.6. Quantitative analysis of the concentration changes is important to understand and describe concentration-dependent self-assembly processes as observed in lyotropic liquid crystals or colloidal glass transitions. This is also valid for studies of CNC-based films in which the concentration is changing during the drying process. However, the determination of the concentration in the bulk of the suspension can be rather complex in the case of colloidal drop drying as particles will leave the suspension as a result of deposition. Figure 4-1 shows images of a drying drop of 3.7 wt% on a hydrophilic substrate at initial deposition and after 30 min. At a later stage during the drying process, the drop is seen to be receding toward the center while a deposit of particles on the substrate can be noticed at beyond the droplet edge (Figure 4-1b). In order to determine the concentration of the receding drop, the amount or mass of particles left within the drop has to be known.

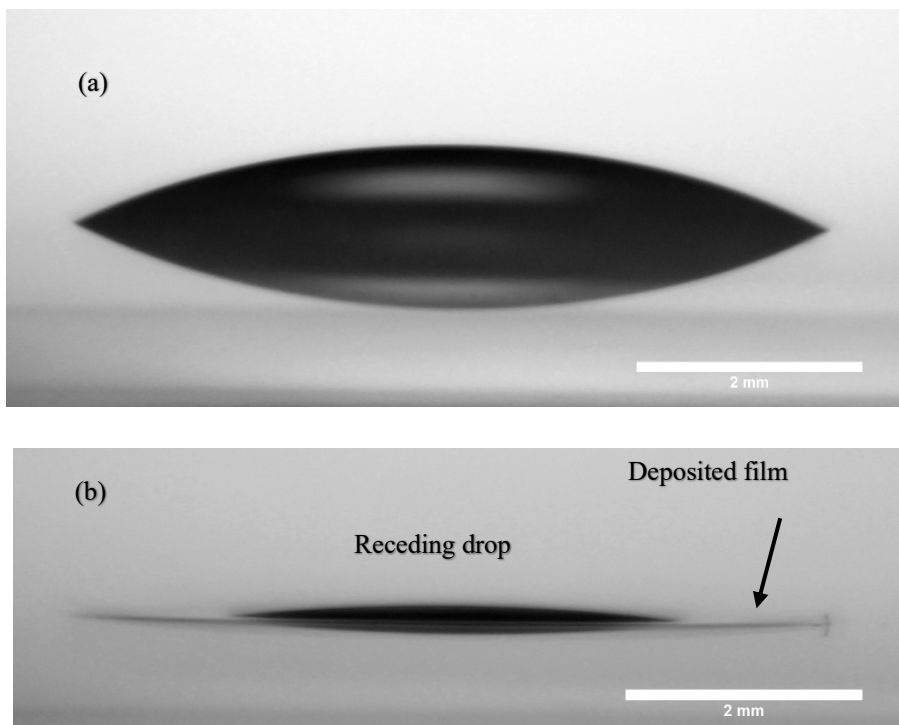


Figure 4-1 (a) Drying of colloidal drop is shown for initially 3.7 wt% CNC suspension
(b) receding drop after 30 min of initial casting

This cannot be achieved using instrumental characterization techniques such as a weighing balance or thermogravimetric analysis. Instead, numerical calculations can be an alternative to solve such a problem. To this end, Deegan *et al.*⁴⁵ introduced an analytical expression to determine the mass of a solute in the deposited ring for drops with a pinned contact line. This expression (Equation 2.1) estimates the ring growth as a power law depending on the evaporation time and the contact angle of the drop. Although this solves mass deposition for thin films with a relatively small height to radius ratio and a constant contact angle, it fails for the larger drops with a more substantial variation in the contact angle with time during evaporation. As a result, this approach is limited to only specific scenarios where the contact angle remains constant. For other cases where the contact angle varies with time the results of ring growth needs to be obtained numerically using computational fluid dynamics.⁵⁹

However, these simulations can be complex due to dynamic boundary conditions at the air-liquid interface and requires a knowledge of particle concentration near the air-liquid interface to solve the diffusion equation of the solvent concentration in the gas phase.²⁷²

Due to these limitations, we proposed a different approach to determine the deposited mass of the particles during the drying process of a colloidal drop and use this to calculate the average particle concentration in the drying drop with time. The key step is to establish the rate of film deposition during the drying of the colloidal drop. This deposition rate is derived by combining information on the film thickness to determine the deposited mass as function of radius, which is extracted from profilometer measurements, and the droplet shrinkage rate which is obtained from time-resolved droplet imaging. The deposition rate (Equation 4.1) is defined by applying the chain rule, thus the change in mass of nanoparticles deposited as a function of time can be expressed as a product of the profilometer profile and the radius change of the evaporating drop with time:

$$\frac{\partial m}{\partial t} = \frac{\partial m}{\partial r} \frac{\partial r}{\partial t} \quad (4.1)$$

The first assumption is that the deposition of the film occurs as the colloidal drop recedes toward the center as illustrated in Figure 4-1. Thus, the analytical expression (Equation 4.2) used for the change in radius as a function of time (dr/dt) for the receding drop can be directly determined from time-resolved measurements of the drying drop and must be equal to that of the change in radius change for the deposited film.

$$\left(\frac{dr}{dt}\right)_{film\ deposition} = \left(-\frac{dr}{dt}\right)_{droplet\ shrinkage} \quad (4.2)$$

The thickness changes of a film, $h(r)$, through the center point can be measured by profilometry and can be used in combination with droplet imaging to determine the

deposition rate. The total area under the profilometer profile $h(r)$ yields M (Equation 4.3), the known total initial mass of the solid particles in the deposited drop:

$$\int_0^{2\pi} \int_0^R h(r) dr d\theta = M \quad (4.3)$$

Once the deposition rate for the films is determined, the absolute deposited mass at any given time is then calculated by the integration of dm/dt and normalized with the initial mass of nanoparticles in the deposited droplet. With this knowledge, it becomes possible to obtain the mass of nanoparticles inside the suspension during drying and, together with the time-resolved evolution of drop volume, to obtain the average concentration of nanoparticles inside the droplet at any time during droplet evaporation.

We used our methodology to characterize the concentration changes in the drying films of CNCs with different initial concentrations. For this reason, a series of films were prepared by evaporation of drop-cast CNC suspensions with different initial mass concentrations. The thickness of these films was measured by profilometry, a technique that also provides information on the final shape of the film (i.e. profile of the cross-section of a film). Increasing the concentration of the initial suspension led to an increase in the accumulation and stacking of particles around the perimeter of the films as illustrated in Figure 4-2. This is due to the coffee-ring effect in which capillary flow carries suspended CNCs particles toward the edge of the droplet during the drying process. It was also observed that films possess uniform thickness around the center except for the film at the intermediate concentration regime which has a pyramid-like deposition.

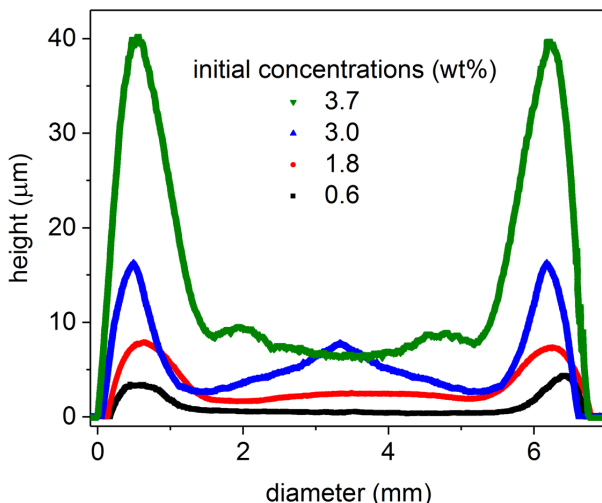


Figure 4-2 Deposition profile of the CNC films with different initial concentrations of colloidal drops

Reproducing of the films requires precise control of levelling of the substrate, stable environmental conditions including temperature and relative humidity, and homogeneity of the CNC suspension. In order to have information on the deposition rate of the films, the droplet imaging (Figure 4-1) was coupled to the data from the profilometry measurements (Figure 4-2). The area under the incremental profilometry slice was used to estimate the deposited mass. The deposition rates of the particles (dm/dt) during film formation (Figure 4-3) were then determined using Equation 4.1. It was found that the drying process can be decomposed into different stages. At the early stage, the deposition rates for all samples appear to increase, as shown in Figure 4-3. For the particular case where a 3.0 wt% CNCs suspension was used to cast a drop, at the first stage the deposition rate increases initial 10 min which is followed by a slight decrease of the deposition rate at the second stage (from 10th min to 30th min) and further increase in the deposition rate at the final stage of the drying (from 30th min onwards).

In the case of 3.7 wt% deposition rate decreases more rapidly at the second stage of the drying process compared to the case of the second stage of 3.0 wt%. On the other hand, the deposition rate for 3.0 wt% reaches much higher values at the final stage of the drying.

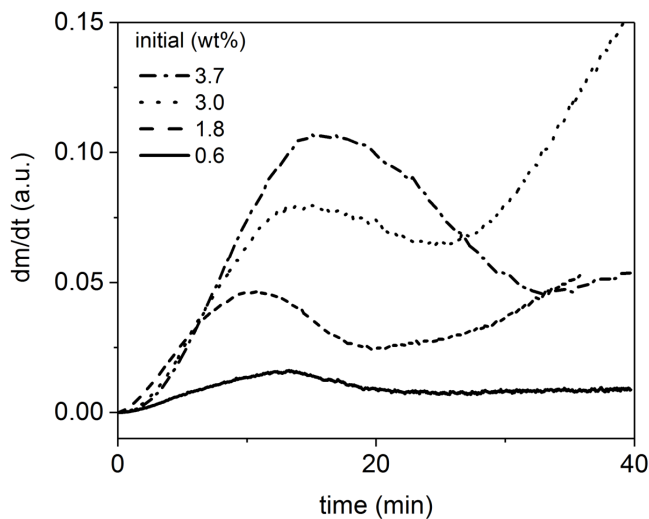


Figure 4-3 Deposition rate of the CNC films

Next, the deposited mass of the films is determined as a function of time (Figure 4-4) by the integration of dm/dt (Equation 4.1). An increase in the deposition rate results in a convex shape in the corresponding curve whereas a decrease in the deposition rate results in a concave shape in deposited mass trends. For example, after 10 min the deposited mass for 3.7 wt% CNCs in Figure 4-4 becomes concave shaped which is due to decrease in the deposition rate whereas deposited mass gets a convex shape after 30 min for initially 3.0 wt% CNCs film. The deposition rate stays constant for the dilute suspensions which leads to a constant mass deposition as seen by the flat deposition profile (Figure 4-2).

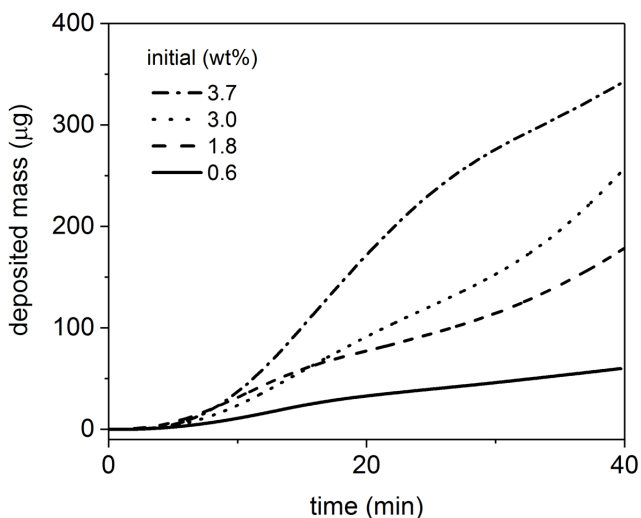


Figure 4-4 Deposited mass of the films in time

Once the deposited mass is determined, it becomes possible to obtain the mass of nanoparticles inside the colloidal drop during drying providing the initial mass of nanoparticles in the system is known. In Figure 4-5, the average concentration of nanoparticles inside the droplet as a function of time during evaporation of the water from the droplet is shown. For suspensions with initial concentration of 1.8, 3.0, and 3.7 wt%, the concentration is found to increase gradually during droplet evaporation. The concentration for drops with an initial concentration of 1.8 wt% and above reaches values where gelation and chiral nematic stacking become possible. As the concentration inside the colloidal drop increases, CNCs accumulate at the liquid-air interface which causes the formation of a skin at this interface. At longer evaporation times, this skin deposits and the colloidal drop becomes richer in water. Consequently, the weight concentration of the suspensions decreases in the final stage of drying.

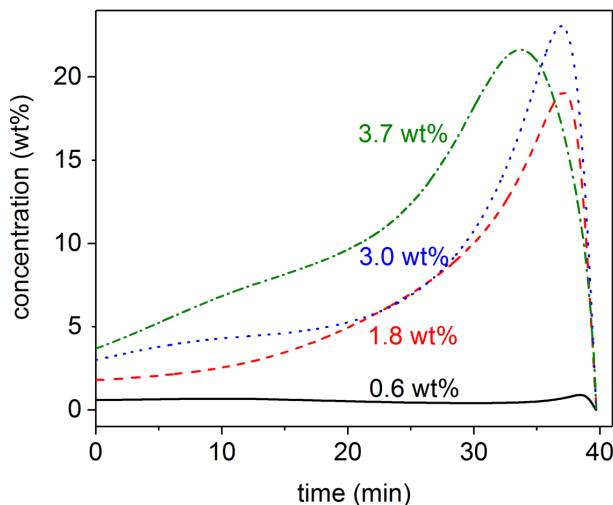


Figure 4-5 Average concentration of nanoparticles in drying colloidal drops

4.2.2. Optical properties of the films

In this section, the optical properties of the films are discussed on the basis of the understanding of the concentration changes during the drying of colloidal films and the deposition patterns of the films developed in the previous section. In a first instance, the self-assembly behavior of CNCs in suspension was analysed under cross-polarized light. Cross-polarized light is used on colloidal suspensions having rod-like particles to visualize phase transitions such as from isotropic to chiral nematic phases.¹⁸⁷ In the case of dilute suspensions rod-shaped particles are isotropic i.e. oriented in a random manner which leads to dark view field under cross-polarized light, whereas at increased concentrations phase transition occur from isotropic phase to chiral nematic phase which results in fingerprint like textures under cross-polarized light.²⁷³ In the same way, the phase transitions are characterized in case of increased concentrations of CNCs suspensions.

In a first instance, the formation of tactoids was observed at initially 3.0 wt% of CNCs as shown in Figure 4-6a. The pitch length of these initial tactoids was around 15 μm

(Figure 4-6a). As some of water evaporated inside the capillary tubes, these tactoids merged into larger assembly domains in a step-growth manner with a pitch length decreasing first to 10 μm (Figure 4-6b) then to 8 μm (Figure 4-6c). The determination of the local concentration is challenging as the nanoparticles are transferred by capillary forces. Longitudinal growth occurs if two tactoids domains meet each other end to end. Some defects can also occur, for instance when tactoid domains with different orientations are merging; an example of which is shown in Figure 4-6c. Long-range order is generally retained over several hundred micrometres (Figure 4-6d). Although the evolution of the pitch length for the suspensions can be recorded with cross-polarized light microscopy up to an optical resolution limit, i.e. 2 μm , for the dried films the pitch lengths cannot be extracted due to further decreases in pitch lengths.

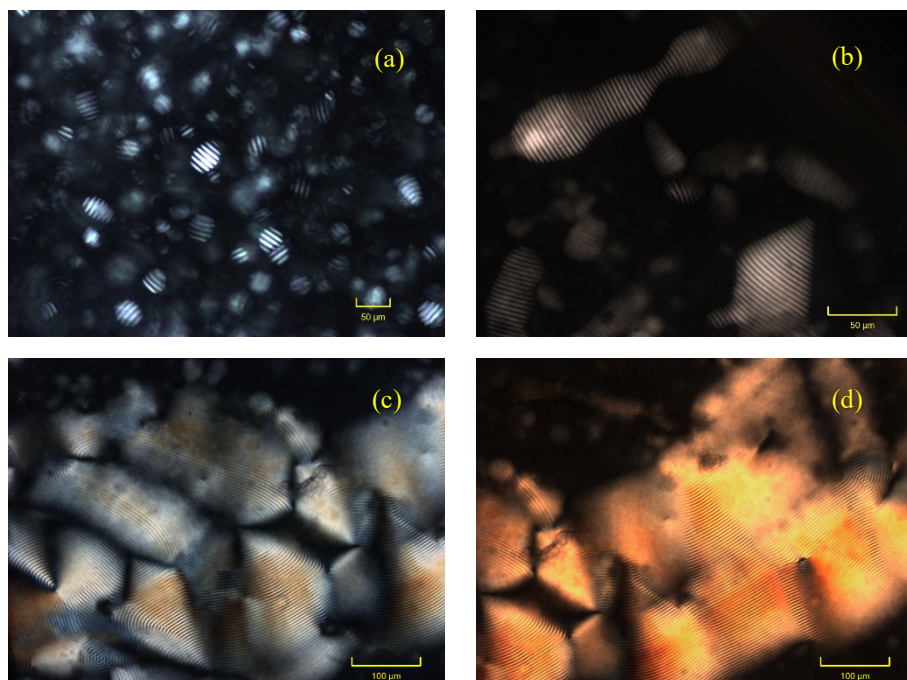


Figure 4-6 Cross-polarized images of (a) Initial formation of tactoids for 3 wt% CNC (b) merging of tactoids (c) local defects (d) long-range order of chiral nematic assemblies.

It is also crucial to understand the degree of orientational order in these assemblies. Capillary tubes are frequently used in studies of characterization of CNCs such as in X-ray scattering, light scattering or helical pitch determination experiments. However, this geometry might cause problems associated with surface induced orientation of the CNCs or induced local concentration gradients due to capillary flow or tube wall effects. It was observed that initially tactoids were randomly oriented (Figure 4-6a). Further evaporation of water inside the capillary tube led to solidified films in which defects caused by parabolic focal conic structures are observed. Similar results were obtained and analysed for dried films of CNCs.²⁷⁴ In a recent study the effects of the shape instabilities and layer undulations on dynamic assembly of chiral nematic domains were investigated.²⁷⁵ There remains a need for an efficient method such as X-ray scattering²⁷⁶ to analyse the orientation of tactoid domains and formed defects. So far, liquid crystalline behavior of CNCs in the suspension has been discussed since the optical properties of obtained films are inherited from those of initial casted suspensions. The discussion will be continued with the analysis of the optical properties of the dried films.

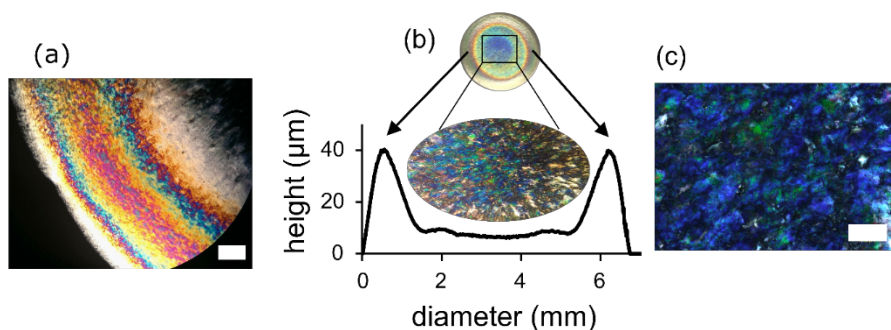


Figure 4-7 CNC film viewed (a) under a cross-polarized light at the edge of the film (scale bar 200 μm), (b) from the top by the naked eye, (c) in the center of the film under a cross-polarized light (scale bar 50 μm) and height profile of the film as a function of diameter

The optical properties of the film obtained via drying of a drop prepared from the deposition of a CNC suspension with an initial concentration of 3.7 wt% were assessed using cross-polarized light microscopy. These films exhibit birefringence just inside the outer border of the film and color changes which are caused by the height differences of the deposit as illustrated by Figure 4-7a. These color changes can be related to the corresponding thickness values by using the Michel-Lévy chart (Appendix A) which consists of the relations of the thickness of the film, optical path difference (retardation), and birefringence (numerical difference between the refractive indices of the CNCs parallel and perpendicular to the optical axis) for polarized light studies.²⁷⁷ The optical path difference (OPD) is the product of the thickness of the sample and birefringence values (Equation 4.4).^{278,279}

$$OPD = |n_{//} - n_{\perp}|t \quad (4.4)$$

where t is the thickness of the specimen, n is the refractive indices. The height obtained from the profilometer yields a thickness at different positions across the diameter of the film as shown in Table 4.1. Multiplication of these values with the birefringence of crystalline cellulose yields an optical path difference that fits the colors observed under the cross-polarized light microscope (Figure 4-8) and the colors displayed in the Michel- Lévy chart (Appendix A). This methodology can be extended to be used for thickness determination of CNC films directly from microscope imaging. For instance, if birefringence values of the samples are known, cross-polarized light microscope images can be used to cross-check with Michel- Lévy chart to determine thickness values at any given position of the films. On the other hand, it was noticed that there is no color formation for unpolarized visible light for the outer region of the film where the thickness gradients exist (Figure 4-7b).

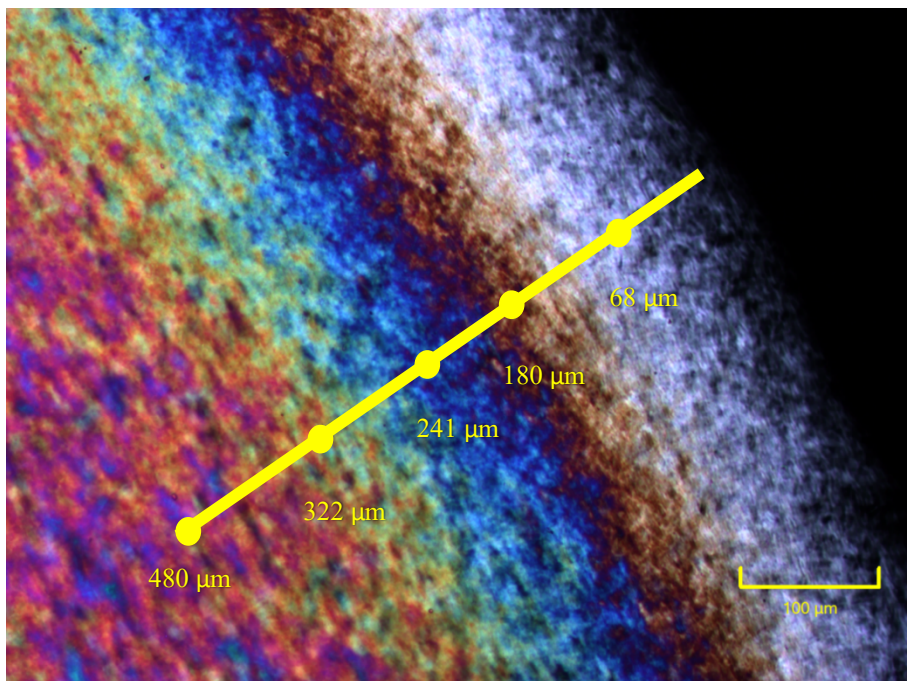


Figure 4-8 Distance from the edge positions which is used in color analysis

Table 4.1 Analysis of OPD from cross-polarized light microscope image of the film in Figure 4-8.

Distance from the edge (μm)	Height of that position (μm)	OPD (nm)
68	6	147
180	18	450
241	24	600
322	31	785
480	40	1000

At the center of the drop-cast films obtained from drying a drop deposited from a suspension of CNCs with an initial concentration of 3.7 wt%, one observes iridescence with the naked eye (under unpolarized light) as a result of the chiral

nematic stacking of the deposited CNCs (Figure 4-7b, c). Fingerprints due to the chiral nematic structuring are readily observed in some domains in the center of the film whereas due to the stacking of the nanocrystals, it is very difficult to differentiate existing fingerprints at the outer edges. The inner area of the film displayed in Figure 4-7 has a uniform average thickness of about 9 micrometer leading to a uniform bluish color that can be explained by Equation 2.4 ($\lambda_{max} = nP\sin\theta$),¹⁸⁹ where n is the refractive index of the film, P is the helical pitch and θ is the incident angle of the light with respect to the surface of the film. λ_{max} can also be decreased by altering the helical pitch with increased particle concentrations as explained in Section 2.6. We can further analyse the color formation observed by the naked eye via correlating the color changes with concentration changes in the colloidal drop prepared from a CNCs suspension with an initial concentration of 3.7 wt% as shown in Figure 4-7b. Formation of red, yellow and green colored rings are attributed to increase in the concentration of the suspension as observed in Figure 4-5 since an increase in the concentration of suspension causes a decrease in the pitch length. At the center of the film, a blue circle is formed where the helical pitch is fixed in a glassy state. However, the pitch length for the blue domains could not be measured due to the optical resolution limit of the microscope.¹⁵ When a film obtained via drying of a suspension of CNCs with an initial concentration of 3.0 wt% was analysed, iridescence was found to be weak at the center of the film which might be due to the scattering of the light caused by the thickness gradients. For 0.6 wt% CNC suspension, there is no iridescence observed in the formed film since the concentration changes of in the colloidal drop stays virtually constant during the drying process and the concentration never reaches values where chiral nematic arrangement occurs.

The optical properties of the films obtained were shown to be dependent on the thickness of these films and the concentration of the colloidal drop. Therefore, it becomes crucial to control either the concentration changes of colloidal drop or the thickness of the films by avoiding the coffee-ring effect to make sure that the colors arise only from uniform film iridescence.

4.2.3. Fluid dynamics

In previous studies numerical simulations were employed to predict the final shape of the deposit obtained from drying colloidal drops.^{59,61,280} Studies related to the evaporation of colloidal films have free-boundary problems in which the shape of the interface is unsteady. In general, analytical solutions can be obtained by the lubrication approximation in which the flow field is predominantly radial, with the largest gradient in radial velocity being the gradient in the axial direction.⁵⁷ Marangoni effects can also be incorporated into these lubrication analyses, however the determination of surface tension gradients requires solving the mass conservation equation for the particles near and at the liquid interface.⁷²

To avoid the complexity of full numerical simulations, dimensionless numbers can be introduced to understand the relative magnitudes of processes controlling the deposition of the particles, and get a practical understanding of how to control the deposition pattern.^{68,222,281,282} In fluid mechanics, these numbers are used to compare the relative magnitudes of forces such as inertial forces, gravitational field, and surface tension which directly affect the fluid behavior.

For instance, Reynolds number, defined by $Re = \rho U l / \eta$, can be introduced via nondimensionalization of the Navier-Stokes equations (Equation 2.2) and used to compare the relative magnitudes of inertial and viscous forces. In the case of the evaporation induced colloidal self-assembly, the relative magnitudes of different contributions can be manipulated to selectively reinforce a specific process to modulate the colloidal deposition pattern. This study follows this approach to understand the internal flow behavior including Marangoni flow inside the drying drop.

To be able to characterize the Marangoni flow via introducing a dimensionless number, a detailed description of the boundary conditions and interfacial stresses for the colloidal drop is needed. A fluid interface consists of two velocity boundary conditions; (1) one for the normal velocity to the interface and (2) one for the tangential velocity. The boundary conditions for the normal and tangential stresses are added for the case of deforming interfaces.

Here, the focus is to analyse of the dynamic boundary conditions for the tangential stresses which can lead to Marangoni flow.

The fluid stress at the surface is defined as, $\sigma \cdot \hat{n}$, and the tangential component of the surface fluid stress as $(\sigma \cdot \hat{n}) \cdot \hat{t}$. The tangential stress caused by surface tension is proportional to the component of the gradient $\nabla\gamma$ which is in the plane of the interface and is expressed as $[\nabla\gamma - \hat{n}(\hat{n} \cdot \nabla\gamma)]$. The component in the interfacial plane is obtained by subtracting the normal component of gradient, $\hat{n}(\hat{n} \cdot \nabla\gamma)$ from the gradient, $\nabla\gamma$. The tangential component of the interfacial tension can be rewritten to derive the dynamic boundary condition:

$$(\sigma_1 \cdot \hat{n}) \cdot \hat{t} - (\sigma_2 \cdot \hat{n}) \cdot \hat{t} = [\nabla\gamma - \hat{n}(\hat{n} \cdot \nabla\gamma)] \cdot \hat{t} \quad (4.5)$$

where σ_1 and σ_2 are the fluid stresses in the domains inside (1) and outside (2) of the liquid-liquid interface. (Appendix B)

For a Newtonian fluid, $\sigma = \eta \left(\frac{\partial u_n}{\partial t} + \frac{\partial u_t}{\partial n} \right)$ the dynamic boundary condition for Marangoni flows is obtained as:^{283,284}

$$\eta_1 \frac{\partial u_{t1}}{\partial n} + \eta_1 \frac{\partial u_{n1}}{\partial t} - \eta_2 \frac{\partial u_{t2}}{\partial n} - \eta_2 \frac{\partial u_{n2}}{\partial t} = -[\nabla\gamma - \hat{n}(\hat{n} \cdot \nabla\gamma)] \quad (4.6)$$

where u_t is the tangential velocity component at the interface and u_n is the normal velocity component. Thus, any surface tension gradient, $\nabla\gamma$, induced by changes in chemical composition or temperature gradient at the interface, generates Marangoni stresses which are balanced by a shear stress in the liquid which drives a recirculating flow called Marangoni flow.

In order to obtain a dimensionless number which characterizes Marangoni flow, Marangoni stress can be compared to the fluid shear stress. The surface tension gradient $\nabla\gamma$ is responsible for Marangoni stress and for a flat surface it can be approximated as $\Delta\gamma/l_c$, where a surface tension difference $\Delta\gamma$ develops over a length scale l_c . The fluid shear stress can be estimated by $\eta U/l_c$ as observed in left-hand side of Equation 4.6.⁵⁸ The characteristic length scale can be defined as the height of the droplet which is determined by the definition of the shear rate.

Thus a generalized Marangoni number can be obtained as shown in Equation 4.7.

$$\text{Marangoni number} = \frac{\Delta\gamma/l_c}{\eta U/l_c} = \frac{\Delta\gamma}{\eta U} \quad (4.7)$$

The Marangoni number (Equation 4.7) was used to determine the relative magnitude of Marangoni flow versus convective transport during the drying of a droplet.^{72,285} For the complex motions at the interface, the velocity scale U can be expressed in terms of the diffusive scaling $U \sim D_p/l_c$ where D_p represents the particle diffusivity. Equation 4.7 can be modified by means of diffusive scaling to define Péclet Marangoni number as given in Equation 4.8.

$$Pe_{Ma} = \frac{\Delta\gamma l_c}{\eta D_p} \quad (4.8)$$

In this chapter, we focus on the understanding of the effect of the particle concentration on the Marangoni flow. Thus, M_a is calculated for the surface tension gradients with changed chemical composition of the interface (Equation 4.9).

$$M_a = - \frac{d\gamma}{dc} \frac{l_c}{\eta D_p} \Delta c \quad (4.9)$$

M_a is based on the change of surface tension (γ) with change of particle concentration (c) and the viscosity of the suspension (η), the length scale of the droplet (l_c), the particle diffusivity (D_p) and the concentration difference (Δc) between the edge and the top of the droplet approximated as the difference between the initial mass concentration and the mass concentration during the evaporation.

In order to calculate the Marangoni number for CNC suspension drops, the surface tension changes of CNC suspensions with different concentrations were determined. The surface tension of the suspensions is shown in Figure 4-9 as determined by pendant drop tensiometry. There is a decrease observed in the surface tension values of the suspensions when the mass concentration of the particles is increased to 3.0 wt%. The decrease in the surface tension of the suspensions is attributed to the accumulation of the nanoparticles at the liquid-vapor interface.

In order to determine the first term of the Marangoni number, which characterizes the magnitude of surface tension forces, the first derivative of the $\gamma(c)$ is determined by fitting an exponential function to the curve plotted in Figure 4-9.

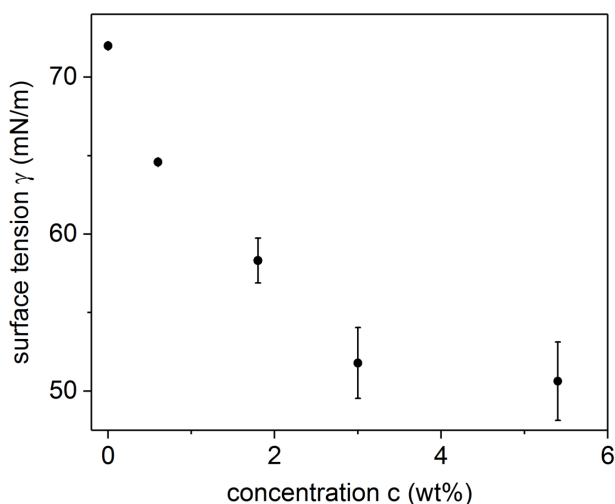


Figure 4-9 Surface tension values of CNC suspensions

After determining the surface tension of the suspensions, rheological tests were carried out to determine the viscosity of the suspensions with different concentrations. Steady shear flow tests show the relation between the shear rate and the viscosity of the suspension (Figure 4-10). It was observed that the viscosity of the suspensions increased with increasing concentration. The viscosities were on the order of a few mPa.s. In dilute concentrations rods are freely rotating and exhibit a Newtonian behavior whereas at increased concentrations the particles start to align which alters the hydrodynamic interactions between the particles. In general, shear thinning is observed for the suspensions with increased mass concentrations (Figure 4-10) which is caused by the orientation of the nanocrystals in suspension by applied shear.²⁸⁶ In addition, tactoids can be formed or destroyed depending on the magnitude of the shear forces. In the literature it is described that coupling the particle alignment to the flow creates shear thinning.²⁸⁷ In this work, the magnitude of the shear thinning in

suspensions are determined by the rate index values. Rate index values (n), are calculated by fitted flow curves to a power law, $\eta = K\dot{\gamma}^{n-1}$ where K is the consistency coefficient, $\dot{\gamma}$ is the shear rate. For a CNC suspension with a concentration of 0.6 wt%, n is calculated to be 0.99 which is unsurprising for a Newtonian behavior. For a 3.0 wt% suspension, n is 0.85 and for a 3.7 wt% suspension n is 0.8 which is more shear thinning.

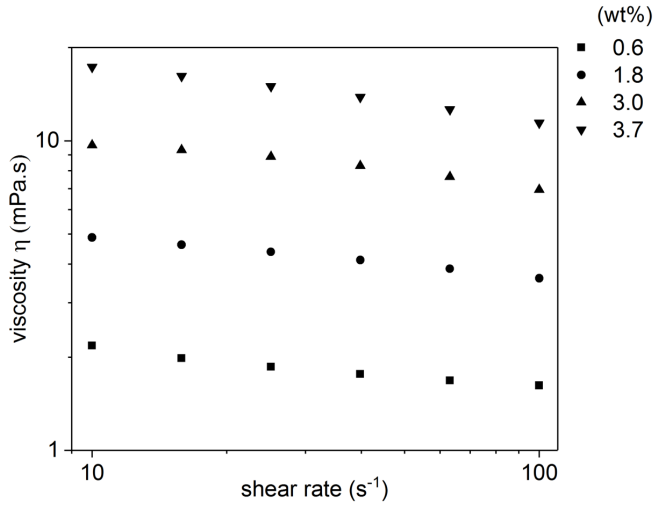


Figure 4-10 Steady shear viscosities of CNC suspensions

For the CNC concentration regime in this study, the magnitude of the parallel diffusion coefficients are approximated to the case of the dilute situation ($D_t \sim 5 \times 10^{-12} \text{ m}^2/\text{s}$).²⁸⁸

After analysing the contributions of the Marangoni number, we set out to calculate the relative Marangoni numbers for the CNC samples to analyse the deposition patterns. Calculated Marangoni numbers (Equation 4.9) are shown in Table 4.2 where a high M_a is seen for low mass concentrations, which would result in a large reverse flow of particles towards the inside of the drying droplet. This is indeed seen for film prepared from a 0.6 wt% suspension, which shows a relatively homogeneous deposit without a clear coffee ring band at the outer edge.

As Ma decreases, the contribution of the capillary flow of particles towards the outer edge becomes more important, and a larger fraction of particles is deposited in the outer ring.

Table 4.2 Relative Marangoni numbers for CNC suspensions

Weight concentration (wt %)	Marangoni numbers
0.6	5.57
1.8	2.22
3.0	1
3.7	0.58

Time-dependent Marangoni numbers were further analysed by considering the concentration changes (Figure 4-5). The viscosity values of different mass concentration of CNC suspension at a shear rate of 10 s^{-1} versus the mass concentration of the suspension were fitted with an exponential function. This function was then used to determine the viscosity values for changed concentrations of the suspensions during drying.

First, Ma numbers were calculated for the initial 10 min of evaporation as illustrated in Figure 4-11a. These numbers are then used to explain the formation of the coffee-ring displayed in Figure 4-2. For the case of 0.6 wt% Ma is governed by surface tension gradients as the viscosity of the system stays constant. After the initial 4 min, the viscous changes have a larger influence on the Ma for 3.0 and 3.7 wt% as the concentration of the system increases. This is also seen as a relatively uniform thickness of the film obtained from a 0.6 wt% suspension as the capillary flow is largely offset by Marangoni flow. For the 1.8 wt% suspension, Ma increases relatively faster for the initial 15 min. The obtained films have a ring deposition for 1.8 wt% as Marangoni flow is not high enough to fully counteract the capillary flow. After 20 min the viscosity changes start to take a larger role in the colloidal drop from a

3.7 wt% suspension, and a decrease in Ma value is observed. Higher Ma numbers due to induced surface tension gradients result in uniform depositions at the center of the droplets obtained from 0.6 and 1.8 wt% suspensions. The detailed analysis of the initially 3.0 wt% CNC of the film deposit is challenging as ring deposition occurs initially which is followed by the hill shaped deposition. Inspection of Figure 4-11a for the initial 10 min shows that Ma numbers are lower for 3.0 wt% CNC than for 0.6 and 1.8 wt% systems which is causing the outer ring deposit. However, after 10 min Ma values start to diverge for 3.0 and 3.7 wt% as illustrated in Figure 4-11b. This more pronounced increase in Ma number for 3.0 wt% is the likely reason to explain the obtained central peak in the film.

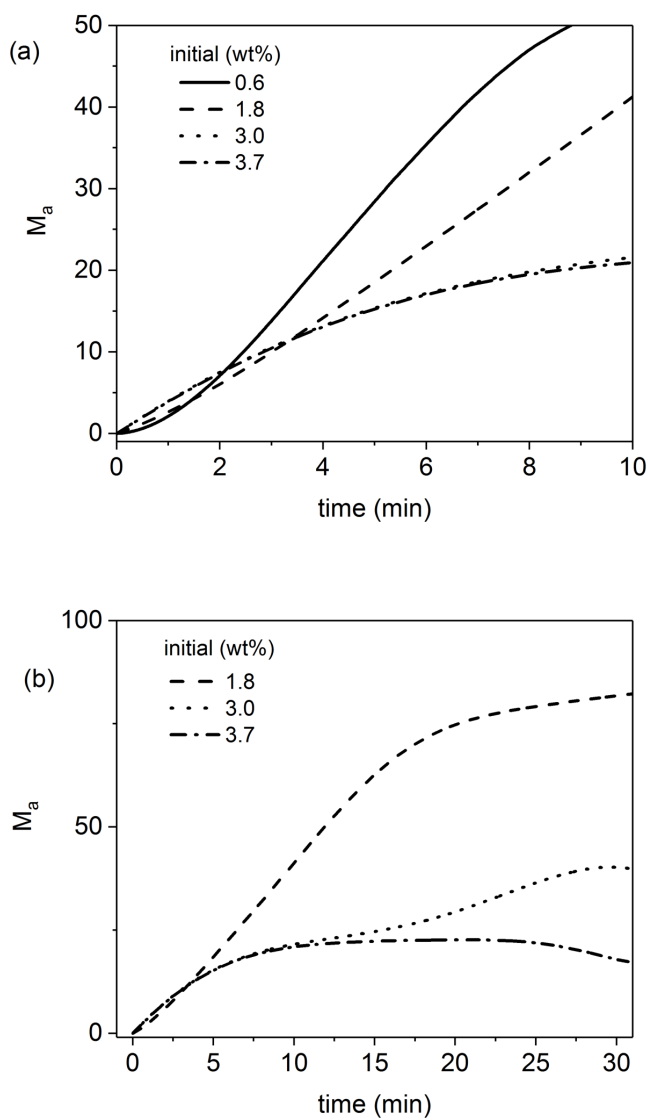


Figure 4-11 Marangoni numbers for (a) initial 10 min (b) for 30 min of drying film

4.3. Conclusions

The colloidal deposition of CNCs in a drying sessile drop is influenced by the coffee-ring effect. Thus, a uniform deposit thickness was not feasible for the produced films. In these systems, a larger fraction of particles is deposited in the outer ring leading to enough deposit height to give Bragg diffraction and colored bands. The determination of the thickness profile of the films and the concentration changes of the drying colloidal drops were effectively used to characterize the optical properties of the films obtained. The analytical approach of determination of concentration changes in drying colloidal drops used in this study can be extended to other applications of colloidal films or to analyse ink formulations for ink-jet printing. Indeed, the efficiency of the inks can be optimized with a better understanding of the concentration changes in drying ink drops and deposited mass.

Dimensionless number analysis reduces the complexity of the numerical solutions to understand fluid flow behavior and colloidal deposition in drying colloidal drops. The coffee-ring effect can be offset by either regulated Marangoni flow counter-acting the capillary flow or resistance to the flow which is induced by viscous or elastic changes in the colloidal suspension.

The content of this chapter was published:

Gençer, A.; Schütz, C.; Thielemans, W., Influence of the Particle Concentration and Marangoni Flow on the Formation of Cellulose Nanocrystal Films. *Langmuir* **2017**, 33 (1), 228-234.

5. Control of the Deposition by Solutal Marangoni Flow

5.1. Introduction

In Chapter 4, the dynamics of the deposition process and important features of the suspensions influencing the colloidal deposition were introduced. It was demonstrated that control over the colloidal deposition can be achieved by selectively manipulating a specific contribution such as fluid flow or the viscosity of the suspensions inside the colloidal drop to obtain the desired deposition pattern. It was identified that, for the case of drying CNC colloidal drops with different concentrations, Marangoni flow was not enough to suppress the coffee-ring effect and thus, to obtain a uniform deposition.

Therefore, we set out to use another way to enhance Marangoni flow relative to capillary flow to control the deposition pattern and thus the optical properties of the films. To this end, solutal Marangoni flow was investigated to offset the capillary flow while retaining colloidal stability of the cellulose nanocrystal dispersions. Solutal Marangoni flow can be achieved by the spatial variation in relative ratios of miscible liquids at the air-liquid interface which can induce surface tension gradients.^{73,77} For instance, the differential evaporation of the solute (liquid with a different surface tension than of solvent) from a solution can induce surface tension gradients.²⁸⁹ In this work, the evaporation-related coffee-ring effect is aimed to be suppressed by creating a surface tension gradient via the diffusion of ethanol vapor into the colloidal drop of CNCs in water, which will create a stronger Marangoni flow dragging particles back to the center of the droplet and thus helping to prevent the accumulation of particles towards the edge. While solutal Marangoni flow is set to induce changes in colloidal deposition, the colloidal stability of CNCs dispersions in ethanol-water mixtures also has to be characterized to ensure the CNCs are not hindered in their structure formation required to obtain the desirable optical properties of the films. For this reason, rheological measurements were carried out for CNCs dispersed in water-

ethanol mixtures. In general, the colloidal stability of CNCs in aqueous suspensions is retained by the electrostatic repulsion among negatively charged sulfate ester groups. Addition of ethanol to the CNC suspension can cause the screening of these electrostatic repulsion between CNCs and thus lead to the aggregation of CNCs. Rheological tests were used to understand the effects of possible aggregation of CNCs on the viscosity behavior of the suspensions. In addition, zeta potential measurements were performed on the CNC suspensions in ethanol-water mixtures to investigate the altered electrostatic interactions which are responsible for the aggregation of CNCs. In the second part of the chapter, dried films of CNCs produced using solutal Marangoni flow were analyzed in terms of deposit shapes and dimensionless group analysis. By understanding the effect of the Marangoni flow, it became possible to exert control over the colloidal deposits by increasing the relative magnitude of Marangoni flow to capillary flow inside the droplet by changing the droplet surface tension. Varying the amount of ethanol in the atmosphere, we were able to find a balance between (1) colloidal stability in the droplet, which is reduced by ethanol diffusion into the droplet, and (2) increasing the Marangoni flow relative to capillary flow inside the droplet by changing the droplet surface tension. Iridescent films with a uniform thickness could therefore be produced.

5.2. Results and Discussion

In this chapter, the solutal Marangoni flow is obtained by diffusion of an ethanol vapor into the colloidal drop consisting of CNCs and water. Ethanol, a relatively benign solvent, is miscible with water and economically available (1.4 \$ per Gallon, Nasdaq, July 2018).²⁹⁰ The surface tension of ethanol-water mixtures changes with respect to the relative ratio of each component.²⁹¹ The viscosity of ethanol is very close to that of water so that rheological characterization of the colloidal stability become easier. Furthermore, it does not require heating for evaporation as is the case for high-boiling solvents.

Solutal Marangoni flow has the advantage over surfactant-induced Marangoni flow that there is no surface contamination due to immiscible chemical species.⁸²

Thermal Marangoni flow would be another alternative, however, it is difficult to localize temperature gradients at a dynamic liquid interface.

The choice of solvent is very crucial as it needs to induce surface tension gradient while retaining the colloidal stability of the suspensions.¹²⁸ Since colloidal stability of CNC suspensions are critical in our work, colloidal stability of cellulose nanocrystals in mixtures of ethanol-water were analyzed before analyzing the flow behavior due to solutal Marangoni flow. A mixed methodology of rheological and zeta potential measurements were applied to the mixtures of CNC in binary ethanol-water mixtures.

5.2.1. Rheological characterization

The effect of the volume fraction of ethanol on the steady shear viscosities CNC suspensions was analyzed to have an understanding of the suspension behavior. The flow curves for a CNC suspension with an initial concentration of 0.6 wt% in water mixed with different volume fractions of ethanol is shown in Figure 5-1. The shear viscosity of the CNC suspensions is increased by the increased volume fraction of ethanol in the suspension at all shear rates.

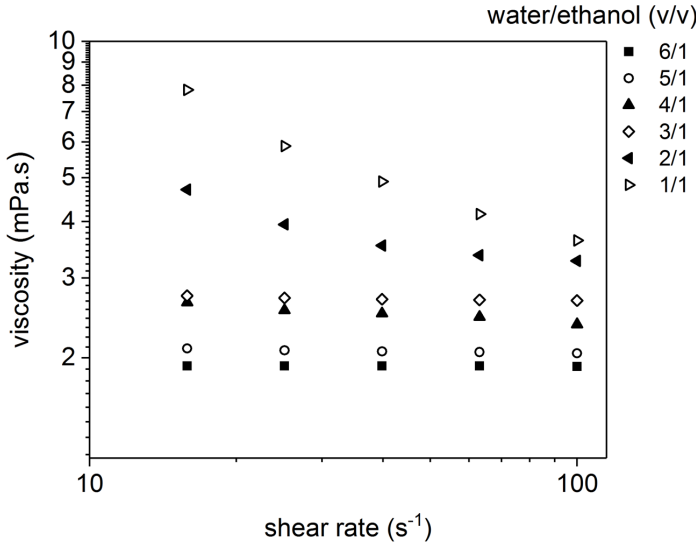


Figure 5-1 Steady shear measurements of initial 0.6 wt% cellulose nanocrystal suspensions in water/ethanol (v/v)

The data can only be recorded up to a minimum shear rate of 15 s^{-1} due to the torque limitation of the instrument. At lower volume fractions of ethanol, the behavior of the mixture is Newtonian as in the case of dilute CNC suspensions in water. This situation is observed up to 25 % v/v ethanol/water with a small increase in viscosity. At 50 % v/v ethanol/water, the overall increase of nearly an order of magnitude of viscosity at 15 s^{-1} with respect to water is attributed to the formation of CNC aggregates. When the ethanol volume fraction was increased to 33 % v/v, shear thinning started at 25 s^{-1} due to the orientation of the aggregated CNC domains or to the breakup of CNC aggregates with increased shear.²²⁸ The degree of shear thinning is highest for the case of 50 % v/v ethanol-water with a calculated rate index of 0.6 as the aggregates formed cause an increase in viscosity at low shear rates and are disrupted as the shear rate is increased to 100 s^{-1} .

After understanding the effect of the addition of ethanol on the behavior of the aqueous CNC suspension for a dilute system, the shear flow tests were repeated for higher weight CNC concentrations (1.8 and 3.0 wt%). For these experiments, problems were encountered during measurements due to the sedimentation of aggregated CNCs. Thus, in order to avoid sedimentation related problems, tests were also carried out using oscillatory measurements.

Oscillatory measurements were performed on CNC suspension with an initial concentration of 3.0 wt% and 3.7 wt% with increased amounts of ethanol. The complex viscosity of the CNC suspensions was observed to increase with an increasing amount of ethanol added to the suspension in water as illustrated in Figure 5-2. This can be due to the aggregation of the particles. One plausible explanation is when ethanol is added to the suspension repulsive forces between particles are screened and attractive forces bring particles into closer proximity and thus increase resistance to flow. At the same time the complex viscosity values seemed to decrease with an increase in frequency which is due to non-Newtonian behavior. Problems due to the instrument inertia were encountered at 100 s^{-1} which caused a plateau behavior in the complex viscosity profile.

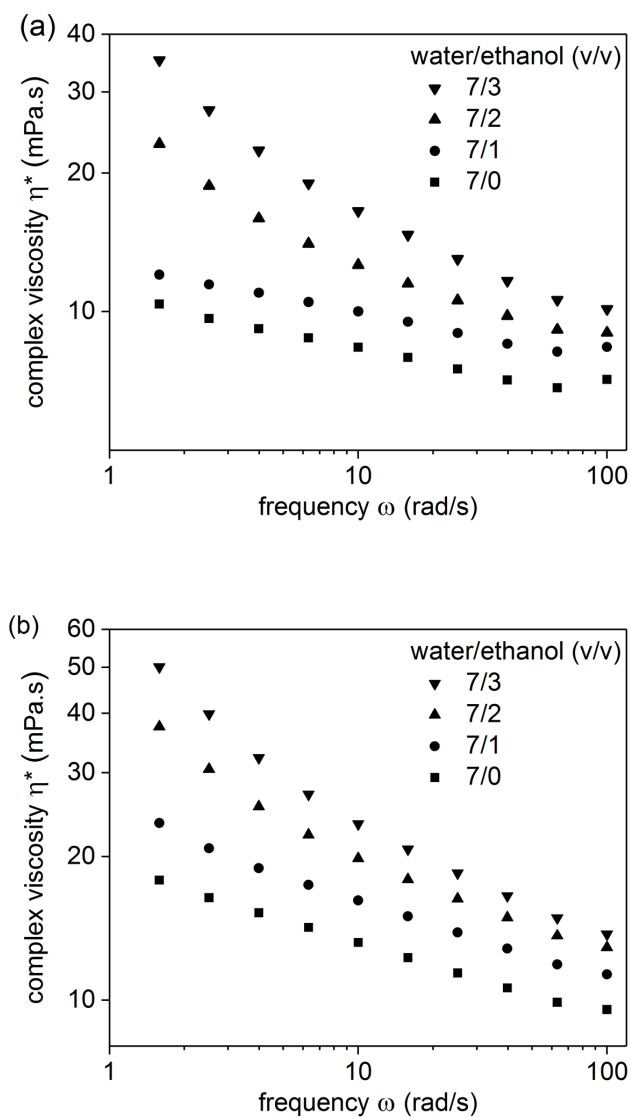
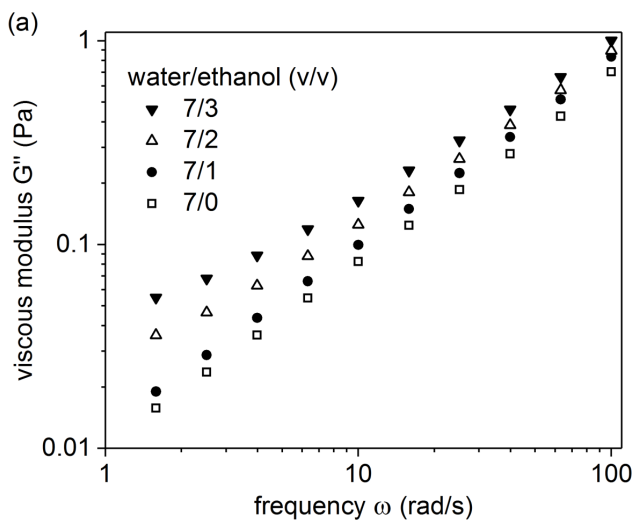


Figure 5-2 Complex viscosity values of initial (a) 3 wt% and (b) 3.7 wt% CNC suspensions in water/ethanol (v/v)

The coupled hydrodynamic effects can cause an increase in the viscous modulus values at higher frequencies (Figure 5-3a). It was described that the solvent mediates the interparticle forces through coupling the motion of colloidal particles which is also known as hydrodynamic interactions.^{292,293} In all cases, the viscous modulus values are observed to dominate the elastic modulus values, an indication of fluid-like behavior of the suspensions. These systems do not exhibit viscoelastic behavior as the contribution of Brownian motion is screened by hydrodynamic interactions. When the hydrodynamic interaction contribution, $\eta_{\infty} \omega$ is subtracted from the viscous modulus data G'' (η_{∞} the limiting high-frequency viscosity), a characteristic viscoelastic behavior with a single relaxation mode due to the Brownian motion of the particles is obtained.²⁹⁴ Relaxation times are seen to decrease with an increased ethanol volume fraction resulting in faster stress relaxation due to the dilution of the systems as indicated in Figure 5-3b.



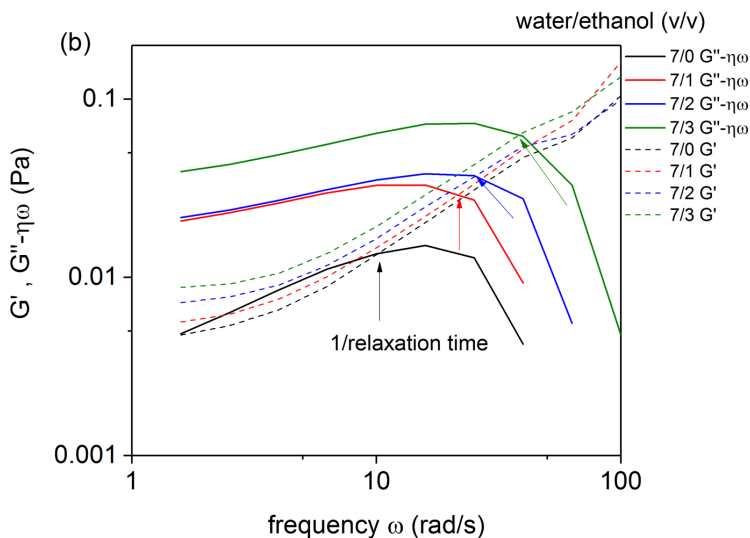


Figure 5-3 (a) Viscous modulus values, (b) Elastic modulus (dash) and corrected viscous modulus (line) of cellulose nanocrystal suspensions with an initial concentration of 3 wt% in water/ethanol (v/v)

Further experiments were carried out to understand the effect of ethanol addition on the electrostatic interactions between the CNCs and thus the colloidal stability of the suspensions. Zeta potential measurements are a good option as a complementary tool to rheological measurements which are calculated based on the electrophoretic mobility of the particles. For a 0.6 wt % cellulose suspension in water the zeta potential increased from -47 mV in pure water to -20 mV (3:1 v/v water/ethanol) and to -12 mV (1:1 v/v water/ethanol) upon the addition of ethanol to the suspension. In an aqueous dispersion, the CNCs are stabilized by the electrostatic repulsion between the negatively charged sulfate ester groups which yield a relatively more negative zeta potential. The addition of ethanol disturbs these repulsions between the CNCs and increases the zeta potential of the dispersion. This is due to fact that ethanol having low dielectric permittivity (ϵ) reduces the solvation of the counterions of the CNCs (H^+ and OH^-) and leads to condensation of the counterions.²⁹⁵

The changes in electrostatic interactions can cause the aggregation of the CNCs which is not desired to obtain a structural formation of CNC films since the agglomeration of CNCs hinders the self-assembly process. Therefore, the ethanol volume fraction in the CNC colloidal drop has to be large enough to induce solutal Marangoni flow yet low enough not to cause aggregation of the particles. So far, the colloidal stability of the CNC particles has been investigated in different volume fractions of ethanol and water using rheological and zeta potential measurements. It was concluded that the direct addition of ethanol into CNC suspension is not a good strategy since it causes problems associated with the aggregation of CNCs. This is why a new approach is needed to induce solutal Marangoni flow for drying CNC colloidal drops.

5.2.2. Solutal Marangoni flow

In a new approach, ethanol was introduced into the colloidal drops via diffusion of ethanol vapor into the CNC colloidal drops. In order to do that, a reservoir of ethanol and water mixtures was used to regulate the vapor concentration of ethanol in a closed environment. Total vapor pressures for an ethanol and water mixture is shown in Figure 5-4 together with predictions from Raoult's law.^{296,297,298} Since the evaporation of the reservoir mixture is assumed to be quasi-steady, the vapor concentration in the atmosphere is assumed to be equal around the colloidal drop and the reservoir, aside from boundary effects close to the interface. Thus, the first assumption is that at equilibrium the bulk vapor boundary conditions at the colloidal drop interface and the liquid interface of the reservoir is the same.

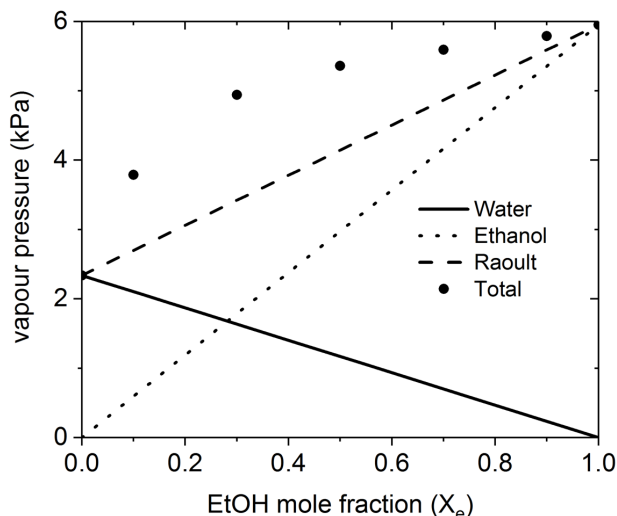


Figure 5-4 Total vapor pressure of an ethanol/water mixture at 20 °C with a mole fraction of ethanol, X_e .

During the drying of the colloidal drop, the scenario becomes more complex in which the diffusion of the ethanol vapor into the drop is followed by preferential evaporation of ethanol from the drop, leading to Marangoni eddies. In the literature, molecular dynamic simulations have been carried out to determine the adsorption and solvation of ethanol at the water liquid-vapor interface.^{299,300} Ethanol is shown to have a positive adsorption at the interface, however, water molecules are arranged to maximize hydrogen bonding between themselves, thereby expelling ethanol molecules. Thus, the density of water is increased in the region of ethanol depletion. These results allowed for the calculation of instantaneous surface tension for ethanol -water mixtures. However the values obtained were overestimating values obtained during macroscopic experimental measurements.²⁹⁹

In order to control the colloidal deposition of CNCs, the discussion will be followed by the fluid flow behavior and the control of the solutal Marangoni flow. Understanding the mechanism of induced surface tension gradients is crucial to generate the desired Marangoni flow. In Section 4.2.3., the effect of the Marangoni

flow on the colloidal deposition with varied concentration of the suspensions was briefly described. For those systems the Marangoni flow was induced by internal contributions in which the dispersed particles regulate the surface tension of the colloidal drops. On the other hand, the solutal Marangoni flow is controlled by dissolved ethanol (solute) via the diffusion of ethanol vapor into the colloidal drop. Thus, the solutal Marangoni flow is induced by external control i.e. the vapor phase. In Chapter 4, the relative Marangoni numbers were determined in order to understand the changes in deposition morphology that were obtained by drying suspensions with different concentrations. For dilute systems (0.6 and 1.8 wt% CNC) the relative Marangoni numbers were determined to be higher than unity which is related to an increased contribution of the Marangoni flow relative to the convection of the CNCs. However, the contribution of the Marangoni flow has to be increased for all concentration regimes to obtain films with a uniform deposition thickness. For this reason, further investigations were carried out on drying films of initially 3.0 wt% and 3.7 wt% CNCs under an ethanol atmosphere since iridescence have been generated at the higher concentrations.

To compare the magnitudes of capillary flow and Marangoni flow, a similar approach of dimensionless group analysis as in previous chapter was followed. The Péclet number for evaporation Pe_E (Equation 5.1) is introduced where, $v_c \approx J_e/l_c^2$ is the evaporation velocity, J_e is the evaporation flux, D_p is the particle diffusivity, and l_c is the length scale of the droplet:

$$Pe_E = \frac{v_c l_c}{D_p} \quad (5.1)$$

This scaling is obtained by the ratio of two characteristic times, τ_d/τ_e namely; characteristic time for diffusion, τ_d which is proportional to l_c^2/D_p and characteristic time for evaporation, τ_e which is proportional to l_c/v_c . Pe_E compares the magnitude of capillary flow via the evaporation velocity to the particle diffusive properties. This number has been used extensively in studies of colloidal film formation to investigate phenomena including skin formation, stratification and vertical drying.^{301,302}

In principle if $Pe_E \gg 1$ evaporation is dominant over diffusion and the system leads to skin formation. In this scenario, the particles cannot be able to diffuse away when the air-liquid interface is descending due to evaporation. Oppositely, if particle diffusion is dominant, i.e. $Pe_E \ll 1$, the colloidal film results in a uniform profile since the diffusion of particles is fast relative to evaporation.

Consider a CNC colloidal drop with a evaporation flux J_e ($4.5 \times 10^{-3} \mu\text{L/s}$) average amount of water evaporated during the drying, length scale of the droplet ($\sim 7 \text{ mm}$) which is initial diameter of the drop, v_c the evaporation velocity ($\sim 9 \times 10^{-2} \mu\text{m/s}$) and D_p diffusion coefficient for CNCs ($5 \mu\text{m}^2/\text{s}$)²⁸⁸, Pe_E is calculated to be 120 which should lead to non-uniform film deposition in the absence of Marangoni flow.

Both numbers, Pe_{Ma} (Equation 4.8) and Pe_E (Equation 5.1), thus describe the ability or inability of particle diffusion to offset the concentration gradients induced by the macroscopic flows, i.e. Marangoni or capillary flow. Dividing these two dimensionless numbers results in another dimensionless number, $Pe_{Ma/E}$ which can be used to compare the magnitude of the Marangoni flow compared to capillary flow in the drying droplets (Equation 5.2):

$$Pe_{Ma/E} = \frac{\Delta\gamma}{\eta v_c} \quad (5.2)$$

where $\Delta\gamma$ is the surface tension difference between a CNC suspension with added ethanol and a neat CNC suspension, η is the viscosity of the suspension and v_c is the evaporation velocity. The surface tension values of ethanol-water mixtures measured at 20°C can be used as an approximation together with those of the CNC suspensions.²⁹¹ Equation 5.2 is a variation of Marangoni number (Equation 4.7) since for $Pe_{Ma/E}$ the velocity scale is characterized by the evaporation velocity.

5.2.3. Film analysis

In the first set of the experiments, the influence of pure ethanol vapor on the colloidal deposition of a CNC suspension with an initial concentration of 3.7 wt% was investigated. The films obtained by drying CNC suspensions (3.7 wt%) under an ethanol vapor gave rise to a film having a white color when viewed with the naked eye. This may indicate that the colloidal stability of the CNCs was negatively affected by the ethanol diffusion into the drying droplet to form the structured patterning needed for iridescence. Cross-polarized light microscope images showed no evidence of color formation in the dried film either as shown in Figure 5-5a. This suggests that long range ordering of the CNCs has to be retained to obtain iridescent films.

At the same time, the deposition of 3.7 wt% under ethanol vapor leads to disk-shaped deposition (Figure 5-5b). This is attributed to induced Marangoni flow which affects the colloidal deposition. For this system, $Pe_{Ma/E}$ is calculated to be 3×10^7 proving that the Marangoni flow is dominant over capillary flow and viscous forces. The amount of ethanol was high enough to induce the necessary surface tension gradient (27 mN/m) and to exert some control over the deposition. On the other hand, the change in vapor phase influences the wetting of the colloidal drop which leads to an increase in contact radius and size of the film. In addition, the ethanol diffusion into the drying droplet creates some problems associated with the aggregation of CNCs. This can also be expected from zeta potential measurements for 3.7 wt % CNCs in water, where the zeta potential increased from -34 mV to -18 mV (3:1 v/v ethanol-water) and -14 mV (1:1 v/v ethanol-water). The flocculation of the CNCs in suspension is also observed with the naked eye upon the addition of an excess of ethanol which creates problems with the zeta potential measurements for higher ethanol volume fractions.

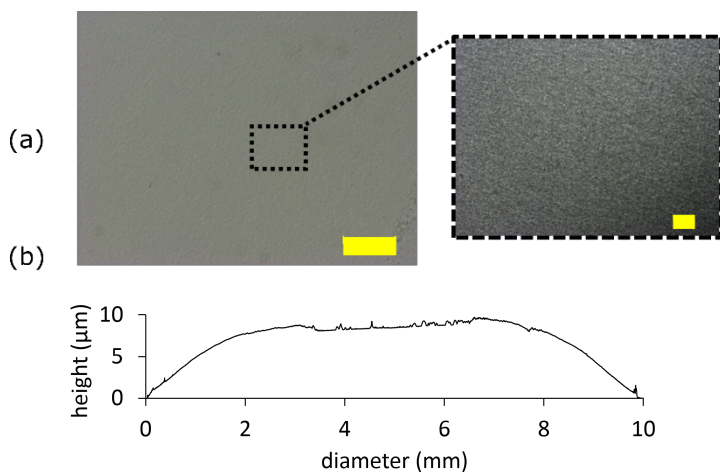
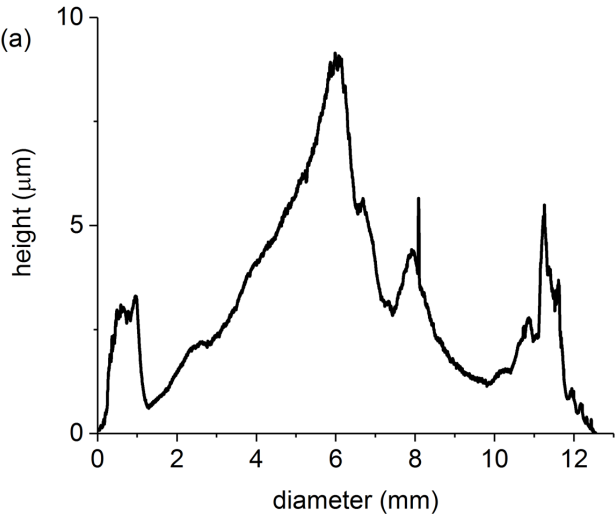


Figure 5-5 (a) Cross-polarized light microscope images of the film obtained via drying 3.7 wt% CNCs suspension under ethanol vapor (scale bars 200 μm and 50 μm) and (b) height profile of the film

Next, the volume ratio of the reservoir was changed to 7:3 v/v ethanol/water ($X_e = 0.4$) for 3.7 wt% CNC to be able to retain the colloidal stability. For this system $Pe_{Ma/E}$ is calculated to be 2.6×10^7 which is enough to induce a control in the deposition, however the colloidal stability of the suspension was still hindered as anticipated from the rheological measurements (Figure 5-2b). In order to decrease the probability of the aggregation, CNC concentration was determined to be reduced. In another set of experiments, CNC concentration was decreased to 3 wt% to avoid the problems associated with the colloidal stability. When a colloidal drop of 3 wt% CNC was dried under ethanol vapor, the flocculation of CNC aggregates caused non-uniform deposition pattern (Figure 5-6a). Although there were signs of flocculation in the film, the deposition pattern suggested an increased Marangoni flow in the drying drop as the central deposition of the film was increased. For this system, $Pe_{Ma/E}$ is 4.7×10^7 which is higher than $Pe_{Ma/E}$ (3×10^7) for 3.7 wt% CNC under ethanol which gives an indication for increased central deposition. To avoid the flocculation of CNCs and alter the magnitude of the Marangoni flow the composition of the vapor phase was varied.

The deposition of the film still exhibited an increased central deposition after drying 3 wt% CNC under ethanol vapor obtained by mixture of 7:3 v/v ethanol/water ($X_e = 0.4$), as shown in Figure 5-6b. For this system, $Pe_{Ma/E}$ is calculated to be 4.2×10^7 with a surface tension difference $\Delta\gamma$, 24 mN/m. Compared to the CNC film without any ethanol, the maximum height of the coffee-ring was reduced one third.



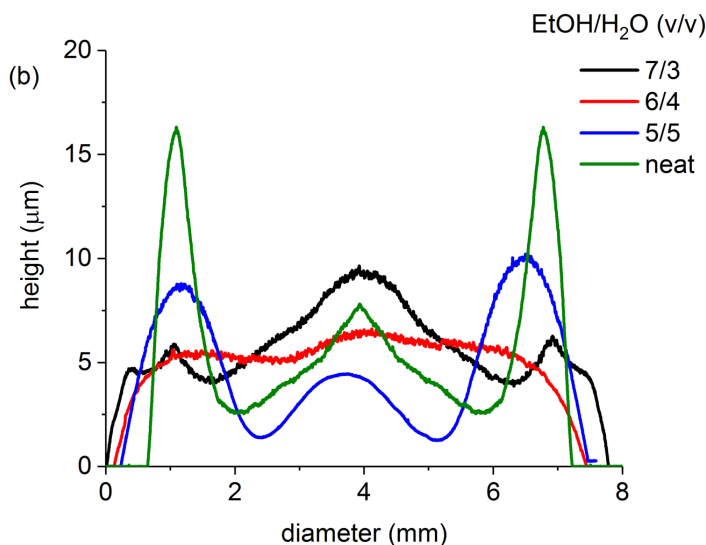


Figure 5-6 Height profile of the films obtained drying 3 wt% CNC under (a) ethanol and (b) different ethanol vapor concentration

The amount of ethanol in the vapor phase was reduced in order to decrease surface tension gradient and thus obtain a more uniform deposition. Thus, a reservoir of 6:4 v/v ethanol/water, ($X_e = 0.3$) was used to induce a solutal Marangoni flow for drying the colloidal drop of 3 wt% CNC. For this system, $Pe_{Ma/E}$ is calculated to be 3.8×10^7 ($\Delta\gamma$, 22 mN/m), i.e. lower than the previous case in which a central peak formed in the film. On the whole, Marangoni flow is adequate to cancel the effect of the capillary flow to produce a film with a more uniform thickness under this atmosphere as shown in Figure 5-6b. Further decrease of ethanol in the vapor phase (a reservoir of 5:5 v/v ethanol/water) causes a loss of uniformity in the obtained films due to reduced surface tension gradients in the system.

The films obtained with a reservoir of 6:4 v/v ethanol/water have a bluish uniform iridescent color throughout the film when viewed by the naked eye which can be seen in Figure 5-7a as a result of a uniform deposition without particle aggregation. The optical properties of the films obtained via this methodology changed considerably compared to that of the films displaying a ring-shaped deposition.

Firstly, the rainbow colors due to thickness gradients at the outer edges are completely absent so that only a blue color is observed under the cross-polarized light as shown in Figure 5-7b, c. The dynamic absorption and the evaporation process of ethanol fine-tune the concentration induced color changes under visible light.

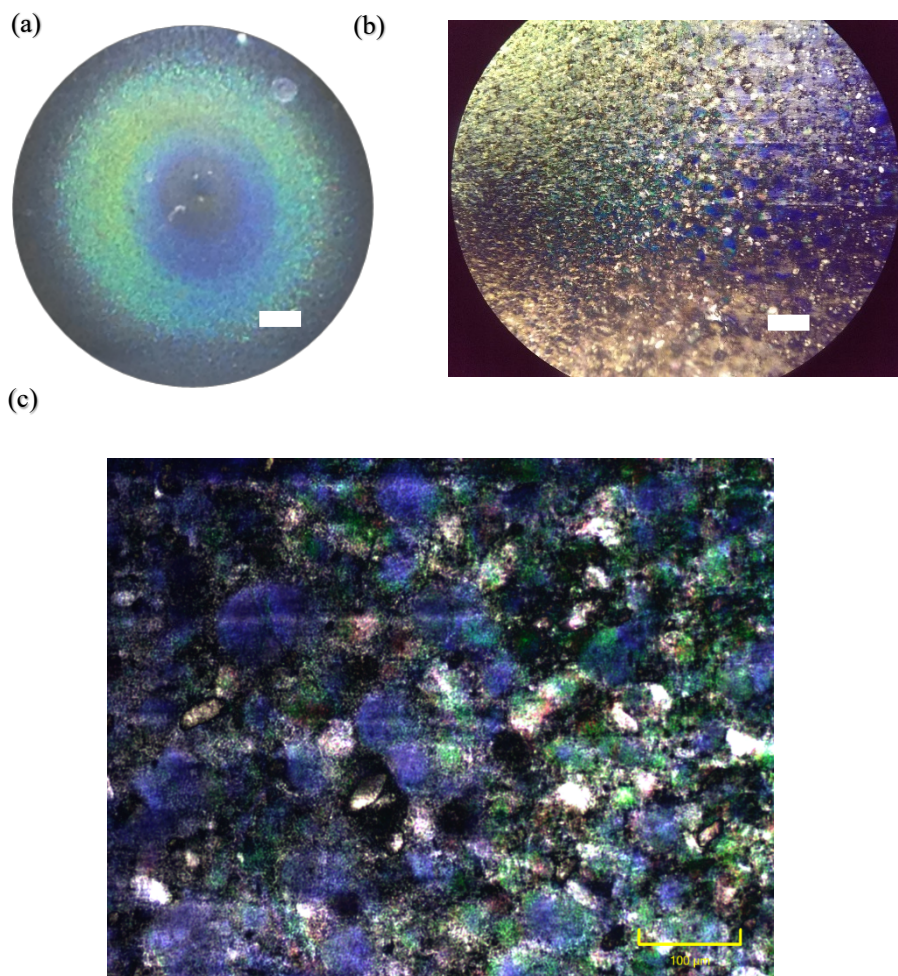


Figure 5-7 (a) Photograph (scale bar 1 mm) and (b, c) Cross-polarized light microscope images of the film obtained by drying a 3 wt% CNC suspension under vapor obtained by a mixture of 6:4 v/v ethanol/water (scale bars 100 μm)

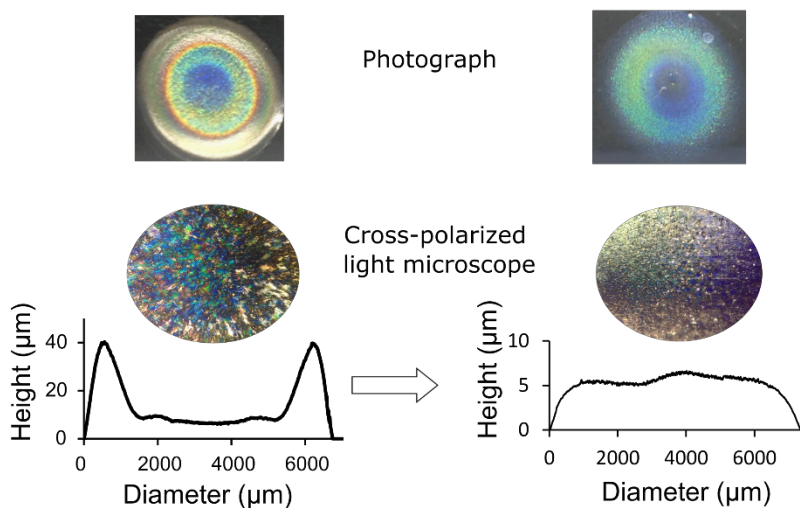


Figure 5-8 Transition of film properties by means of solutal Marangoni flow

In general, the control of the colloidal deposition is a very complex phenomenon which is governed by the fluid flow behavior and thus particle motion inside drying drops. It is realized that if the magnitude of Marangoni flow is increased the coffee-ring effect can be suppressed. The magnitude of the surface tension gradients controls the extent of the Marangoni flow. On the contrary, an increase in the viscosity of the system can reduce the impact of the Marangoni flow. However, it has to be noted that the viscosity of the suspension can also influence the magnitude of the capillary flow by the induced viscous resistance. Dynamic absorption and evaporation of ethanol makes it difficult to analyse the evaporation behavior which is crucial to understand both the magnitude of the capillary flow and Marangoni flow. This methodology can be adapted with other solvent systems where differential evaporation of the solvents induces surface tension gradients. Nevertheless, a special attention has to be given to the combination of the solvents which ensures the colloidal stability of the particles. For the improvement of the study, the hydrodynamic interactions of the particles have to be considered since they are not included in the dimensionless number analysis. By doing so, the deposition of the particles with different shapes can also be understood.

5.3. Conclusions

Iridescent films with a uniform deposition of cellulose nanocrystals were obtained by controlling the relative magnitude of the Marangoni flow (Figure 5-8) opposing convective terms. The forces influencing the deposition process were successfully described using dimensionless number analysis, which enabled the description of the systems studied and to control the deposition profile. The colloidal stability was characterized by rheological and zeta potential measurements to optimize the optical properties of the obtained films through the desired structure formation.

The content of this chapter was published:

Gençer, A.; Van Rie, J.; Lombardo, S.; Kang, K.; Thielemans, W., Effect of Gelation on the Colloidal Deposition of Cellulose Nanocrystal Films.

Biomacromolecules **2018**, 19 (8), 3233-3243.

Author Contributions:

A.G. developed the concept for the study, carried out all the experiments unless otherwise stated, and wrote the manuscript. W.T. supervised and directed the study, and edited the manuscript. K.K. supervised DDLS measurements. A.G. and J.V.R. prepared different batches of CNCs suspensions and mixed these batches. S.L. determined the concentration of sulfate ester group of CNCs.

6. Effect of Gelation on the Deposition of CNC Films

6.1. Introduction

In Chapter 5, a homogeneous deposition of cellulose nanocrystal films was achieved from a drying colloidal drop by reinforcing Marangoni flow over the internal capillary flow. This was attained by exposing the colloidal drop to ethanol vapor which induces solutal Marangoni flow during drying. The uniform films showed iridescence when ethanol absorption was limited to retain colloidal stability and self-assembly of the particles. In general, the addition of organic solvents to aqueous CNC suspensions alters the electrostatic interactions between the particles which can lead to aggregation of the particles. This causes limitations for the application of solvent-mediated Marangoni flow in studies of evaporation induced self-assembly.

An alternative way of controlling the colloidal deposition is introduced for CNC films in this chapter. In this new approach we aimed to reduce the coffee ring effect by inducing elastic resistance in the colloidal drop via gelation. The capillary flow inside the drying drop, responsible for non-uniform deposition, is thus restricted by the viscoelastic changes in the colloidal drop. These changes consequently affect the final morphology of the dried films. To test this hypothesis, CNC films were prepared by drop casting CNC suspensions containing NaCl and CaCl₂ salts which are known to facilitate gel formation.^{175,178} The effect of gelation on the deposition pattern and on the self-assembly of CNCs during the droplet drying is discussed. A mixed methodology using rheological and depolarized dynamic light scattering was applied to understand the deposition behavior of the CNCs. In addition, the analysis of the surface tension, viscosity and yield stress of the suspension mixture was used to gain deeper insights into the deposition process. The understanding of the gelation behavior in the drying droplet was used to exert control over the deposit where the coffee-ring deposit can be converted to a dome-shaped deposit. Lastly, the effects on the optical properties of the films were characterized with cross-polarized light microscopy and linked to the deposition parameters.

6.2. Results and Discussion

Gel formation in a colloidal drop can be an effective way to restrict the radial capillary flow that is responsible for the coffee-ring effect. Thus, the particles motion towards the drop edge can be suppressed via induction of gelation. For instance, Talbot and co-workers used the sol-gel transition during evaporation to regulate the colloidal deposition of polystyrene particles.³⁰³ Other examples include the addition of polymers to microsphere dispersions prior to drop casting to increase the viscosity of the system and thus to avoid the coffee-ring effect.^{304,305} In order to adapt these strategies to CNC films, an additive is required to induce gelation in colloidal drops. In the work presented here NaCl and CaCl₂, which have different type of cations and cationic charges, were chosen to induce gelation. It has been discussed that network formation and gelation of CNC suspensions is caused by different mechanisms namely charge screening for monovalent salts such as NaCl and cationic bridging for divalent salts such as CaCl₂.^{173,175,180} The differences in network formation due to the addition of salts changes the rheological properties of the suspensions for different concentrations of the salt. Increasing the charge and ionic radius of the cations have also been shown to increase the elastic moduli of the gels,^{178,306} which was attributed to the fact that the mesh size of the network was changed relative to the ions added to the system.

Both CNC and salt (NaCl or CaCl₂) concentrations can be varied to achieve the desired magnitude of the elastic modulus. As the deposition of CNC particles is set to be controlled by inducing gelation, there remains a need to understand the effect of the induced elastic resistance on the capillary flow. Again, it is possible to apply dimensional analysis to compare the effect of contributing factors on the fluid flow and weigh out the relative magnitude of the different contributions. As gelation is a different process, another dimensionless number is needed to characterize the contribution of the elastic modulus due to gelation of the suspensions: The modified capillary number, \mathcal{C} (Equation 6.1), enables one to compare the elastic modulus with the internal capillary pressure to quantify the elastic modulus at which the capillary flow is completely stopped.³⁰³

$$\epsilon = \frac{G' r_c}{2\gamma} \quad (6.1)$$

ϵ is based on the ratio of the elastic modulus, G' , to the Laplace pressure ($P = 2\gamma/r_c$) inside the droplet, where r_c is the radius of curvature of the droplet and γ is the surface tension. The value for ϵ has to be higher than unity for network (gel) integrity, expressed by the modulus, to resist the Laplace pressure inside the drying droplet. To determine whether gelation as a result of salt addition is sufficient to stop/limit the capillary flow, in a drying droplet, one needs to establish the magnitude of the gel yield stress at which the capillary flow is inhibited. Setting $\epsilon=1$, it becomes possible to estimate the elastic modulus at which capillary flow is inhibited for a droplet with known surface tension and a radius of curvature. For the systems under investigation here (droplet radius 2.5×10^{-3} m), values are reported in Table 6.1.

Table 6.1 Elastic modulus values required to attain $\epsilon = 1$ and surface tension values for CNC suspensions with added salt (10 mM)

CNCs	NaCl	CaCl ₂	NaCl	CaCl ₂
	G'	G'	γ	γ
(wt %)	(Pa)	(Pa)	(mN/m)	(mN/m)
2	50.08	52.87	62.6± 2.3	66.0± 1.7
4	37.44	30.83	46.8± 1.9	38.5± 2.9

The decrease in the calculated moduli with increased CNC concentration is due to reduced values of surface tension of the mixtures (Table 6.1). Previous work has noted that the actual yield stress required to overcome capillary flow is lower than this calculated G' as there is a gradient in capillary pressure within the drying droplet.³⁰³ The determined G' values using this method can thus be considered to be an upper limit.

The experimentally determined yield stress values, σ_y (Table 6.2) were compared to the gel modulus at $\epsilon = 1$ (Table 6.1). It can readily be seen that in all of the cases for CNC suspensions containing NaCl, the magnitude of the yield stress under

equilibrium conditions should not be sufficient to resist the capillary pressure, and thus these systems are not expected to fully inhibit capillary flow. The CNC suspensions containing CaCl₂ display a higher yield strength compared to the ones containing NaCl under equilibrium conditions.

Table 6.2 Yield stress values for CNC suspensions with added salt (10 mM)

CNCs (wt %)	NaCl σ_y (Pa)	NaCl σ_y (Pa)	NaCl σ_y (Pa)	CaCl ₂ σ_y (Pa)	CaCl ₂ σ_y (Pa)
	Initial	After 30 min	After 1 hr	Initial	After 30 min
2	-	0.31	0.64	1.02	23.38
4	0.20	1.52	10.32	9.49	119.84
10	8.52	22.89	-	74.18	-

On the other hand, dynamic changes of yield stress values have to be taken into account since the evaporation of water from the colloidal drop causes changes in the concentration of CNCs. For this reason, the concentration changes in the evaporating droplets was determined in the drying droplets as described in Section 4.2.1. The calculations gave an understanding of average weight concentration changes in the drop (Figure 6-1).

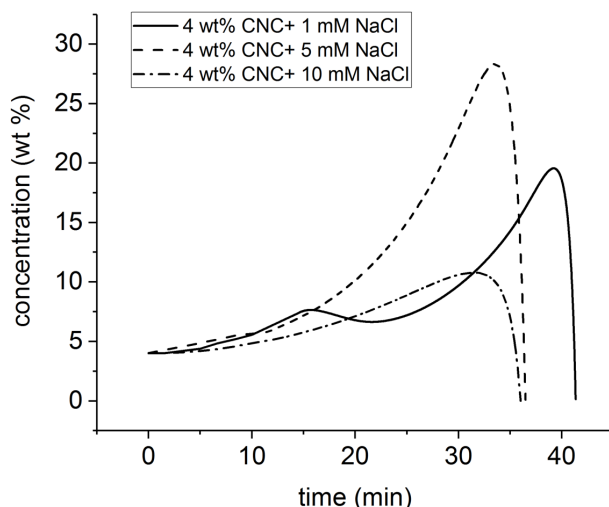


Figure 6-1 Average weight concentration variation of cellulose nanocrystals in the drying droplets with added NaCl

During drying of a droplet with initially 4 wt% CNC+ 1 mM NaCl, we observed a peak in the weight concentration change at 15 min due to depinning, in which some of the formed skin collapses. However, it was observed that the average concentrations in the drying droplets reached much higher values for suspensions containing 1 and 5 mM NaCl, while the increase in concentration was suppressed when 10 mM NaCl was added to the suspension. This suppression for 10 mM NaCl is either due to gelation or to the deposition of the skin during drying.

Unfortunately, local concentration gradients cannot be determined since spatial information on the particles within the droplet is missing. If one would like to estimate local concentrations, other methods such as computational fluid dynamics should be used but the accuracy will also heavily depend on the simulation assumptions.³⁰⁷ For this dimensional analysis (Equation 6.1), average concentrations are sufficient to gain the required insights into the order of magnitudes of the opposing forces. One can thus refer to bulk concentration changes in the colloidal drops and analyze the yield stress values for a specific concentration regime. For instance, when the weight

concentration of CNCs increases to 10 wt% for drying colloidal drops at longer times with initially 4wt% CNCs + 10 mM NaCl (Figure 6-1), the recorded yield stress value (8.52 Pa) is still lower than the required gel modulus to stop capillary flow (Table 6.2). On the other hand, it becomes impossible to determine the yield stress values for systems with added salt where the weight concentration of CNCs exceeds 10 wt% since homogenous mixing of the salt and gelled CNCs cannot be achieved due to aggregation. For the studied concentrations of CNC suspensions, the determined yield stress values when CaCl_2 is added to the suspensions reached sufficiently high values to stop capillary flow. Yield stress values for CaCl_2 after an hour cannot be recorded due to inhomogeneous flow which is caused by the formation of aggregates of CNCs. To detect the transition from viscous to gel state, dynamic oscillatory tests were performed for different concentrations of salts added to the CNC suspensions. For 4 wt% CNC + 5 mM NaCl suspension, the viscous modulus values dominate the elastic modulus as shown in Figure 6-2 which is an indication of viscous fluid-like behavior. The elastic modulus was observed to dominate the viscous modulus when the concentration was increased to 10 mM for 4 wt% CNC which is a proof of gel formation. In addition, for gel-like systems the elastic modulus values display a frequency-independent behavior.

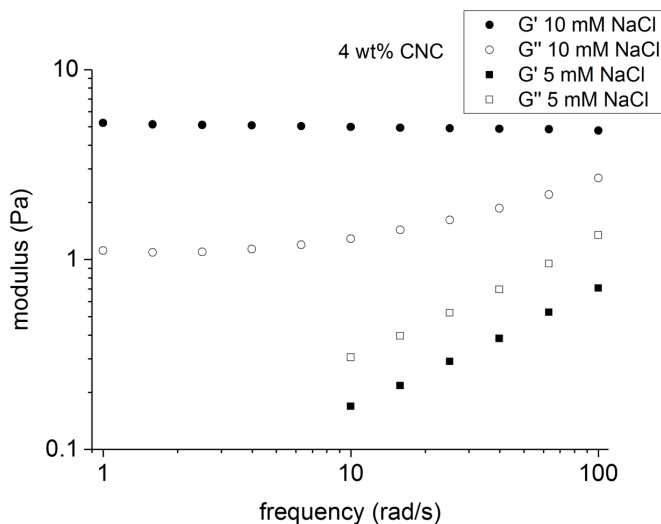


Figure 6-2 Dynamic oscillatory measurements of 4 wt% CNC suspension with added salt

Next, the effect of the different salts on the viscoelastic behavior of the CNC suspensions were analyzed. Dynamic oscillatory measurements were carried out with 2 wt% and 4 wt% CNC suspensions with a salt concentration of 10 mM and modulus values were compared to understand the magnitude of the network formation and the gel strength (Figure 6-3). Both elastic and viscous modulus values were found to increase with increasing the CNCs concentration from 2 wt% to 4 wt%. The elastic modulus values were higher for CNC suspensions containing CaCl_2 when compare to suspensions containing NaCl as illustrated in Figure 6-3. This was attributed to the different mechanisms of network formation. The same behavior was observed in steady shear tests: for the same concentration of salts, the viscosity of the suspension was recorded to be higher for the CaCl_2 systems (Figure 6-4). Thus, gelation starts at lower concentrations for CaCl_2 than for NaCl. At the same concentration regime, CaCl_2 added suspensions exhibit stronger gel behavior than NaCl added suspensions. In all cases, the suspensions with added CaCl_2 showed a higher modulus values, which was ascribed to increased percolation.

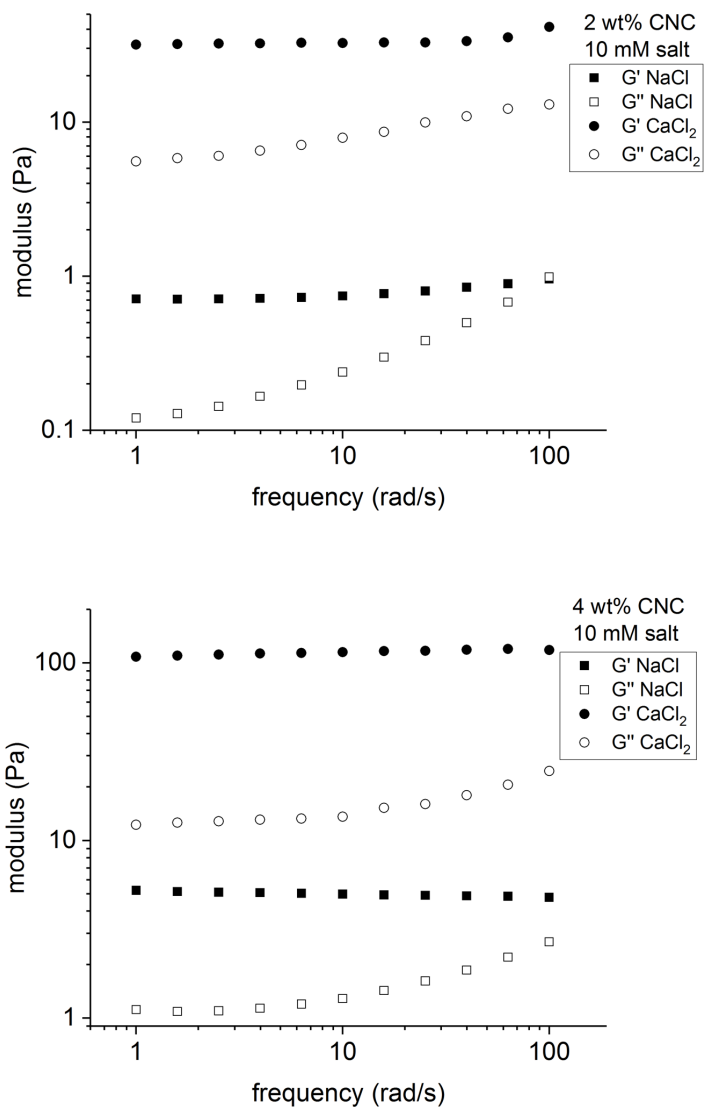


Figure 6-3 Dynamic oscillatory measurements of CNC suspensions with different salt

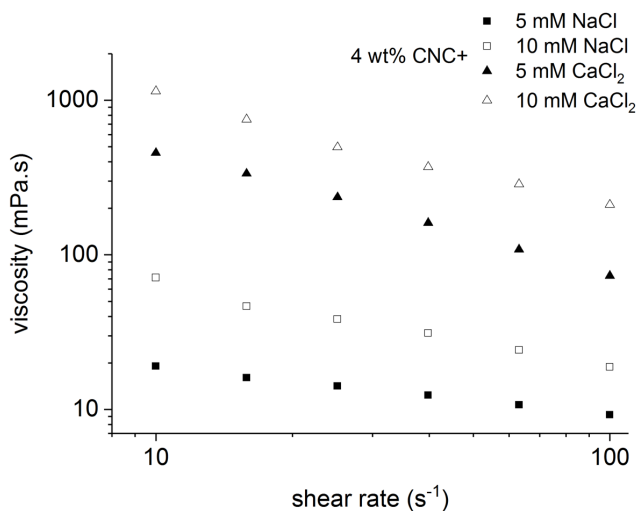


Figure 6-4 Steady shear viscosity values of salt added CNC suspension at initial time of mixing

The addition of salt to the suspensions also caused changes in the zeta potential of the systems, as shown in Figure 6-5. The zeta potential of salt containing suspensions increased as the concentration of the salt was increased to 5 mM. This information can be useful to predict the colloidal stability of the CNCs, since the systems with zeta potential below -25 and above 25 mV are stable whereas the systems with zeta potential closer to 0 mV are unstable.²⁶⁹

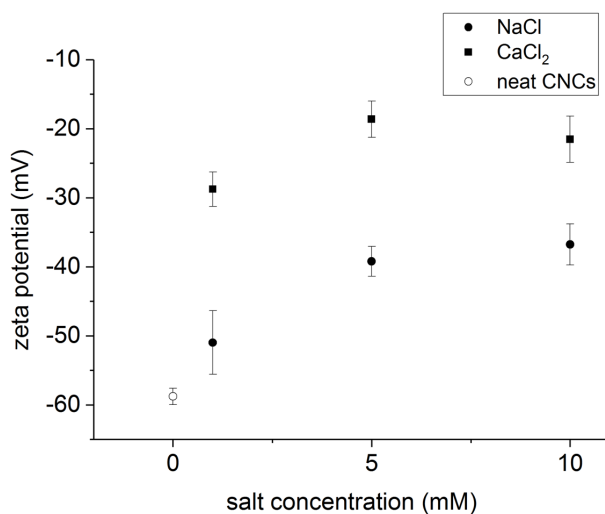


Figure 6-5 Zeta potential values for CNC suspensions (0.55 wt%) as function of the concentration and type of salt in the suspension

So far, the changes in rheological properties of the suspensions were described with respect to the concentration of CNC and added salt. Understanding the gelation kinetics is also important during the time-dependent drying of the colloidal suspensions. It was already reported that NaCl addition to CNC suspensions leads to a network formation of particles that grows with time.¹⁷⁴ The addition of salt is known to cause a change in the rheological behavior of CNC suspensions in time.²⁵⁹ For this reason, it is important to determine the rheological behavior of CNC suspensions as a function of time upon salt addition. The evolution of the rheological properties was investigated using two different approaches: In the first approach, steady shear viscosities were measured after a certain period of time and changes in the viscosity were tracked. As seen in Figure 6-6 half an hour after the initial mixing, the viscosity is observed to increase at any given shear rate. At the same time, shear thinning behavior was observed for salt added suspensions. The magnitude of the shear thinning in suspensions are determined by the rate index values (n) as described in Section 4.2.3. For a CNC suspension with 5 mM NaCl, rate index is reduced from 0.69 to 0.51 after half an hour of mixing whereas with 10 mM NaCl, rate index is

reduced from 0.46 to 0.22. The decreased rate index values were attributed to shear-induced breakup of CNCs networks. In the second approach, time sweep experiments were carried out to be able characterize changes in the modulus of the suspensions in time. The obtained results for different wt% CNC suspensions with different salts are shown in Figure 6-7. An increase in the elastic modulus as a function of time is observed, proving the continuation of the network formation and quantifying its strength. These samples exhibited gel-like behavior since the elastic modulus is dominating the viscous modulus during the time scale of the measurement. It was reported that divalent cations induce attractive forces between two rigid polyelectrolyte rods.³⁰⁸ This effect increases CNCs aggregation in the presence of Ca^{2+} cations which is responsible for the increased elastic modulus for CaCl_2 added CNC suspensions compared to NaCl added CNC suspensions.

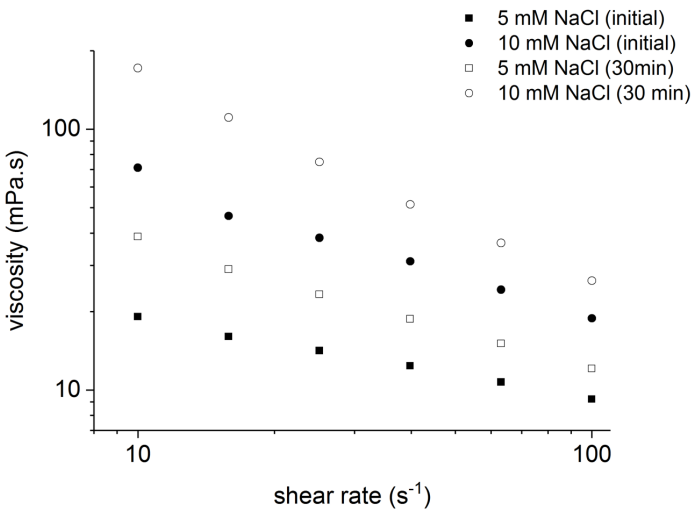


Figure 6-6 Time evolution of viscosity values for 4 wt% CNC suspension with added salt

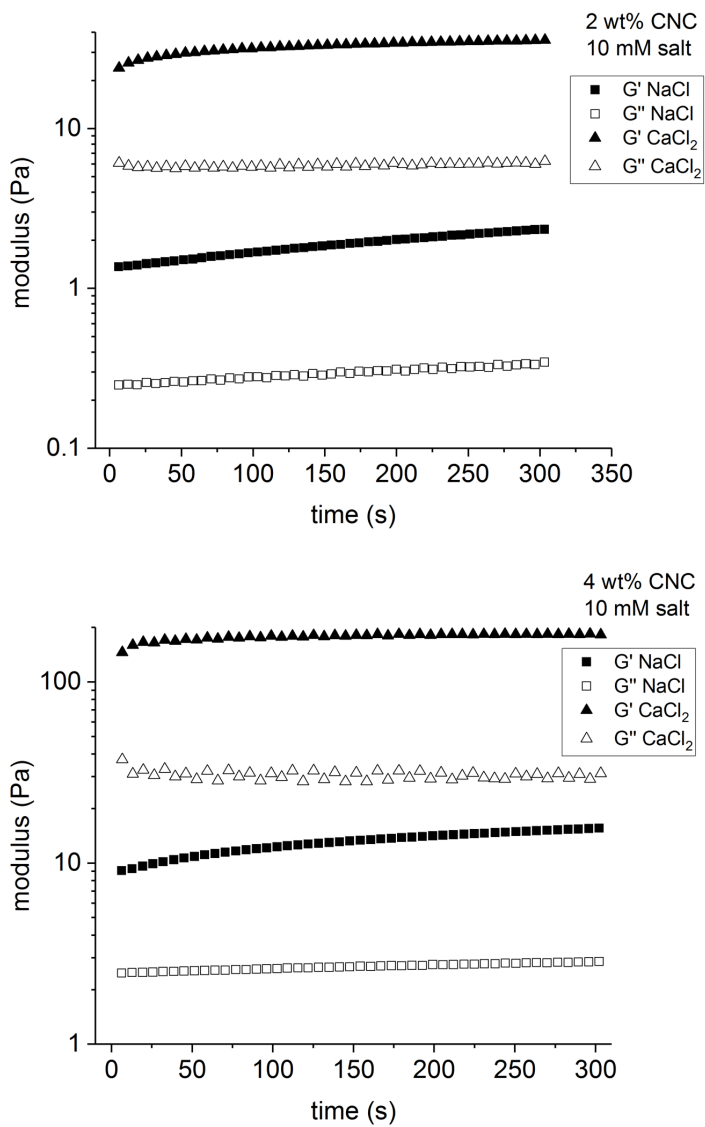


Figure 6-7 Time sweep measurements of 2 and 4 wt% CNC mixed with 10 mM salt

Understanding the rheological properties of salt containing CNC suspensions is an important step to characterize the deposition process of the CNCs. Yet, particle motion is also influenced by the fluid flow which is subject to change with induced surface tension gradients. For this reason, the contribution of the Marangoni flow on the colloidal deposition was further analysed.

6.2.1. Marangoni flow for salt containing CNC suspensions

The modified capillary number (Equation 6.1) gives one a means to describe the effect of the elastic resistance opposing the capillary flow but does not take into account the effect of Marangoni stresses. The surface tension gradients induced by gelation create a Marangoni stress at the interface which is balanced by a shear stress within the liquid. In this work, the Marangoni stresses are induced by gradients of surface tension in the gelled suspension due to the addition of salt into the CNC suspension. In a similar way, the surface tension of ethyl cellulose nanoparticle suspensions has previously been shown to decrease upon the addition of salt.³⁰⁹ This mechanism was explained in two different ways; in the first scenario, the nanoparticle aggregates formed in the bulk are adsorbed at the air–water interface alongside the single nanoparticles whereas in the second scenario only a single nanoparticle is initially adsorbed at the air–water interface while the nanoparticle aggregates are formed at the interface through attachment of nanoparticles onto those already at the interface. As the adsorption is a dynamic process there will inherently be concentration gradients on the surface giving rise to local Marangoni stresses. One can analyze the effect of surface tension gradients and the viscosity of the suspensions on the deposition using the Marangoni number, M_a , using the same dimensionless number approach as used in Section 4.2.3.

The Marangoni number ($M_a = -\frac{d\gamma}{dc} \frac{l_c}{\eta D_{par}} \Delta c$) was calculated for the CNC suspensions with different salt concentrations where $(d\gamma/dc)$ is the surface tension change with the change of the salt concentration, l_c is the length scale of the droplet (diameter of the droplet), η is the viscosity of the suspensions, and D_{par} is the parallel particle diffusivity. The product of $-\left(\frac{d\gamma}{dc}\right) \Delta c$ is the magnitude of the surface tension

difference across the droplet determined by the difference between the surface tension of the suspension containing salt and the neat CNC suspension. In order to calculate the Marangoni number, the surface tension of the salt mixed suspensions was determined using pendant drop tensiometry in the same way the surface tension of the neat CNC suspensions was determined (Figure 4-9). The obtained results (Figure 6-8) showed that the surface tension of the CNC suspensions decreased with increased concentration of the salt. This is attributed to network formation of particles at the air-liquid interface which is disturbing hydrogen bonding between water molecules.³⁰⁹ The decrease in the surface tension in the case of increased CaCl_2 concentration is more pronounced since Ca^{2+} can form ionic bridges with CNCs.^{175,308} Average surface tension values are used together with the surface tension of the neat CNC suspension to determine the local surface tension changes in the dimensionless number analysis.

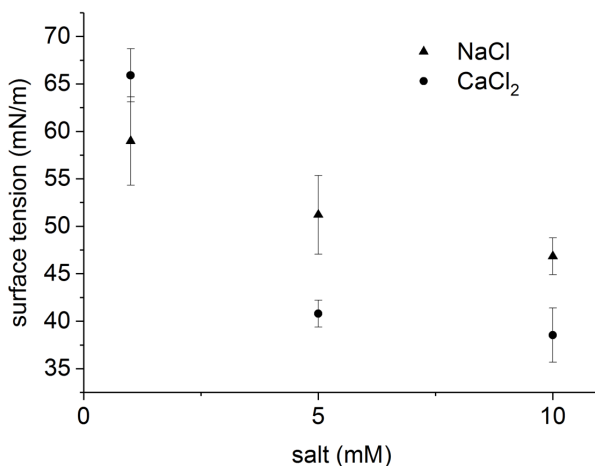


Figure 6-8 Surface tension measurements of 4 wt% CNC mixed with salt

To determine the diffusional properties of CNCs in the salt solutions depolarized dynamic light scattering (DDLS) was used. This enabled us to extract the diffusion coefficients of the CNCs in the mixed systems. Furthermore, DDLS makes it possible to extract the translational and rotational diffusion coefficients.

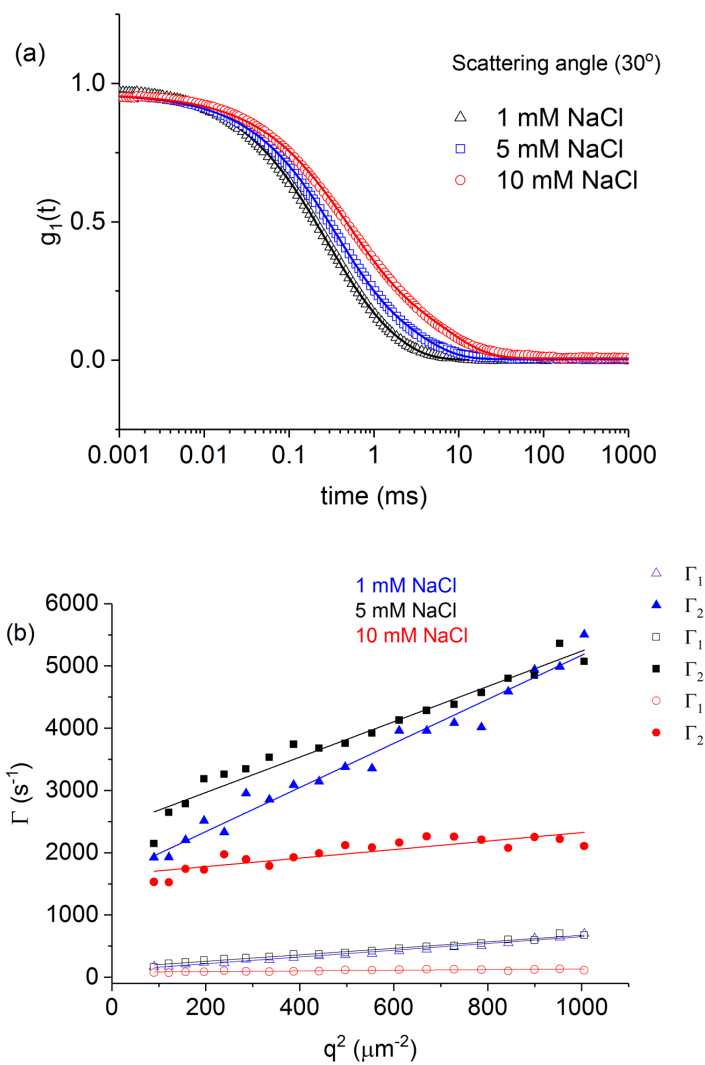


Figure 6-9 (a) Autocorrelation curves measured at scattering angle of 30° for 4 wt% CNC mixed with salt (b) fitted decay constants to extract the diffusion coefficients

The DDLS autocorrelation functions (I_{VH} geometry) at a scattering angle of 30° for CNC suspensions mixed with different concentrations of salt are shown in Figure 6-9a. The relaxation times increased with increased salt concentrations which leads to the shift towards longer times in the autocorrelation curves. Rod shaped particles undergo slow and fast diffusional translational motions perpendicular and parallel to the particle main axis. Parallel diffusion coefficients were obtained via the slope of the linear fit to Γ (decay constant) vs. q^2 in fast mode whereas the perpendicular diffusion coefficients were obtained by the slope of the linear fit to Γ (decay constant) vs. q^2 in slow mode (Figure 6-9b).

The diffusion coefficients are shown in Table 6.3 together with the calculated Marangoni numbers for a 4 wt% CNC suspension as a function of the amount of NaCl. The calculated Marangoni numbers can then be used to understand the relative magnitude of the Marangoni flow with respect to the capillary flow.

Table 6.3 Diffusion Coefficients and Relative Marangoni Numbers of 4 wt% Cellulose Nanocrystal Suspension containing NaCl *

NaCl (mM)	D_{per} ($\mu m^2/s$)	D_{par} ($\mu m^2/s$)	D_{rot} (s^{-1})	Ma
1	0.54	3.23	18	0.6
5	0.52	2.7	24	0.7
10	0.052	0.68	13	3.4

* D_{per} , D_{par} and D_{rot} are respectively the diffusion coefficients perpendicular and parallel to the particle main axis, and the rotational diffusion coefficient around the main axis

Increased Marangoni numbers with increasing NaCl concentration (Table 6.3) indicate that Marangoni flow becomes more important relative to the capillary flow. The diffusion coefficients for $CaCl_2$ containing CNC suspensions could not be determined using the light scattering experiments because the relaxation times were too long, and gelation set in within the measurement time for the relevant $CaCl_2$

concentrations. Due to these limitations in the determination of the diffusion coefficients for the CNC- CaCl_2 system, another dimensionless number which is independent of the diffusion coefficient can be used instead: The importance of the relative magnitude of the Marangoni flow to the processes inside the drying droplet can be described by the modified Péclet number $Pe_{Ma/E} = \frac{\Delta\gamma}{\eta v_c}$ (Equation 5.2) as used in Section 5.2.3. where $\Delta\gamma$ is the surface tension difference between added salt and neat CNC suspension, $v_c \approx J_e/l_c^2$ is the evaporation velocity, J_e is the evaporation flux, l_c is the length scale of the droplet, η is the viscosity of the suspension. The evaporation velocity of salt added CNC suspensions can be determined by the drop volume changes during drying which is obtained by the droplet imaging (Section 3.5). The changes of the mixtures composition do not significantly alter the evaporation velocity of the systems. The calculated values for $Pe_{Ma/E}$ are given in Figure 6-10 for 4 wt% CNC suspension with added salt. It can clearly be seen that $Pe_{Ma/E}$ decreases as time progresses showing that the relative importance of Marangoni flow to capillary flow decreases during the deposition. At the same concentration regimes suspensions with NaCl have higher $Pe_{Ma/E}$ compared to suspensions with CaCl_2 . Although both surface tension gradients and viscosities are higher for the suspensions with CaCl_2 than for the suspensions with NaCl, increase in the viscosities are much dominant in CaCl_2 systems thus $Pe_{Ma/E}$ is reduced for CaCl_2 added suspensions. The changes in the magnitude of $Pe_{Ma/E}$ are small when different salts are compared at the same concentration. On the other hand, when the concentration of salt is doubled, the magnitude of $Pe_{Ma/E}$ decreases nearly by one order of magnitude. In Chapter 5, induced solutal Marangoni flow results in $Pe_{Ma/E}$ in the magnitude of 10^7 when the capillary flow is suppressed whereas for suspensions with salt the magnitude of order for $Pe_{Ma/E}$ ranges between 10^3 and 10^5 .

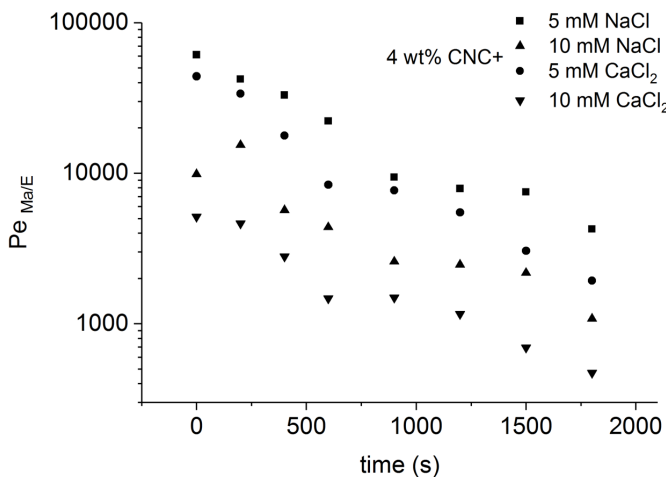


Figure 6-10 $Pe_{Ma/E}$ numbers for 4 wt% CNC with added salt

6.2.2. Analysis of the film deposition

Up to now, the key factors which control the deposition of the colloidal films have been introduced, the discussion will be followed by the analysis of the deposition patterns of the obtained films based on these factors and their importance. Firstly, the deposition of the drying colloidal drops containing NaCl will be discussed which then will be followed by CaCl₂ containing droplets.

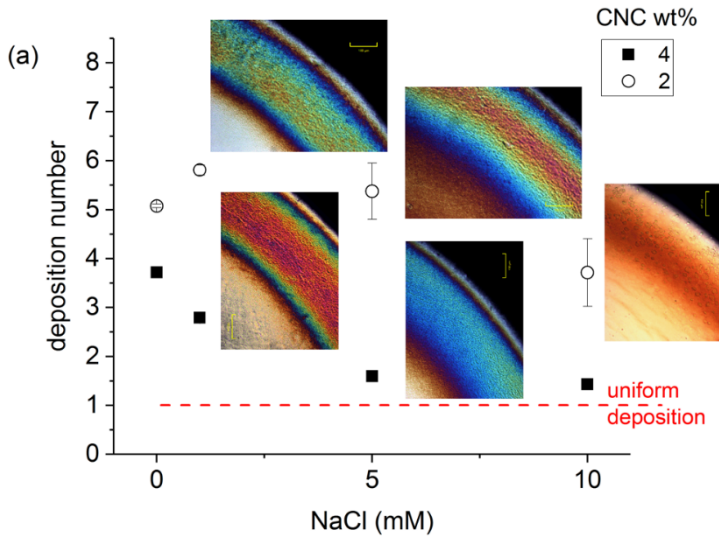
6.2.2.1. Colloidal CNCs drop containing NaCl

The deposition at the outer edges of the drying droplets caused by capillary flow, can be expected to decrease with increasing amounts of added NaCl as the increased viscosity reduces capillary flow (Figure 6-2).

In order to quantify the changes in the final deposit with added salt, a new parameter, the deposition number, DN (Equation 6.2) was defined, relating the maximum height of the outer ring deposit, $h_{max,edge}$, to the average film thickness at the centre of the film, $h_{average,center}$:

$$\text{Deposition Number} = \frac{h_{\max, \text{edge}}}{h_{\text{average}, \text{center}}} \quad (6.2)$$

If the deposition number is larger than 1, the outer ring deposits, i.e. the “coffee-ring”, will dominate in the deposition profile, whereas if it is equal to 1, the deposit is uniform. The deposition number versus NaCl concentration for different CNC concentrations was plotted in Figure 6-11a by using the data from profilometry of the final deposits.



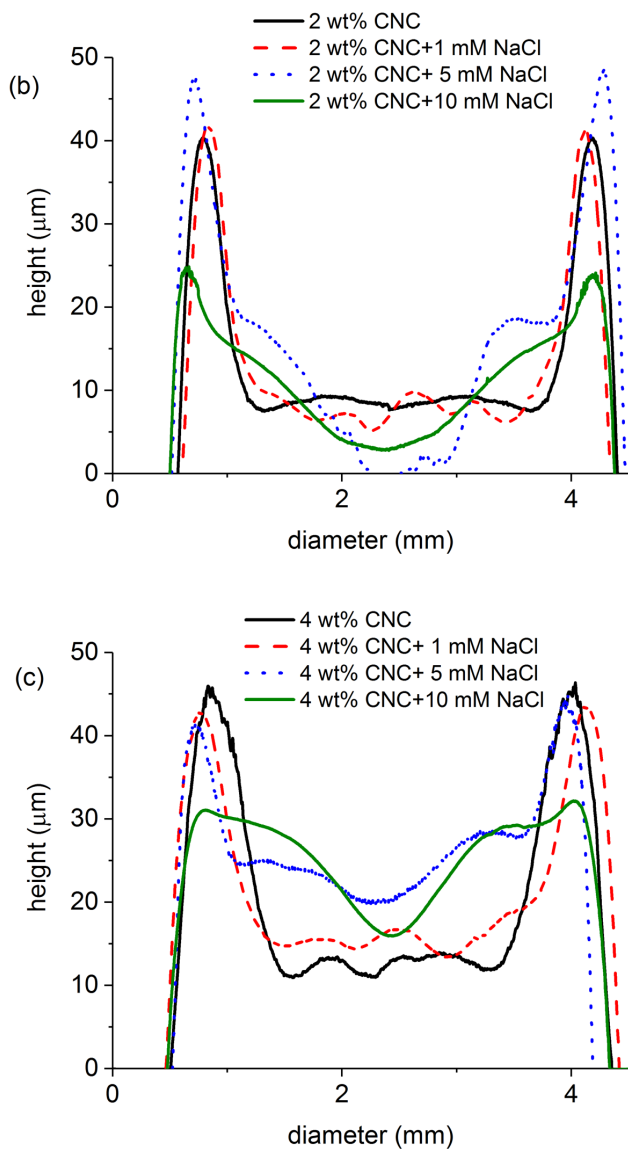


Figure 6-11 (a) Deposition number of films deposited from a CNC-NaCl aqueous mixture with corresponding cross-polarized light microscope images from edge of the films, film profiles for NaCl addition to (b) 2 wt% CNC and (c) 4 wt% CNC suspension

In Figure 6-11a the cross-polarized microscope images of the edge of the films were also illustrated. In Figure 6-11b, c the height profile of the films was shown which are measured with the profilometer (Section 3.7). The trend observed in the deposition numbers gives an idea about the influence of the salt on the colloidal deposition. For instance, at low salt concentration regime the deposition numbers are higher for 2 wt% and 4 wt% compared to high salt concentration regime. This is due to suppressed coffee-ring effect. Deposition numbers are lower for the 4 wt% CNC salt systems since the central deposition of the particles were increased. The calculated deposition numbers were also compared to the ratio of maximum height of the film to minimum height of the film (Table 6.4). Similar trends were obtained for these ratios compared to obtained deposition numbers as defined by Equation 6.2 for both 2 and 4 wt% CNC suspensions with only magnitude of the values differing. A decrease is seen for 4 wt% as the NaCl content is increased, whereas the values for 2 wt% CNC suspensions remained somewhat constant. However, using the average, i.e. the DN as defined by Equation 6.2 has the advantage that it still gives a usable value for deposits which have sections without any deposition. This is seen for 2wt% CNCs with 5mM NaCl, where a central section is left empty because the drying drop becomes depleted of particles at later stages of drying and the minimum height becomes 0.

Table 6.4 Comparison of deposition number (DN) and max/min values of the deposit

NaCl (mM)	2 wt% CNC	2 wt% CNC	4 wt% CNC	4 wt% CNC
	DN	Max/min	DN	Max/min
0	5.1	6.7	3.7	4.8
1	5.8	8	2.8	3.2
5	5.4	Undefined	1.6	1.9
10	3.7	8.9	1.4	1.9

For a colloidal drop of 2 wt% CNC+ 5 mM NaCl, it was observed that there is enhanced accumulation of the particles around the ring which is possibly due to the flocculation as colloidal stability is decreased in the system (Figure 6-5). Consequently, there is a depletion of the particles at the center of the films as seen in Figure 6-11b. Due to this depletion in the films, it becomes unfeasible to determine the concentration changes based on Equation 4.2. $Pe_{Ma/E}$ for this system was determined to be in the order of 10^4 , yet the deposition profile suggests that the capillary flow is effective in the colloidal deposition. Thus, it was presumed that original surface tension gradients are smaller than the determined surface tension changes.

For the 2wt% CNC+10 mM NaCl the dynamic oscillatory tests can be performed, and the system exhibits gel-like behavior (Figure 6-3). This retards the particle motion and limits the capillary flow in the case of the obtained films (Figure 6-11b). As a result, the particle deposition is diminished at the outer ring.

For the suspension of 4 wt % CNC + 5 mM NaCl, the yield stress could not be recorded after initial mixing and the deposition of the film is controlled mostly due to Marangoni and capillary flows for the first 16 min. This is seen in Figure 6-10 where $Pe_{Ma/E}$ is large and decreases during drying. Although the viscosity of the suspension increases gradually with time for this system, it only becomes important in controlling the deposition profile after ~ 16 min (Figure 6-1, 6-10). The viscous resistance was thus found to be effective only from ~ 16 min to the end of the deposition at around 36 min. The contribution of the viscosity of the suspension dominates $Pe_{Ma/E}$ for 4 wt% CNC + 10 mM NaCl which results in lower values than $Pe_{Ma/E}$ for 4 wt% CNC + 5 mM NaCl. The ensuing effect on the deposition is directly seen in the shape of the final deposit with a reduced height of the outer ring deposit relative to the center height (Figure 6-11c). Uniform films could not be obtained for the studied concentration regime since the measured magnitude of the yield stress of the suspension was not sufficient to fully suppress the radial capillary flow (Table 6.2).

6.2.2.2. Colloidal CNCs drop with CaCl_2

The effect of the addition of CaCl_2 to a CNC suspension on the film formation was also studied. Contrary to NaCl , films obtained by the addition of CaCl_2 to the CNC suspension showed a transition from a ring-shaped deposit to dome-shaped deposits (Figure 6-12). It was shown in Table 6.2 that the yield stress is high enough for suspensions containing CaCl_2 to stop capillary flow and this can be seen in the deposits taking on a dome-shaped form. For 4 wt% CNC suspensions, an increase in CaCl_2 concentration from 5 mM to 10 mM led to a decrease in $Pe_{Ma/E}$ throughout the deposition (Figure 6-10) which indicates the dome-shaped deposit is obtained by elastic resistance i.e. an increased yield stress retarding the capillary flow rather than the induced flow due to surface tension gradients after gelation of the drying drop. For 4 wt% CNC + 5 mM CaCl_2 the contribution of the Marangoni flow is higher for the first 10 min than at later times of evaporation. This causes a decrease in terms of the height of the coffee-ring compared to obtained film of 4 wt% CNC (Figure 6-12b). When we compare the films obtained from drying a 4 wt% CNC + 5 mM CaCl_2 suspension to the film obtained from 4 wt% CNC + 10 mM NaCl , both films showed a two-humped deposition pattern. With 5mM CaCl_2 the humps are of lower height at the summit than for 10 mM NaCl , which can be attributed to the higher $Pe_{Ma/E}$ for 4 wt% CNC + 5 mM CaCl_2 during the deposition (Figure 6-10).

The deposition number cannot be calculated for systems where the outer ring is inexistent since the location of the edge cannot be defined. Another observation for the flocculation induced by Ca^{2+} ions is the formation of sharkskin patterns on the surface of the film (Figure 6-12a). Sharkskin occurs because the elasticity induced in the colloidal drop cannot compensate the flocculation related to the crack formation in the colloidal deposit.³¹⁰

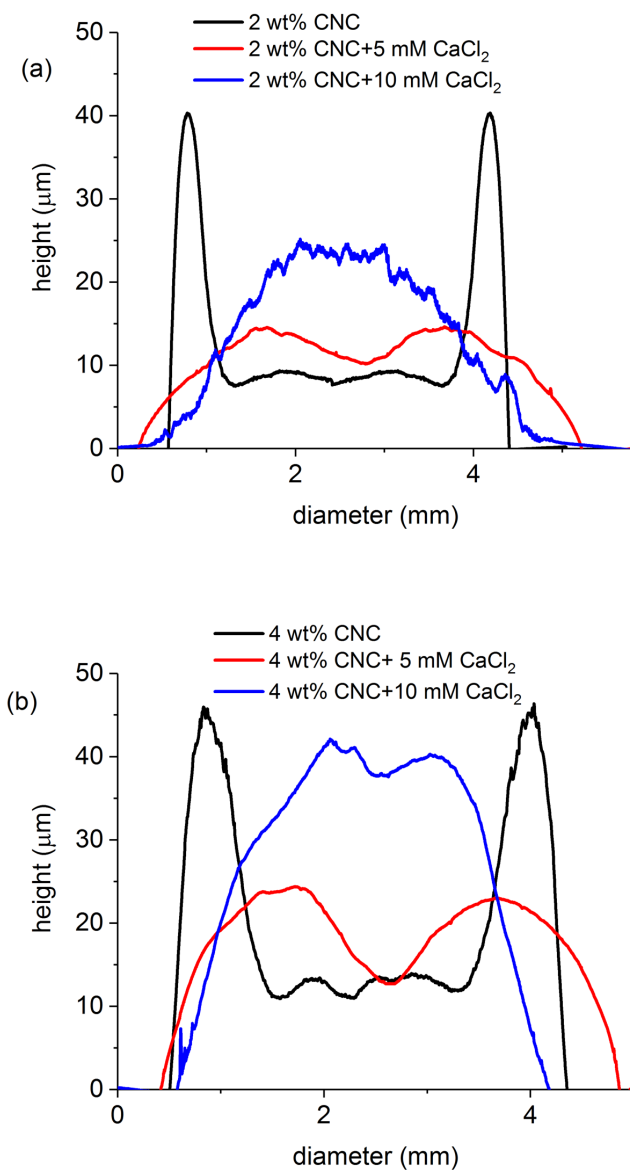


Figure 6-12 Film profiles for CaCl_2 addition to (a) 2 wt% CNC suspension (b) 4 wt% CNC suspension

6.2.3. Optical properties of the films

Considering the color formation of the films under visible light, the pitch distance values of chiral nematic assembly must be reduced to a certain range to reflect visible light.^{12,222} The concentration inside the drying droplets prepared from CNC suspensions with an initial concentration of 4 wt% can be seen to increase as the droplet dries, going through a maximum towards the end of the drying process (Figure 6-1). Clear iridescence was observed for the dried films of initially 4 wt% neat CNCs whereas the droplets prepared from a 4 wt% CNC suspension containing 1 and 5 mM NaCl did not result in iridescent films although their concentration increased sufficiently during drying. This can be due to the loss of the chiral nematic structure (network formation) or because the pitch increased with the increased ionic strength via induced electrostatic interactions³¹¹ or alternatively, gelation may avoid a further decrease in the pitch due to jamming of nanocrystals³¹² or kinetic arrest.³¹³ It was also shown that increased ionic strength shifts the phase sequence towards the isotropic phase.³¹⁴

The observed thickness changes at the perimeter of the films were further analyzed by cross-polarized light microscopy and included in Figure 6-11a for direct comparison. The colored band variation were further correlated using the Michel-Lévy color chart^{315,187} in terms of optical path difference (Appendix A). The changes in colors could be directly related to the thickness changes as described in Section 4.2.2. and is therefore unsurprising.²²² The obtained rainbow pattern is thus a direct effect of the deposit thickness at the outer edge and the slope of outer edge deposit peaks, and can thus be fully controlled by the deposition conditions.

On the other hand, small aggregates (Figure 6-13) were observed for the dried films from 2 wt% CNC + 10 mM NaCl and 4 wt% CNC + 10 mM NaCl suspensions under cross-polarized light which were not seen for dried neat CNC films. The possibility of salt-induced CNC aggregation was also proven by changed electrostatic interactions between CNCs as determined by zeta potential measurements (Figure 6-5).

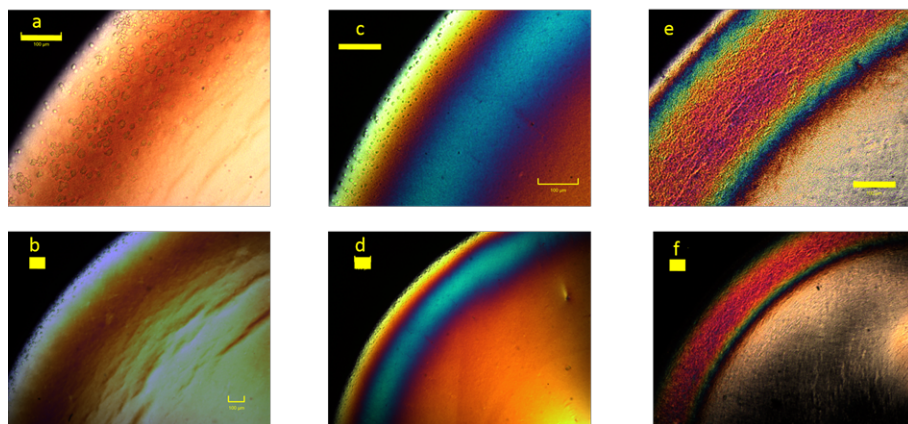


Figure 6-13 Cross-polarized light microscope images for salt added films (a, b) 2 wt% CNC +10 mM NaCl (c, d) 4 wt% CNC +10 mM NaCl and (e, f) neat CNC film 4 wt% CNC (scale bars= 100 μ m)

The center of the films deposited from a CNC-NaCl mixture still has color characterized by cross-polarized light microscopy (Figure 6-13), indicating retained individualization of the nanocrystals and thus sufficient colloidal stability within the time frame of the deposition process. The observed color under cross-polarized light microscope however disappeared around 15mM for NaCl added CNC suspensions of 2 wt% and 4 wt%. For CNC suspensions containing CaCl_2 , the color disappears already at lower concentrations (5mM) for both 2 wt% and 4 wt% CNCs. Films obtained by the addition of CaCl_2 to CNC suspensions showed no color formation under cross-polarized light due to the loss of the structure formation (Figure 6-14). These mixtures led to films of flocculated CNCs which is attributed to the fact that calcium ions form bridging complexes with CNCs, unlike sodium ions which only screen CNC charges.^{175,316}

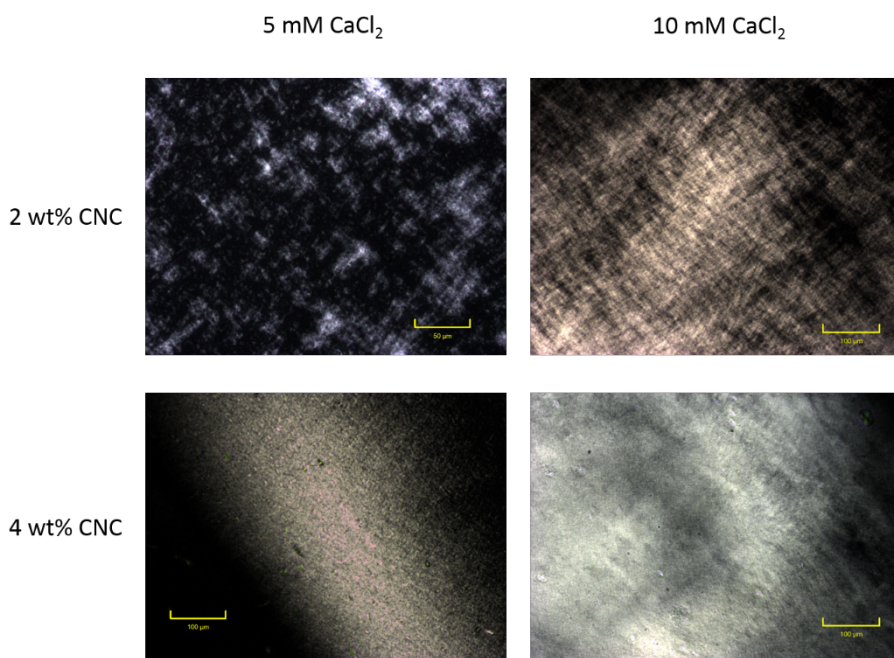


Figure 6-14 Cross-polarized light microscope images for CaCl_2 added films

6.3. Conclusions

The gelation controls the deposition of CNCs at increased salt concentrations, whereas the capillary flow shapes the final deposition pattern of the CNCs for low salt concentrations. However, the addition of salt changes the electrostatic interactions between the CNCs which causes changes in terms of colloidal stability and self-assembly which is crucial to obtain optically active films. Both the addition of NaCl or CaCl_2 induce gelation of the suspension. The addition of NaCl retains the structure formation for CNCs and thus results in optically active films under cross-polarized light, whereas the addition of CaCl_2 results in loss of colloidal stability and the structure formation of CNCs. The transition from ring-shaped deposition to dome-shaped deposition occurs for CaCl_2 added CNC suspensions due to gelation during the deposition.

7. Drying of CNC Films on Superhydrophobic Surfaces

7.1. Introduction

It was already discussed that the coffee-ring effect stems from preferential evaporation of water toward the outer edge of the colloidal drop on hydrophilic substrates. In other words, the local evaporation flux distribution is particularly responsible for the capillary flow which carries the suspended particles towards the edge of the drying drop. Thus, if the local evaporation flux is manipulated along the drop interface, the capillary flow can be reduced to avoid this coffee-ring effect. One way to achieve this scenario is to change the drop geometry to alter the distribution of the local flux at the air-liquid interface as shown by numerical calculations of droplet evaporation (Figure 7-1).^{63,64}

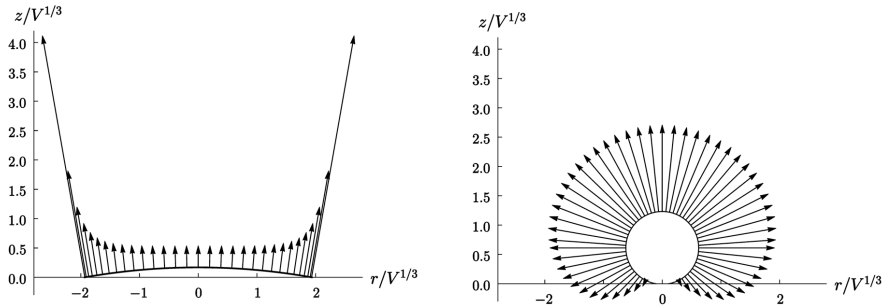


Figure 7-1 Evaporation flux profile of droplets with different geometries (Reproduced with permission from the publisher ⁶³)

In a case study, we aimed to reduce the effect of the capillary flow on the drying of a colloidal film by altering the distribution of the local flux at the air-liquid interface in experiments. In order to achieve this, water was evaporated from colloidal drops of CNCs deposited on superhydrophobic surfaces. Thus, preferential evaporation of water around the outer edge of the drops is avoided. In addition, the effect of the substrate on the colloidal film deposition could also be studied. The advantage of this

strategy is it does not require addition of any additive to the colloidal system such as surfactants or solvents to induce a Marangoni flow to regulate the colloidal deposition. It also provides a well-defined confined assembly area for the CNC suspensions if the constant contact angle is achieved during the evaporation. A similar work was carried out by Parker and co-workers to investigate the hierarchical self-assembly of CNCs in micron-sized droplets which are obtained via a microfluidic assembly.¹⁵ It was reported that the spherical geometry of the droplets affects the colloidal self-assembly process, resulting in concentric ordering within the droplet. The optical properties of the droplets which were immersed in oil were analysed with the polarized microscopy images of the droplets and were compared to the theoretical images which were obtained from numerical simulations.^{15,317}

In our work, the optical properties of the films dried on superhydrophobic substrates were analyzed to check if thin-film interference is occurring as is the case for CNC films dried on hydrophilic substrates. In the last part, the drying of a colloidal drop onto a heated substrate was monitored with thermographic (infrared) camera to characterize the thermal Marangoni flows.

7.2. Results and Discussion

Superhydrophobic surfaces were produced as described in Section 3.4. In the first instance the resultant coating of reasonable adhesion to the glass substrates showed a water contact angle of $165 \pm 2^\circ$. Then a CNC colloidal drops with initial weight concentrations of 1 and 2 wt% were cast onto prepared superhydrophobic substrates. The shape of the drop is drastically changed for drying of 1 wt% CNC relative to the case of drop drying on hydrophilic substrate as can be seen in Figure 7-2.

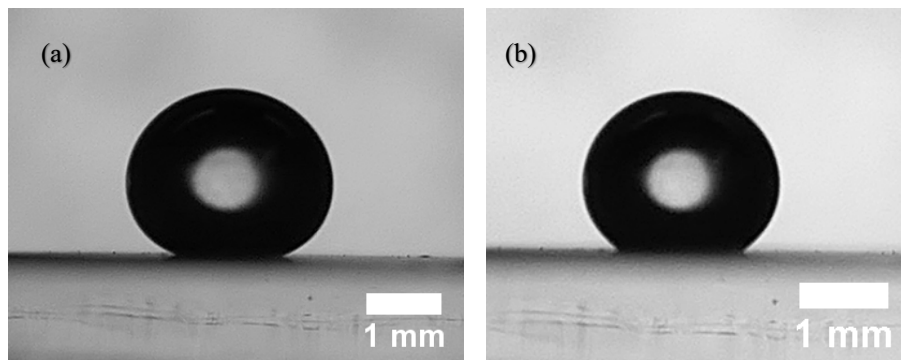


Figure 7-2 (a) CNC colloidal drop (1 wt%) casted onto superhydrophobic substrate and (b) evolution of drop after half an hour

The mode of evaporation was observed to be a constant contact radius in which the contact line remained pinned during the evaporation. For both 1 and 2 wt% CNCs in the colloidal drop, the contact radius was measured to be 0.7 mm. The contact angle of the drops was determined to be $166 \pm 3^\circ$ initially and decreased during evaporation (Figure 7-3).

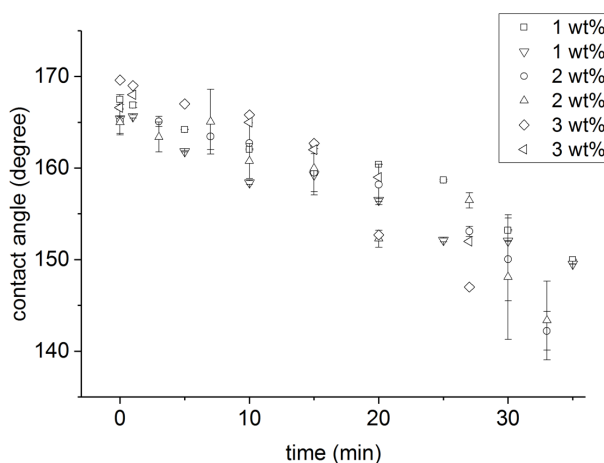


Figure 7-3 Contact angle changes of drying CNC droplets onto coated substrates

This decrease in contact angle during drying is generally observed for constant contact radius evaporation cases.³¹⁸ In the specific case described here, the decrease in contact angle was attributed to the fact that some of the CNC particles dispersed in the drop accumulated at the contact line and locally disturbed the superhydrophobic property of the coating. Before studying the optical properties of the dried films, the plan was to characterize the deposition rate and concentration changes in the drying colloidal drops to be able to understand the self-assembly process. However, the model proposed in Section 4.2.1 could not be implemented to the colloidal drops drying onto superhydrophobic substrates since the evaporation process was observed to be occurring via a vertical drying in which the evaporation of water occurred without retraction of the contact line. In the literature, a model was reported to solve the rate of mass loss from colloidal drops with higher contact angles by mimicking the solution of electric potential around a charged lens-shaped conductor.³¹⁹ This leads to a diffusion based analytical model in which the diffusive flux from the droplet surface has to be characterized to determine the rate of mass loss during drying. Another alternative is to analyze the images of the drying drops to calculate the volume changes and thus the concentration of the colloidal drops over time. However, the determination of drop volumes via the image analysis become challenging since the shape of drops exhibits flattening on the side where it is in contact with solid surfaces. The analysis was continued in a qualitative way and the optical properties of the obtained films were investigated. Cross-polarized light images of films obtained from drying colloidal drops obtained from CNC suspension of initial concentration of 1 wt%, 2 wt% and 3.5 wt% showed that the films exhibited a very similar behavior in terms of the optical properties independent of the concentration of the suspensions. Cross-polarized light microscope images obtained for the dried film of 1-3.5 wt% CNC are shown in Figure 7-4.

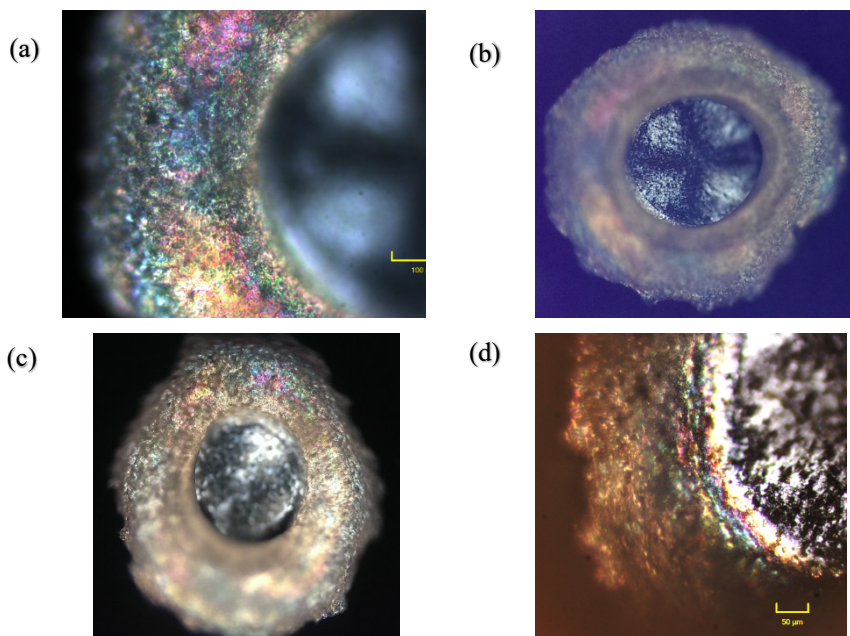


Figure 7-4 Cross-polarized light microscope images of dried films (a, b) 1wt% (c) 2 wt% and (d) 3.5 wt%

The first observation in terms of color formation compared to the dried films on uncoated glass substrates was that there was no rainbow-like color formation at the outer edge of the films. Instead, color spots were observed in a random manner around the rim of the film. This was due to either irregularities in thickness throughout the surface of the film or due to the microstructure of the CNC particles. The cross-polarized images showed that there is a thickness difference between the center of the film and its rim which is proven by the loss of the focus of image in related areas. Therefore, the morphology of the obtained films is resembling to the bowl-shaped deposition. This is actually unsurprising since such cavity formations observed in films are normally due to the buckling instabilities.^{318,320,321} It is known that when water evaporates from the colloidal drop, the CNC particles can accumulate at the air-liquid interface causing skin formation. The reason for the buckling instability induced during the evaporation is the sol-gel transition of the skin formed at the air-

liquid interface. Skin formation is favored for colloidal drops drying onto superhydrophobic substrates since the preferential evaporation towards the contact line is suppressed. Therefore, it is anticipated that the bowl-shaped depositions obtained here are induced by the buckling instabilities during the evaporation instead of the coffee-ring effect.³²²

7.2.1. Thermal Marangoni flow

Colloidal drops of CNCs were also dried using the same coated substrate using a peltier heating stage. In the case of drying films dried on heated substrates, thermal Marangoni flow might become pronounced and influence the particle deposition behavior. This situation can be explained using Figure 7-5. In general, the regions with a low temperature possess a high surface tension whereas the regions with a high temperature possess a low surface tension. It is due to fact that intermolecular attractive forces between molecules decreases at increased temperatures and increases at decreased temperatures.³²³ Thus, the direction of the flow is dictated by these surface tension gradients.

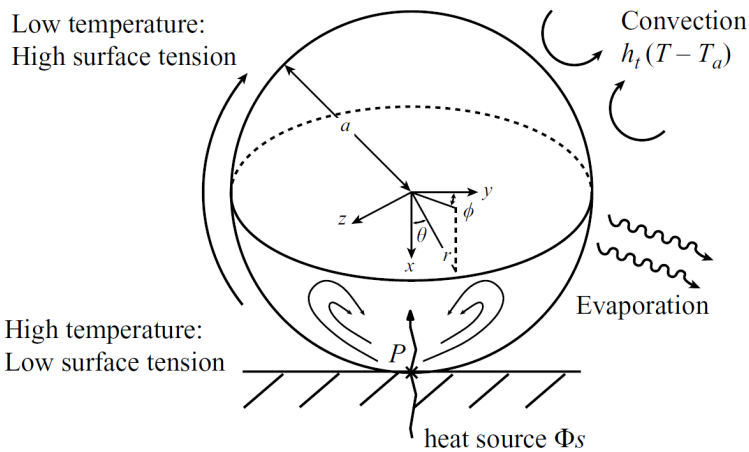


Figure 7-5 Schematic description of thermal Marangoni flow for droplets on superhydrophobic substrates (Reproduced with permission from the publisher³²⁴)

To be able to characterize the influence of thermal Marangoni flow, the temperature gradients in the drying colloidal drops were further characterized. When the temperature of the heat source was at 45 °C, the air-liquid interface of the drop could be distinguished, and the temperature profile could be analyzed to understand the Marangoni flow inside the colloidal drops (Figure 7-6). The temperature profile measured represents the air-liquid interface across the droplet since water was opaque to the infrared radiation. In this analysis, the droplet surface temperature could be used to estimate the surface tension gradients and the magnitude of the Marangoni flow in the drying drops.

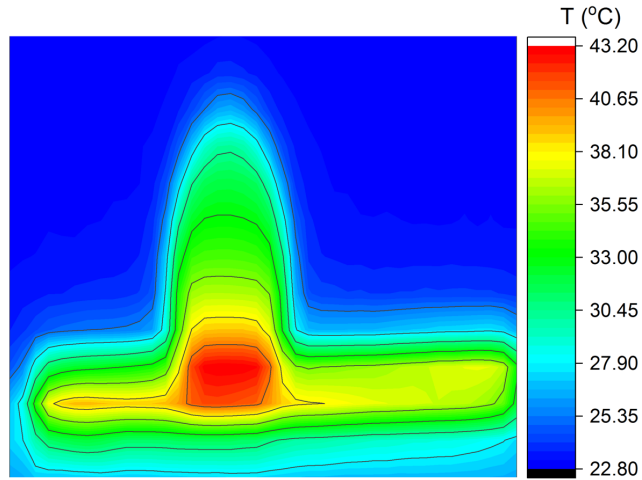


Figure 7-6 Temperature profile of 2 wt% CNC drop after the initial casting

The magnitude of the Marangoni flow is scaled with $d\gamma/dr$ as this gradient is responsible for the Marangoni stress. To be able to analyze this contribution, the chain rule was used (Equation 7.1);

$$\frac{d\gamma}{dr} = \frac{d\gamma}{dT} \frac{dT}{dr} \quad (7.1)$$

where $d\gamma/dT$ represents the surface tension changes with respect to the changes in temperature and dT/dr is the temperature gradient across the interface which is extracted from the temperature profile obtained by the infrared camera.

The temperature profile of drying 2 wt% CNCs drop was recorded as a function of time and used together with the surface tension changes calculated from Equation 7.1, in order to characterize the Marangoni stresses caused by the temperature gradients shown in Figure 7-6.^{72,325} The temperature gradients were acquired by thermal imaging from side view of the drop. The temperature of the drop is highest close to the heat source and decreases as a function of the height. Since these results are available in two-dimensional space it is difficult to predict three-dimensional information of the temperature gradients on the surface of the spheroid. The analysis of temperature gradients is based on the temperature changes on the axis perpendicular to the heat source. For a colloidal drop of 2 wt% CNC, time-dependent changes of the surface tension changes were extracted with respect to the given height of the drop as shown in Figure 7-7. A similar trend is observed at different times of evaporation and a shift is witnessed due to the reduction of height of drops. The magnitude of the Marangoni flow is higher for the position of the drop where a high surface tension gradient exists. This approach could be implemented for the numerical simulation of the drying colloidal drops on heated superhydrophobic surfaces.³²⁶ Yet, there remains a need to characterize the stresses induced by skin formation to fully understand the flow behavior.

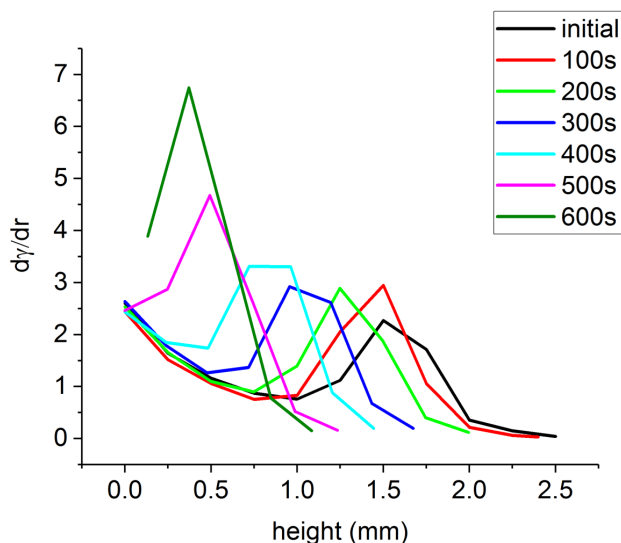


Figure 7-7 Magnitude of Marangoni stresses at different times of evaporation

7.3. Conclusions

Drying CNCs colloidal drops onto superhydrophobic substrates alters the optical properties of the dried films. The strategy of drying colloidal drops of CNCs onto superhydrophobic substrates could be used as a platform to study the confined self-assembly of CNC in a shrinking geometry. This way the coffee-ring effect can be avoided, and the self-assembly process can be investigated with a uniform spatial concentration inside the drying drop. In addition, the surface tension gradients can be induced by the temperature gradients which can further be studied to control the fluid flow and thus the particle motion in the drying colloidal drops.

8. General Conclusions and Outlook

CNCs are a very promising material to be employed in inks to generate structural color. There have been already several attempts in areas of inkjet printing and 3D printing to investigate the applicability of CNC films.^{48,244,245,327,328} The optical properties of the films is largely controlled by the self-assembly behavior of CNCs and the method of production of the films. Self-assembly of CNCs depends on the behavior of the drying CNC suspension. For instance, phase transitions occur with increasing concentration of the particles. However, the coexistence of different phases namely isotropic and chiral nematic leads to biphasic systems, which can cause possible non-uniformities in the self-assembly process. For this reason, the onset of phase transitions and the orientation of chiral nematic domains has to be better understood to have a control in the self-assembly process. In addition, the properties of the particles such as surface charge density, shape and size distribution have to be regulated to have a control for the onset of phase transitions, colloidal stability and rheological properties of the suspensions.

On the other hand, methods of film production influence the optical properties of the obtained films. Several methods such as blade coating, dip coating, drop-casting and spin coating were introduced in Section 2.8. Depending on the method, differences in the particle alignment and the deposition of the particles can be observed in the produced films. For instance, applied shear affects the orientation of the rod-shaped particles in the case of blade coating and spin coating. On the contrary, the effect of shear is less pronounced in the case of drop-casting. However, fluid flow in drying drops can influence the alignment of the particles.²⁷⁵ Although many of the studies have focused on the production of the films via drying CNC suspension onto different substrates including in petri dish, and on AFM meshes and glass slides, these studies only characterized the initial properties of the suspensions and the final properties of the obtained films.^{11,12,236} Drying of CNC films leads to complex systems in which particle transfer and deposition during drying determines the final morphology of the obtained films. Thus, there is a need for a dynamic characterization of the drying process. Tracking of the individual nanocrystals in drying drops is not feasible due to

the limitations of the microscopic methods. Instead, computational fluid dynamics can be useful to understand the velocity field and the particle motion inside a drying colloidal drop. Yet, these have not been studied for CNC films since many of the parameters such as concentration and the viscosity of the suspensions are subject to change during drying and has to be known for numerical analysis.

The dynamic self-assembly of CNCs takes place during drying which is affected by the concentration changes. To this end, a new analytical method was developed which can be used to determine the concentration changes in drying colloidal drops. Thus, the phase transitions and cholesteric pitch of chiral nematic assembly can be correlated with the concentration changes. This method is advantageous over simulation-based calculations since in the latter the prediction of particle motion hence the understanding of the deposition behavior is very complex.

The relation between the deposition pattern and the optical properties of CNC films showed that thickness changes occurred due to the coffee-ring effect and these changes are responsible for the thin film interference at the perimeter of the films. On the other hand, the radial color changes observed by the naked eye in the absence of thickness gradients in the CNC films was attributed to concentration changes in the drying colloidal suspensions. It can also be reasoned that the concentration changes during drying alter the chiral nematic pitch distance. At later times of drying of the colloidal drop, gelation might take place which avoids further changes in the pitch distance. The observation of different color spots at length scales of a few microns around the center of the film is induced by local defects in the self-assembly process of CNCs. For instance, flow dynamics during drying can cause local defects that are produced by the sliding of cholesteric phases.²⁷⁵ In addition, the control of helix orientation is challenging during drying of CNC films.

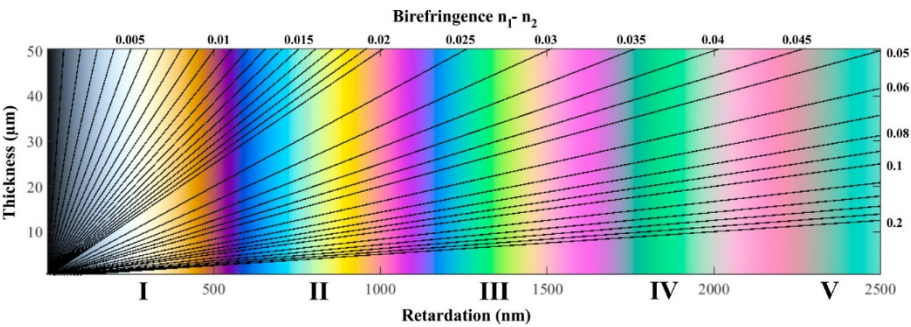
Determination of helical pitch lengths in films was limited due to the optical resolution of light microscopy. For this reason, the helicoidal nanostructure of the CNC films has to be characterized by electron microscope studies. X-ray scattering techniques such as GI-SAXS can also be employed to study the self-assembly and the alignment of rod-like shaped CNCs in films.²⁰²

The developed understanding of the colloidal deposition process enabled us to further design and control the deposition of the particles via manipulation of the fluid flow inside the droplet. The influencing forces in the deposition process were successfully described using the dimensionless number analysis, which enabled us to describe the studied systems and develop a framework to control the deposition profile. In Chapter 5, uniform deposition of CNC films was achieved by induced solutal Marangoni flow in the drying drops. The magnitude of the Marangoni flow was increased by means of increased surface tension gradients. This was accomplished by diffusion of ethanol vapor into drying colloidal drop of CNC suspension. Retaining the colloidal stability was necessary to preserve the structure formation and thus iridescence for the obtained films. Since the colloidal drops were exposed to ethanol atmosphere, excess diffusion of ethanol caused aggregation of CNCs. To avoid this problem, the vapor composition of atmosphere was altered via using reservoir of ethanol-water mixtures with different mole fractions in a closed environment. In addition, the suspension behavior of ethanol added CNC suspensions were tested by rheological and zeta potential measurements. Increase of ethanol amount for CNC aqueous suspensions caused an increase in the viscosity of the suspensions. This was due to the aggregation of CNCs since the electrostatic interactions between particles were impaired by the addition of ethanol.

Alternatively, different organic solvents that are miscible to water and have different surface tension behavior can be tested to induce solutal Marangoni flow. Naturally, the colloidal stability of the suspension has to be considered for the selection of the solvent. For instance, solvents having dielectric permittivity close to that of water (e.g. formamide) can be a possible candidate. Thus, the disruption of the electrostatic interactions between CNCs can be minimized and the self-assembly behavior which is linked to helical pitch length can also be controlled together with the deposition profile to manipulate the optical behavior of the films.²⁹⁵ Additionally, the drying of colloidal drops can be coupled with an external stimulus such as an electric field or a magnetic field to control the self-assembly behavior of the CNCs.^{197,198,199}

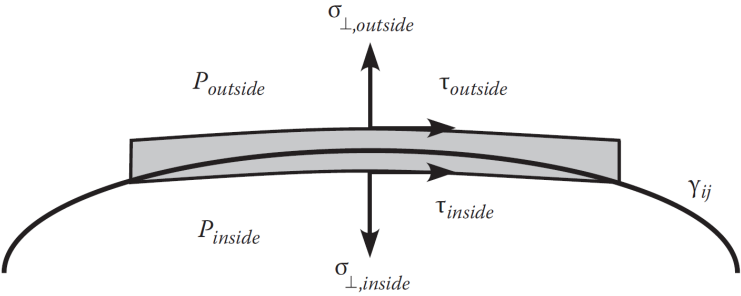
Gel formation was shown to restrict the radial capillary flow in drying drops and thus particle motion towards the drop edge. In general, gelation controls the deposition of CNCs at increased salt concentrations, whereas capillary flow shapes the final deposition pattern of CNCs for low salt concentrations. Control of the colloidal deposition and the self-assembly of CNCs can be tested using other salts which induce gelation in colloidal suspensions. As a result, viscoelastic inks can be produced from CNCs which can be used in 3D printing applications.

Appendix A: The Michel-Lévy Interference Color Chart



Reproduced with permission from the publisher ³²⁹

Appendix B: Fluid Stresses at the Interface



Reproduced with permission from the publisher ³³⁰

References

1. Roduner, E., Size matters: why nanomaterials are different. *Chemical Society Reviews* **2006**, 35 (7), 583-592.
2. Altenbach, H., Fundamentals of continuum mechanics – classical approaches and new trends. *Journal of Physics: Conference Series* **2018**, 991 (1), 012003.
3. Liu, X.; Yuan, F.; Wei, Y., Grain size effect on the hardness of nanocrystal measured by the nanosize indenter. *Applied Surface Science* **2013**, 279, 159-166.
4. Xia, Y.; Yang, H.; Campbell, C. T., Nanoparticles for Catalysis. *Accounts of Chemical Research* **2013**, 46 (8), 1671-1672.
5. Son, Y.; Park, M.; Son, Y.; Lee, J.-S.; Jang, J.-H.; Kim, Y.; Cho, J., Quantum Confinement and Its Related Effects on the Critical Size of GeO₂ Nanoparticles Anodes for Lithium Batteries. *Nano Letters* **2014**, 14 (2), 1005-1010.
6. NSTC/COT/NSET NNI budget. <https://www.nano.gov/about-nni/what/funding>.
7. Mensah, T. O.; Wang, B.; Bothun, G.; Davis, V.; Winter, J., *Nanotechnology Commercialization: Manufacturing Processes and Products*. Wiley: 2017.
8. Roco, M. C.; Mirkin, C. A.; Hersam, M. C., Nanotechnology research directions for societal needs in 2020: summary of international study. *J Nanopart Res* **2011**, 13 (3), 897-919.
9. Rodzinski, A.; Guduru, R.; Liang, P.; Hadjikhani, A.; Stewart, T.; Stimpf, E.; Runowicz, C.; Cote, R.; Altman, N.; Datar, R.; Khizroev, S., Targeted and controlled anticancer drug delivery and release with magnetoelectric nanoparticles. *Scientific Reports* **2016**, 6, 20867.
10. Yablonovitch, E., Photonic Crystals: Semiconductors of Light. *Scientific American* **2001**, 285 (6), 46-55.
11. Dumanli, A. G.; van der Kooij, H. M.; Kamita, G.; Reisner, E.; Baumberg, J. J.; Steiner, U.; Vignolini, S., Digital Color in Cellulose Nanocrystal Films. *ACS Appl. Mater. Interfaces* **2014**, 6 (15), 12302-12306.
12. Mu, X.; Gray, D. G., Formation of Chiral Nematic Films from Cellulose Nanocrystal Suspensions Is a Two-Stage Process. *Langmuir* **2014**, 30 (31), 9256-9260.
13. Wilts, B. D.; Dumanli, A. G.; Middleton, R.; Vukusic, P.; Vignolini, S., Invited Article: Chiral optics of helicoidal cellulose nanocrystal films. *APL Photonics* **2017**, 2 (4), 040801.
14. Lagerwall, J. P. F.; Schütz, C.; Salajkova, M.; Noh, J.; Hyun Park, J.; Scalia, G.; Bergström, L., Cellulose nanocrystal-based materials: from liquid crystal self-assembly and glass formation to multifunctional thin films. *NPG Asia Mater.* **2014**, 6, e80.
15. Parker, R. M.; Frka-Petesic, B.; Guidetti, G.; Kamita, G.; Consani, G.; Abell, C.; Vignolini, S., Hierarchical Self-Assembly of Cellulose Nanocrystals in a Confined Geometry. *ACS Nano* **2016**, 10 (9), 8443-8449.
16. Revol, J.; Bradford, H.; Giasson, J.; Marchessault, R. H.; Gray, D. G., Helicoidal self-ordering of cellulose microfibrils in aqueous suspension. *International Journal of Biological Macromolecules* **1992**, 14 (3), 170-172.

17. Burda, C.; Chen, X.; Narayanan, R.; El-Sayed, M. A., Chemistry and Properties of Nanocrystals of Different Shapes. *Chem. Rev.* **2005**, *105* (4), 1025-1102.
18. Pignataro, B., *Ideas in Chemistry and Molecular Sciences*. Wiley: 2010.
19. Nunes, R., Sculpting Nanometric Patterns: The Top-down Approach. In *Ideas in Chemistry and Molecular Sciences*, Wiley: 2010.
20. Gates, B. D.; Xu, Q.; Stewart, M.; Ryan, D.; Willson, C. G.; Whitesides, G. M., New Approaches to Nanofabrication: Molding, Printing, and Other Techniques. *Chem. Rev.* **2005**, *105* (4), 1171-1196.
21. Chou, S. Y.; Krauss, P. R.; Renstrom, P. J., Imprint Lithography with 25-Nanometer Resolution. *Science* **1996**, *272* (5258), 85-87.
22. Boles, M. A.; Engel, M.; Talapin, D. V., Self-Assembly of Colloidal Nanocrystals: From Intricate Structures to Functional Materials. *Chem. Rev.* **2016**, *116* (18), 11220-11289.
23. Casalini, S.; Bortolotti, C. A.; Leonardi, F.; Biscarini, F., Self-assembled monolayers in organic electronics. *Chemical Society Reviews* **2017**, *46* (1), 40-71.
24. Grzelczak, M.; Vermant, J.; Furst, E. M.; Liz-Marzán, L. M., Directed Self-Assembly of Nanoparticles. *ACS Nano* **2010**, *4* (7), 3591-3605.
25. Bishop, K. J. M.; Wilmer, C. E.; Soh, S.; Grzybowski, B. A., Nanoscale Forces and Their Uses in Self-Assembly. *Small* **2009**, *5* (14), 1600-1630.
26. Ozin, G. A.; Arsenault, A., *Nanochemistry: A Chemical Approach to Nanomaterials*. Royal Society of Chemistry: 2015.
27. Li, B.; Zhou, D.; Han, Y., Assembly and phase transitions of colloidal crystals. *Nature Reviews Materials* **2016**, *1*, 15011.
28. Ulama, J.; Zackrisson Oskolkova, M.; Bergenholtz, J., Monodisperse PEGylated Spheres: An Aqueous Colloidal Model System. *The Journal of Physical Chemistry. B* **2014**, *118* (9), 2582-2588.
29. Cai, W.; Yang, H.; Guo, X., A Facile Synthesis of Nanocrystalline Spherical TiO₂ Particles and its Photoluminescent Properties. *Procedia Engineering* **2014**, *94*, 71-75.
30. Nikoobakht, B.; El-Sayed, M. A., Preparation and Growth Mechanism of Gold Nanorods (NRs) Using Seed-Mediated Growth Method. *Chem. Mater.* **2003**, *15* (10), 1957-1962.
31. Matthias, S.; Schilling, J.; Nielsch, K.; Müller, F.; Wehrspohn, R. B.; Gösele, U., Monodisperse Diameter-Modulated Gold Microwires. *Advanced Materials* **2002**, *14* (22), 1618-1621.
32. Chandrasekhar, S.; Chandrasekhar, S.; Press, C. U., *Liquid Crystals*. Cambridge University Press: 1992.
33. Lettinga, M. P.; Dogic, Z.; Wang, H.; Vermant, J., Flow Behavior of Colloidal Rodlike Viruses in the Nematic Phase. *Langmuir* **2005**, *21* (17), 8048-8057.
34. Buining, P. A.; Philipse, A. P.; Lekkerkerker, H. N. W., Phase Behavior of Aqueous Dispersions of Colloidal Boehmite Rods. *Langmuir* **1994**, *10* (7), 2106-2114.
35. Fraden, S.; Maret, G.; Caspar, D. L. D.; Meyer, R. B., Isotropic-nematic phase transition and angular correlations in isotropic suspensions of tobacco mosaic virus. *Physical Review Letters* **1989**, *63* (19), 2068-2071.

36. Zaccone, A.; Wu, H.; Lattuada, M.; Morbidelli, M., Correlation between Colloidal Stability and Surfactant Adsorption/Association Phenomena Studied by Light Scattering. *The Journal of Physical Chemistry B* **2008**, *112* (21), 6733-6733.
37. Celasco, E.; Valente, I.; Marchisio, D. L.; Barresi, A. A., Dynamic Light Scattering and X-ray Photoelectron Spectroscopy Characterization of PEGylated Polymer Nanocarriers: Internal Structure and Surface Properties. *Langmuir* **2014**, *30* (28), 8326-8335.
38. Crucho, C. I. C.; Barros, M. T., Polymeric nanoparticles: A study on the preparation variables and characterization methods. *Materials Science and Engineering: C* **2017**, *80*, 771-784.
39. Vogel, N.; Retsch, M.; Fustin, C.-A.; del Campo, A.; Jonas, U., Advances in Colloidal Assembly: The Design of Structure and Hierarchy in Two and Three Dimensions. *Chem. Rev.* **2015**, *115* (13), 6265-6311.
40. Rajagopalan, T.; Venumadhav, K.; Arkasubhra, G.; Nripen, C.; Keshab, G.; Shubhra, G., Nanomaterial processing using self-assembly-bottom-up chemical and biological approaches. *Reports on Progress in Physics* **2013**, *76* (6), 066501.
41. Bigioni, T. P.; Lin, X.-M.; Nguyen, T. T.; Corwin, E. I.; Witten, T. A.; Jaeger, H. M., Kinetically driven self assembly of highly ordered nanoparticle monolayers. *Nat. Mater.* **2006**, *5* (4), 265-270.
42. Davidson, Z. S.; Huang, Y.; Gross, A.; Martinez, A.; Still, T.; Zhou, C.; Collings, P. J.; Kamien, R. D.; Yodh, A. G., Deposition and drying dynamics of liquid crystal droplets. **2017**, *8*, 15642.
43. Daly, R.; Kotova, O.; Boese, M.; Gunnlaugsson, T.; Boland, J. J., Chemical Nano-Gardens: Growth of Salt Nanowires from Supramolecular Self-Assembly Gels. *ACS Nano* **2013**, *7* (6), 4838-4845.
44. Rabani, E.; Reichman, D. R.; Geissler, P. L.; Brus, L. E., Drying-mediated self-assembly of nanoparticles. *Nature* **2003**, *426*, 271.
45. Deegan, R. D.; Bakajin, O.; Dupont, T. F.; Huber, G.; Nagel, S. R.; Witten, T. A., Contact line deposits in an evaporating drop. *Physical review E* **2000**, *62* (1), 756.
46. Deegan, R. D.; Bakajin, O.; Dupont, T. F.; Huber, G.; Nagel, S. R.; Witten, T. A., Capillary flow as the cause of ring stains from dried liquid drops. *Nature* **1997**, *389*, 827.
47. Mampallil, D., Some physics inside drying droplets. *Resonance* **2014**, *19* (2), 123-134.
48. Maren, R.; Fernando, N., Deposition of Cellulose Nanocrystals by Inkjet Printing. In *Model Cellulosic Surfaces*, American Chemical Society: 2009; Vol. 1019, pp 157-171.
49. Sun, J.; Bao, B.; He, M.; Zhou, H.; Song, Y., Recent Advances in Controlling the Depositing Morphologies of Inkjet Droplets. *ACS Appl. Mater. Interfaces* **2015**, *7* (51), 28086-28099.
50. Yakovlev, A. V.; Milichko, V. A.; Vinogradov, V. V.; Vinogradov, A. V., Inkjet Color Printing by Interference Nanostructures. *ACS Nano* **2016**, *10* (3), 3078-3086.

51. Wu, L.; Dong, Z.; Li, F.; Zhou, H.; Song, Y., Emerging Progress of Inkjet Technology in Printing Optical Materials. *Advanced Optical Materials* **2016**, 1915-1932.
52. Tong, S.; Sun, J.; Yang, J., Printed Thin-Film Transistors: Research from China. *ACS Appl. Mater. Interfaces* **2018**.
53. Amjad, M.; Yang, Y.; Raza, G.; Gao, H.; Zhang, J.; Zhou, L.; Du, X.; Wen, D., Deposition pattern and tracer particle motion of evaporating multi-component sessile droplets. *Journal of Colloid and Interface Science* **2017**, 506, 83-92.
54. Vélez-Cordero, J. R.; Yáñez Soto, B.; Arauz-Lara, J. L., Transport of Colloids along Corners: Visualization of Evaporation-Induced Flows beyond the Axisymmetric Condition. *Langmuir* **2016**, 32 (32), 8171-8181.
55. Kwan Hyung, K.; Sang Joon, L.; Choung Mook, L.; In Seok, K., Quantitative visualization of flow inside an evaporating droplet using the ray tracing method. *Measurement Science and Technology* **2004**, 15 (6), 1104.
56. Truskett, V. N.; Stebe, K. J., Influence of Surfactants on an Evaporating Drop: Fluorescence Images and Particle Deposition Patterns. *Langmuir* **2003**, 19 (20), 8271-8279.
57. Hu, H.; Larson, R. G., Analysis of the Microfluid Flow in an Evaporating Sessile Droplet. *Langmuir* **2005**, 21 (9), 3963-3971.
58. Ruzicka, M. C., On dimensionless numbers. *Chemical Engineering Research and Design* **2008**, 86 (8), 835-868.
59. Rajneesh, B.; Xiaohua, F.; Daniel, A., Pattern formation during the evaporation of a colloidal nanoliter drop: a numerical and experimental study. *New J. Phys.* **2009**, 11 (7), 075020.
60. Widjaja, E.; Harris, M. T., Particle deposition study during sessile drop evaporation. *AIChE Journal* **2008**, 54 (9), 2250-2260.
61. Hwang, H.; Son, G., Numerical Simulation of Evaporation-Induced Particle Line Formation on a Moving Substrate. *Heat Transfer Eng.* **2017**, 1-7.
62. Fischer, B. J., Particle Convection in an Evaporating Colloidal Droplet. *Langmuir* **2002**, 18 (1), 60-67.
63. Stauber, J. M.; Wilson, S. K.; Duffy, B. R.; Sefiane, K., Evaporation of Droplets on Strongly Hydrophobic Substrates. *Langmuir* **2015**, 31 (12), 3653-3660.
64. Xie, C.; Liu, G.; Wang, M., Evaporation Flux Distribution of Drops on a Hydrophilic or Hydrophobic Flat Surface by Molecular Simulations. *Langmuir* **2016**, 32 (32), 8255-8264.
65. Bijal, B. P.; Ying, D., Multiscale assembly of solution-processed organic electronics: the critical roles of confinement, fluid flow, and interfaces. *Nanotechnology* **2018**, 29 (4), 044004.
66. Mampallil, D.; Eral, H. B., A review on suppression and utilization of the coffee-ring effect. *Advances in Colloid and Interface Science* **2018**, 252, 38-54.
67. Brutin, D., *Droplet Wetting and Evaporation: From Pure to Complex Fluids*. Elsevier Science: 2015.
68. Hu, H.; Larson, R. G., Marangoni Effect Reverses Coffee-Ring Depositions. *J. Phys. Chem. B* **2006**, 110 (14), 7090-7094.

69. Van der Mensbrugghe, G. L., *Sur la tension superficielle des liquides considérée au point de vue de certains mouvements observés à leur surface*. Hayez: 1869.
70. Marangoni, C., Study on surface tension of fluid. *Ann. Phys. Chem* **1871**, 143, 337-354.
71. Scriven, L. E.; Sternling, C. V., The Marangoni Effects. *Nature* **1960**, 187, 186.
72. Hu, H.; Larson, R. G., Analysis of the Effects of Marangoni Stresses on the Microflow in an Evaporating Sessile Droplet. *Langmuir* **2005**, 21 (9), 3972-3980.
73. Kyoko, N.; Kaoru, N.; Motofumi, S., Investigation of transition from thermal- to solutal-Marangoni flow in dilute alcohol/water mixtures using nanoplasmonic heaters. *Nanotechnology* **2018**, 29 (6), 065201.
74. Varanakkottu, S. N.; Anyfantakis, M.; Morel, M.; Rudiuk, S.; Baigl, D., Light-Directed Particle Patterning by Evaporative Optical Marangoni Assembly. *Nano Letters* **2016**, 16 (1), 644-650.
75. Anyfantakis, M.; Varanakkottu, S. N.; Rudiuk, S.; Morel, M.; Baigl, D., Evaporative Optical Marangoni Assembly: Tailoring the Three-Dimensional Morphology of Individual Deposits of Nanoparticles from Sessile Drops. *ACS Applied Materials & Interfaces* **2017**, 9 (42), 37435-37445.
76. Doumenc, F.; Guerrier, B., Self-patterning induced by a solutal Marangoni effect in a receding drying meniscus. *EPL (Europhysics Letters)* **2013**, 103 (1), 14001.
77. Kim, H.; Muller, K.; Shardt, O.; Afkhami, S.; Stone, H. A., Solutal Marangoni flows of miscible liquids drive transport without surface contamination. *Nat. Phys.* **2017**, 13, 1105.
78. Singer, J. P., Thermocapillary approaches to the deliberate patterning of polymers. *Journal of Polymer Science Part B: Polymer Physics* **2017**, 55 (22), 1649-1668.
79. Giorgiutti-Dauphiné, F.; Pauchard, L., Drying drops. *The European Physical Journal E* **2018**, 41 (3), 32.
80. (a) Anyfantakis, M.; Geng, Z.; Morel, M.; Rudiuk, S.; Baigl, D., Modulation of the Coffee-Ring Effect in Particle/Surfactant Mixtures: the Importance of Particle-Interface Interactions. *Langmuir* **2015**, 31 (14), 4113-4120; (b) Marin, A.; Liepelt, R.; Rossi, M.; Kahler, C. J., Surfactant-driven flow transitions in evaporating droplets. *Soft Matter* **2016**; (c) Karapetsas, G.; Chandra Sahu, K.; Matar, O. K., Evaporation of Sessile Droplets Laden with Particles and Insoluble Surfactants. *Langmuir* **2016**.
81. Seo, C.; Jang, D.; Chae, J.; Shin, S., Altering the coffee-ring effect by adding a surfactant-like viscous polymer solution. *Scientific Reports* **2017**, 7 (1), 500.
82. Still, T.; Yunker, P. J.; Yodh, A. G., Surfactant-Induced Marangoni Eddies Alter the Coffee-Rings of Evaporating Colloidal Drops. *Langmuir* **2012**, 28 (11), 4984-4988.
83. Kim, H.; Boulogne, F.; Um, E.; Jacobi, I.; Button, E.; Stone, H. A., Controlled Uniform Coating from the Interplay of Marangoni Flows and Surface-Adsorbed Macromolecules. *Physical Review Letters* **2016**, 116 (12), 124501.
84. Park, J.; Moon, J., Control of Colloidal Particle Deposit Patterns within Picoliter Droplets Ejected by Ink-Jet Printing. *Langmuir* **2006**, 22 (8), 3506-3513.

85. Manos, A.; Damien, B., Dynamic Photocontrol of the Coffee-Ring Effect with Optically Tunable Particle Stickiness. *Angewandte Chemie International Edition* **2014**, *53* (51), 14077-14081.
86. Kim, D.-O.; Pack, M.; Hu, H.; Kim, H.; Sun, Y., Deposition of Colloidal Drops Containing Ellipsoidal Particles: Competition between Capillary and Hydrodynamic Forces. *Langmuir* **2016**, *32* (45), 11899-11906.
87. Kim, S.-H.; Lee, S. Y.; Yang, S.-M.; Yi, G.-R., Self-assembled colloidal structures for photonics. *Npg Asia Materials* **2011**, *3*, 25.
88. Galisteo-López, J. F.; Ibisate, M.; Sapienza, R.; Froufe-Pérez, L. S.; Blanco, Á.; López, C., Self-Assembled Photonic Structures. *Advanced Materials* **2011**, *23* (1), 30-69.
89. (a) Stavenga, D. G., Thin Film and Multilayer Optics Cause Structural Colors of Many Insects and Birds. *Materials Today: Proceedings* **2014**, *1*, 109-121; (b) Jacobs, M.; Lopez-Garcia, M.; Phrathep, O. P.; Lawson, T.; Oulton, R.; Whitney, H. M., Photonic multilayer structure of Begonia chloroplasts enhances photosynthetic efficiency. **2016**, *2*, 16162; (c) Xiao, M.; Li, Y.; Allen, M. C.; Deheyn, D. D.; Yue, X.; Zhao, J.; Gianneschi, N. C.; Shawkey, M. D.; Dhinojwala, A., Bio-Inspired Structural Colors Produced via Self-Assembly of Synthetic Melanin Nanoparticles. *ACS Nano* **2015**, *9* (5), 5454-5460; (d) Whitney, Heather M.; Reed, A.; Rands, Sean A.; Chittka, L.; Glover, Beverley J., Flower Iridescence Increases Object Detection in the Insect Visual System without Compromising Object Identity. *Current Biology* **26** (6), 802-808; (e) Rodríguez, R. E.; Agarwal, S. P.; An, S.; Kazyak, E.; Das, D.; Shang, W.; Skye, R.; Deng, T.; Dasgupta, N. P., Biotemplated Morpho Butterfly Wings for Tunable Structurally Colored Photocatalysts. *ACS Appl. Mater. Interfaces* **2018**, *10* (5), 4614-4621.
90. Vukusic, P.; Sambles, J. R.; Lawrence, C. R.; Wootton, R. J., Quantified interference and diffraction in single Morpho butterfly scales. *Proceedings of the Royal Society of London. Series B: Biological Sciences* **1999**, *266* (1427), 1403-1411.
91. Dumanli, A. G.; Savin, T., Recent advances in the biomimicry of structural colours. *Chemical Society Reviews* **2016**, *45* (24), 6698-6724.
92. Kinoshita, S.; Yoshioka, S.; Miyazaki, J., Physics of structural colors. *Reports on Progress in Physics* **2008**, *71* (7), 076401.
93. Cary, A. T.; Yulan, F.; Anne-Martine, J.; Eugenii, U. D.; Rene, L., Reproduction and optical analysis of Morpho -inspired polymeric nanostructures. *Journal of Optics* **2016**, *18* (6), 065105.
94. Hooke, R.; Allestry, J.; Martyn, J., *Micrographia, or, Some physiological descriptions of minute bodies made by magnifying glasses :with observations and inquiries thereupon*. Printed by Jo. Martyn and Ja. Allestry, printers to the Royal Society ... London :, 1665.
95. Grant, T. E.; Joanna, A., Emerging optical properties from the combination of simple optical effects. *Reports on Progress in Physics* **2018**, *81* (1), 016402.
96. Freestone, I.; Meeks, N.; Sax, M.; Higgitt, C., The Lycurgus Cup — A Roman nanotechnology. *Gold Bulletin* **2007**, *40* (4), 270-277.
97. Link, S.; El-Sayed, M. A., Size and Temperature Dependence of the Plasmon Absorption of Colloidal Gold Nanoparticles. *The Journal of Physical Chemistry B* **1999**, *103* (21), 4212-4217.

98. Lee, K.-S.; El-Sayed, M. A., Gold and Silver Nanoparticles in Sensing and Imaging: Sensitivity of Plasmon Response to Size, Shape, and Metal Composition. *The Journal of Physical Chemistry B* **2006**, *110* (39), 19220-19225.
99. Kelly, K. L.; Coronado, E.; Zhao, L. L.; Schatz, G. C., The Optical Properties of Metal Nanoparticles: The Influence of Size, Shape, and Dielectric Environment. *The Journal of Physical Chemistry B* **2003**, *107* (3), 668-677.
100. Al-Hassan, A. Y., An Eighth Century Arabic Treatise On The Colouring Of Glass: Kitāb Al-Durra Al-Maknūna (The Book Of The Hidden Pearl) Of Jābir Ibn Hayyān (C. 721–C. 815). *Arabic Sciences and Philosophy* **2009**, *19* (1), 121-156.
101. Srinivasarao, M., Nano-Optics in the Biological World: Beetles, Butterflies, Birds, and Moths. *Chem. Rev.* **1999**, *99* (7), 1935-1962.
102. Sun, J.; Bhushan, B.; Tong, J., Structural coloration in nature. *RSC Advances* **2013**, *3* (35), 14862-14889.
103. Tao, L.; Wenhong, P.; Shenmin, Z.; Di, Z., Bio-inspired fabrication of stimuli-responsive photonic crystals with hierarchical structures and their applications. *Nanotechnology* **2016**, *27* (12), 122001.
104. Yacoubian, A., *Optics Essentials: An Interdisciplinary Guide*. CRC Press: 2014.
105. Tilley, R. J. D., Iridescence (Goniochromism). In *Encyclopedia of Color Science and Technology*, Luo, R., Ed. Springer New York: New York, NY, 2014; pp 1-10.
106. Yablonovitch, E.; Gmitter, T. J., Photonic band structure: The face-centered-cubic case. *Physical Review Letters* **1989**, *63* (18), 1950-1953.
107. Yablonovitch, E., Photonic Crystals: Towards Nanoscale Photonic Devices. American Institute of Physics: 2006; Vol. 59, pp 54-55.
108. von Freymann, G.; Kitaev, V.; Lotsch, B. V.; Ozin, G. A., Bottom-up assembly of photonic crystals. *Chemical Society Reviews* **2013**, *42* (7), 2528-2554.
109. Hou, J.; Li, M.; Song, Y., Patterned Colloidal Photonic Crystals. *Angewandte Chemie International Edition* **2017**, (56), 2-12.
110. Vignolini, S.; Rudall, P. J.; Rowland, A. V.; Reed, A.; Moyroud, E.; Faden, R. B.; Baumberg, J. J.; Glover, B. J.; Steiner, U., Pointillist structural color in Pollia fruit. *Proceedings of the National Academy of Sciences* **2012**, *109* (39), 15712-15715.
111. Sharma, V.; Crne, M.; Park, J. O.; Srinivasarao, M., Structural Origin of Circularly Polarized Iridescence in Jeweled Beetles. *Science* **2009**, *325* (5939), 449-451.
112. Nickerson, R. F.; Habrle, J. A., Cellulose Intercrystalline Structure. *Industrial & Engineering Chemistry* **1947**, *39* (11), 1507-1512.
113. Marchessault, R. H.; Morehead, F. F.; Walter, N. M., Liquid Crystal Systems from Fibrillar Polysaccharides. *Nature* **1959**, *184*, 632.
114. Favier, V.; Chanzy, H.; Cavaille, J. Y., Polymer Nanocomposites Reinforced by Cellulose Whiskers. *Macromolecules* **1995**, *28* (18), 6365-6367.
115. Kontturi, E.; Laaksonen, P.; Linder, M. B.; Nonappa; Gröschel, A. H.; Rojas, O. J.; Ikkala, O., Advanced Materials through Assembly of Nanocelluloses. *Advanced Materials* **2018**, (30), 1703779.
116. Klemm, D.; Cranston, E. D.; Fischer, D.; Gama, M.; Kedzior, S. A.; Kralisch, D.; Kramer, F.; Kondo, T.; Lindström, T.; Nietzsche, S.; Petzold-Welcke, K.;

Rauchfuß, F., Nanocellulose as a natural source for groundbreaking applications in materials science: Today's state. *Materials Today* **2018**.

117. de Assis, C. A.; Houtman, C.; Phillips, R.; Bilek, E. M.; Rojas, O. J.; Pal, L.; Peresin, M. S.; Jameel, H.; Gonzalez, R., Conversion Economics of Forest Biomaterials: Risk and Financial Analysis of CNC Manufacturing. *Biofuels, Bioproducts and Biorefining* **2017**, *11* (4), 682-700.

118. Kovacs, T.; Naish, V.; O'Connor, B.; Blaise, C.; Gagné, F.; Hall, L.; Trudeau, V.; Martel, P., An ecotoxicological characterization of nanocrystalline cellulose (NCC). *Nanotoxicology* **2010**, *4* (3), 255-270.

119. Dong, S.; Hirani, A. A.; Colacino, K. R.; Lee, Y. W.; Roman, M., Cytotoxicity And Cellular Uptake Of Cellulose Nanocrystals. *Nano LIFE* **2012**, *02* (03), 1241006.

120. Seabra, A. B.; Bernardes, J. S.; Fávaro, W. J.; Paula, A. J.; Durán, N., Cellulose nanocrystals as carriers in medicine and their toxicities: A review. *Carbohydrate Polymers* **2018**, *181*, 514-527.

121. Camarero-Espinosa, S.; Endes, C.; Mueller, S.; Petri-Fink, A.; Rothen-Rutishauser, B.; Weder, C.; Clift, M.; Foster, E., Elucidating the Potential Biological Impact of Cellulose Nanocrystals. *Fibers* **2016**, *4* (3), 21.

122. Klemm, D.; Heublein, B.; Fink, H.-P.; Bohn, A., Cellulose: Fascinating Biopolymer and Sustainable Raw Material. *Angewandte Chemie International Edition* **2005**, *44* (22), 3358-3393.

123. Abitbol, T.; Rivkin, A.; Cao, Y.; Nevo, Y.; Abraham, E.; Ben-Shalom, T.; Lapidot, S.; Shoseyov, O., Nanocellulose, a tiny fiber with huge applications. *Current Opinion in Biotechnology* **2016**, *39*, 76-88.

124. Nelson, D.; Ana Paula, L.; Amedea, B. S., Review of Cellulose Nanocrystals Patents: Preparation, Composites and General Applications. *Recent Patents on Nanotechnology* **2012**, *6* (1), 16-28.

125. Trache, D.; Hussin, M. H.; Haafiz, M. K. M.; Thakur, V. K., Recent progress in cellulose nanocrystals: sources and production. *Nanoscale* **2017**, *9* (5), 1763-1786.

126. Kargarzadeh, H.; Ahmad, I.; Thomas, S.; Dufresne, A., *Handbook of Nanocellulose and Cellulose Nanocomposites, 2 Volume Set*. Wiley: 2017.

127. Hamad, W. Y., *Cellulose Nanocrystals: Properties, Production and Applications*. Wiley: 2017.

128. Habibi, Y.; Lucia, L. A.; Rojas, O. J., Cellulose nanocrystals: Chemistry, self-assembly, and applications. *Chem. Rev.* **2010**, *110* (6), 3479-3500.

129. Cheng, M.; Qin, Z.; Chen, Y.; Hu, S.; Ren, Z.; Zhu, M., Efficient Extraction of Cellulose Nanocrystals through Hydrochloric Acid Hydrolysis Catalyzed by Inorganic Chlorides under Hydrothermal Conditions. *ACS Sustainable Chemistry & Engineering* **2017**, *5* (6), 4656-4664.

130. Ehmman, H. M. A.; Mohan, T.; Koshanskaya, M.; Scheicher, S.; Breitwieser, D.; Ribitsch, V.; Stana-Kleinschek, K.; Spirk, S., Design of anticoagulant surfaces based on cellulose nanocrystals. *Chemical Communications* **2014**, *50* (86), 13070-13072.

131. Lu, P.; Hsieh, Y.-L., Preparation and properties of cellulose nanocrystals: Rods, spheres, and network. *Carbohydrate Polymers* **2010**, *82* (2), 329-336.

132. Puspasari, T.; Pradeep, N.; Peinemann, K.-V., Crosslinked cellulose thin film composite nanofiltration membranes with zero salt rejection. *Journal of Membrane Science* **2015**, *491*, 132-137.
133. Salas, C.; Nypelö, T.; Rodriguez-Abreu, C.; Carrillo, C.; Rojas, O. J., Nanocellulose properties and applications in colloids and interfaces. *Current Opinion in Colloid & Interface Science* **2014**, *19* (5), 383-396.
134. Beck-Candanedo, S.; Roman, M.; Gray, D. G., Effect of Reaction Conditions on the Properties and Behavior of Wood Cellulose Nanocrystal Suspensions. *Biomacromolecules* **2005**, *6* (2), 1048-1054.
135. Oksman, K.; Aitomäki, Y.; Mathew, A. P.; Siqueira, G.; Zhou, Q.; Butylina, S.; Tanpichai, S.; Zhou, X.; Hooshmand, S., Review of the recent developments in cellulose nanocomposite processing. *Composites Part A: Applied Science and Manufacturing* **2016**, *83*, 2-18.
136. Eyley, S.; Thielemans, W., Surface modification of cellulose nanocrystals. *Nanoscale* **2014**, *6* (14), 7764-7779.
137. Natarajan, B.; Gilman, J. W., Bioinspired Bouligand cellulose nanocrystal composites: a review of mechanical properties. *Philosophical Transactions of the Royal Society A: Mathematical, Physical and Engineering Sciences* **2018**, *376* (2112).
138. Bondeson, D.; Oksman, K., Dispersion and characteristics of surfactant modified cellulose whiskers nanocomposites. *Composite Interfaces* **2007**, *14* (7-9), 617-630.
139. Siqueira, G.; Bras, J.; Dufresne, A., Cellulosic Bionanocomposites: A Review of Preparation, Properties and Applications. *Polymers* **2010**, *2* (4), 728.
140. Stinson-Bagby, K. L.; Roberts, R.; Foster, E. J., Effective cellulose nanocrystal imaging using transmission electron microscopy. *Carbohydrate Polymers* **2018**, *186*, 429-438.
141. Lahiji, R. R.; Xu, X.; Reifenberger, R.; Raman, A.; Rudie, A.; Moon, R. J., Atomic Force Microscopy Characterization of Cellulose Nanocrystals. *Langmuir* **2010**, *26* (6), 4480-4488.
142. Brinkmann, A.; Chen, M.; Couillard, M.; Jakubek, Z. J.; Leng, T.; Johnston, L. J., Correlating Cellulose Nanocrystal Particle Size and Surface Area. *Langmuir* **2016**, *32* (24), 6105-6114.
143. Jakubek, Z. J.; Chen, M.; Couillard, M.; Leng, T.; Liu, L.; Zou, S.; Baxa, U.; Clogston, J. D.; Hamad, W. Y.; Johnston, L. J., Characterization challenges for a cellulose nanocrystal reference material: dispersion and particle size distributions. *J Nanopart Res* **2018**, *20* (4), 98.
144. Elazzouzi-Hafraoui, S.; Nishiyama, Y.; Putaux, J.-L.; Heux, L.; Dubreuil, F.; Rochas, C., The Shape and Size Distribution of Crystalline Nanoparticles Prepared by Acid Hydrolysis of Native Cellulose. *Biomacromolecules* **2008**, *9* (1), 57-65.
145. Reid, M. S.; Villalobos, M.; Cranston, E. D., Benchmarking Cellulose Nanocrystals: From the Laboratory to Industrial Production. *Langmuir* **2017**, *33* (7), 1583-1598.
146. Foster, E. J.; Moon, R. J.; Agarwal, U. P.; Bortner, M. J.; Bras, J.; Camarero-Espinosa, S.; Chan, K. J.; Clift, M. J. D.; Cranston, E. D.; Eichhorn, S. J.; Fox, D. M.; Hamad, W. Y.; Heux, L.; Jean, B.; Korey, M.; Nieh, W.; Ong, K. J.; Reid, M. S.; Renneckar, S.; Roberts, R.; Shatkin, J. A.; Simonsen, J.; Stinson-Bagby, K.

- Wanasekara, N.; Youngblood, J., Current characterization methods for cellulose nanomaterials. *Chemical Society Reviews* **2018**, *47* (8), 2609-2679.
147. Mao, Y.; Liu, K.; Zhan, C.; Geng, L.; Chu, B.; Hsiao, B. S., Characterization of Nanocellulose Using Small-Angle Neutron, X-ray, and Dynamic Light Scattering Techniques. *The Journal of Physical Chemistry B* **2017**, *121* (6), 1340-1351.
 148. Ehmman, H. M. A.; Spirk, S.; Doliška, A.; Mohan, T.; Gössler, W.; Ribitsch, V.; Sfiligoj-Smole, M.; Stana-Kleinschek, K., Generalized Indirect Fourier Transformation as a Valuable Tool for the Structural Characterization of Aqueous Nanocrystalline Cellulose Suspensions by Small Angle X-ray Scattering. *Langmuir* **2013**, *29* (11), 3740-3748.
 149. Su, Y.; Burger, C.; Ma, H.; Chu, B.; Hsiao, B. S., Exploring the Nature of Cellulose Microfibrils. *Biomacromolecules* **2015**, *16* (4), 1201-1209.
 150. Zugenmaier, P., Conformation and packing of various crystalline cellulose fibers. *Progress in Polymer Science* **2001**, *26* (9), 1341-1417.
 151. Nishiyama, Y.; Sugiyama, J.; Chanzy, H.; Langan, P., Crystal Structure and Hydrogen Bonding System in Cellulose Ia from Synchrotron X-ray and Neutron Fiber Diffraction. *Journal of the American Chemical Society* **2003**, *125* (47), 14300-14306.
 152. Yue, Y.; Zhou, C.; French, A. D.; Xia, G.; Han, G.; Wang, Q.; Wu, Q., Comparative properties of cellulose nano-crystals from native and mercerized cotton fibers. *Cellulose* **2012**, *19* (4), 1173-1187.
 153. Zugenmaier, P., *Crystalline Cellulose and Derivatives: Characterization and Structures*. Springer Berlin Heidelberg: 2008.
 154. Thygesen, A.; Oddershede, J.; Lilholt, H.; Thomsen, A. B.; Ståhl, K., On the determination of crystallinity and cellulose content in plant fibres. *Cellulose* **2005**, *12* (6), 563.
 155. Dufresne, A., *Nanocellulose: From Nature to High Performance Tailored Materials*. De Gruyter: 2013.
 156. Abitbol, T.; Kam, D.; Levi-Kalishman, Y.; Gray, D. G.; Shoseyov, O., Surface Charge Influence on the Phase Separation and Viscosity of Cellulose Nanocrystals. *Langmuir* **2018**, *34* (13), 3925-3933.
 157. Lombardo, S.; Eyley, S.; Schütz, C.; van Gorp, H.; Rosenfeldt, S.; Van den Mooter, G.; Thielemans, W., Thermodynamic Study of the Interaction of Bovine Serum Albumin and Amino Acids with Cellulose Nanocrystals. *Langmuir* **2017**, *33* (22), 5473-5481.
 158. Schütz, C.; Van Rie, J.; Eyley, S.; Genç, A.; van Gorp, H.; Rosenfeldt, S.; Kang, K.; Thielemans, W., Effect of Source on the Properties and Behavior of Cellulose Nanocrystal Suspensions. *ACS Sustainable Chemistry & Engineering* **2018**, *6* (7), 8317-8324.
 159. Sacui, I. A.; Nieuwendaal, R. C.; Burnett, D. J.; Stranick, S. J.; Jorfi, M.; Weder, C.; Foster, E. J.; Olsson, R. T.; Gilman, J. W., Comparison of the Properties of Cellulose Nanocrystals and Cellulose Nanofibrils Isolated from Bacteria, Tunicate, and Wood Processed Using Acid, Enzymatic, Mechanical, and Oxidative Methods. *ACS Appl. Mater. Interfaces* **2014**, *6* (9), 6127-6138.
 160. Li, M.-C.; Wu, Q.; Song, K.; Lee, S.; Qing, Y.; Wu, Y., Cellulose Nanoparticles: Structure–Morphology–Rheology Relationships. *ACS Sustainable Chemistry & Engineering* **2015**, *3* (5), 821-832.

161. Moberg, T.; Sahlin, K.; Yao, K.; Geng, S.; Westman, G.; Zhou, Q.; Oksman, K.; Rigdahl, M., Rheological properties of nanocellulose suspensions: effects of fibril/particle dimensions and surface characteristics. *Cellulose* **2017**, *24* (6), 2499-2510.
162. Korolovych, V. F.; Cherpak, V.; Nepal, D.; Ng, A.; Shaikh, N. R.; Grant, A.; Xiong, R.; Bunning, T. J.; Tsukruk, V. V., Cellulose nanocrystals with different morphologies and chiral properties. *Polymer* **2018**, *145*, 334-347.
163. Ureña-Benavides, E. E.; Ao, G.; Davis, V. A.; Kitchens, C. L., Rheology and Phase Behavior of Lyotropic Cellulose Nanocrystal Suspensions. *Macromolecules* **2011**, *44* (22), 8990-8998.
164. Xu, X.; Rice, S. A.; Dinner, A. R., Relation between ordering and shear thinning in colloidal suspensions. *Proceedings of the National Academy of Sciences* **2013**, *110* (10), 3771-3776.
165. Shafiei-Sabet, S.; Hamad, W. Y.; Hatzikiriakos, S. G., Rheology of Nanocrystalline Cellulose Aqueous Suspensions. *Langmuir* **2012**, *28* (49), 17124-17133.
166. Gu, M.; Jiang, C.; Liu, D.; Prempeh, N.; Smalyukh, I. I., Cellulose Nanocrystal/Poly(ethylene glycol) Composite as an Iridescent Coating on Polymer Substrates: Structure-Color and Interface Adhesion. *ACS Appl. Mater. Interfaces* **2016**, *8* (47), 32565-32573.
167. Wang, B.; Walther, A., Self-Assembled, Iridescent, Crustacean-Mimetic Nanocomposites with Tailored Periodicity and Layered Cuticular Structure. *ACS Nano* **2015**, *9* (11), 10637-10646.
168. Bardet, R.; Belgacem, N.; Bras, J., Flexibility and Color Monitoring of Cellulose Nanocrystal Iridescent Solid Films Using Anionic or Neutral Polymers. *ACS Appl. Mater. Interfaces* **2015**, *7* (7), 4010-4018.
169. Yao, K.; Meng, Q.; Bulone, V.; Zhou, Q., Flexible and Responsive Chiral Nematic Cellulose Nanocrystal/Poly(ethylene glycol) Composite Films with Uniform and Tunable Structural Color. *Advanced Materials* **2017**, 1701323.
170. Araki, J.; Kuga, S., Effect of Trace Electrolyte on Liquid Crystal Type of Cellulose Microcrystals. *Langmuir* **2001**, *17* (15), 4493-4496.
171. Pan, J.; Hamad, W.; Straus, S. K., Parameters Affecting the Chiral Nematic Phase of Nanocrystalline Cellulose Films. *Macromolecules* **2010**, *43* (8), 3851-3858.
172. Oguzlu, H.; Danumah, C.; Boluk, Y., Colloidal behavior of aqueous cellulose nanocrystal suspensions. *Curr. Opin. Colloid Interface Sci.* **2017**, *29*, 46-56.
173. Cherhal, F.; Cousin, F.; Capron, I., Influence of Charge Density and Ionic Strength on the Aggregation Process of Cellulose Nanocrystals in Aqueous Suspension, as Revealed by Small-Angle Neutron Scattering. *Langmuir* **2015**, *31* (20), 5596-5602.
174. Peddireddy, K. R.; Capron, I.; Nicolai, T.; Benyahia, L., Gelation Kinetics and Network Structure of Cellulose Nanocrystals in Aqueous Solution. *Biomacromolecules* **2016**, *17* (10), 3298-3304.
175. Bertsch, P.; Isabetini, S.; Fischer, P., Ion-Induced Hydrogel Formation and Nematic Ordering of Nanocrystalline Cellulose Suspensions. *Biomacromolecules* **2017**, *18* (12), 4060-4066.

176. Dong, X. M.; Kimura, T.; Revol, J.-F.; Gray, D. G., Effects of Ionic Strength on the Isotropic–Chiral Nematic Phase Transition of Suspensions of Cellulose Crystallites. *Langmuir* **1996**, *12* (8), 2076-2082.
177. Lyubimova, O.; Stoyanov, S. R.; Gusarov, S.; Kovalenko, A., Electric Interfacial Layer of Modified Cellulose Nanocrystals in Aqueous Electrolyte Solution: Predictions by the Molecular Theory of Solvation. *Langmuir* **2015**, *31* (25), 7106-7116.
178. Chau, M.; Sriskandha, S. E.; Pichugin, D.; Thérien-Aubin, H.; Nykypanchuk, D.; Chauve, G.; Méthot, M.; Bouchard, J.; Gang, O.; Kumacheva, E., Ion-Mediated Gelation of Aqueous Suspensions of Cellulose Nanocrystals. *Biomacromolecules* **2015**, *16* (8), 2455-2462.
179. De France, K. J.; Hoare, T.; Cranston, E. D., Review of Hydrogels and Aerogels Containing Nanocellulose. *Chem. Mater.* **2017**, *29* (11), 4609-4631.
180. Phan-Xuan, T.; Thuresson, A.; Skepö, M.; Labrador, A.; Bordes, R.; Matic, A., Aggregation behavior of aqueous cellulose nanocrystals: the effect of inorganic salts. *Cellulose* **2016**, *23* (6), 3653-3663.
181. Cherhal, F.; Cousin, F.; Capron, I., Structural Description of the Interface of Pickering Emulsions Stabilized by Cellulose Nanocrystals. *Biomacromolecules* **2016**, *17* (2), 496-502.
182. Kalashnikova, I.; Bizot, H.; Cathala, B.; Capron, I., Modulation of Cellulose Nanocrystals Amphiphilic Properties to Stabilize Oil/Water Interface. *Biomacromolecules* **2012**, *13* (1), 267-275.
183. Pickering, S. U., CXCVI.-Emulsions. *Journal of the Chemical Society, Transactions* **1907**, *91* (0), 2001-2021.
184. Aveyard, R.; Beake, B. D.; Clint, J. H., Wettability of spherical particles at liquid surfaces. *Journal of the Chemical Society, Faraday Transactions* **1996**, *92* (21), 4271-4277.
185. Capron, I.; Rojas, O. J.; Bordes, R., Behavior of nanocelluloses at interfaces. *Current Opinion in Colloid & Interface Science* **2017**, *29*, 83-95.
186. Giese, M.; Blusch, L. K.; Khan, M. K.; MacLachlan, M. J., Functional Materials from Cellulose-Derived Liquid-Crystal Templates. *Angewandte Chemie International Edition* **2015**, *54* (10), 2888-2910.
187. Wayne, R., Interference Microscopy. In *Light and Video Microscopy*, Academic Press/Elsevier: 2009; pp 149-166.
188. Wang, P.-X.; Hamad, W. Y.; MacLachlan, M. J., Structure and transformation of tactoids in cellulose nanocrystal suspensions. *Nat. Commun.* **2016**, *7*.
189. De, V., Rotatory power and other optical properties of certain liquid crystals. *Acta Crystallographica* **1951**, *4* (3), 219-226.
190. Thanh-Dinh, N.; Egoitz, S.; Harkaitz, E.; Erlantz, L., Iridescent cellulose nanocrystal films: the link between structural colour and Bragg's law. *European Journal of Physics* **2018**, *39* (4), 045803.
191. Gray, D., Recent Advances in Chiral Nematic Structure and Iridescent Color of Cellulose Nanocrystal Films. *Nanomaterials* **2016**, *6* (11), 213.
192. Straley, J. P., Theory of piezoelectricity in nematic liquid crystals, and of the cholesteric ordering. *Physical Review A* **1976**, *14* (5), 1835-1841.

193. Dogic, Z.; Fraden, S., Cholesteric Phase in Virus Suspensions. *Langmuir* **2000**, *16* (20), 7820-7824.
194. Khoo, I. C., *Liquid Crystals*. Wiley: 2007.
195. Majoinen, J.; Kontturi, E.; Ikkala, O.; Gray, D. G., SEM imaging of chiral nematic films cast from cellulose nanocrystal suspensions. *Cellulose* **2012**, *19* (5), 1599-1605.
196. Almeida, A. P. C.; Canejo, J. P.; Fernandes, S. N.; Echeverria, C.; Almeida, P. L.; Godinho, M. H., Cellulose-Based Biomimetics and Their Applications. *Advanced Materials* **2018**, 1703655.
197. De France, K. J.; Yager, K. G.; Hoare, T.; Cranston, E. D., Cooperative Ordering and Kinetics of Cellulose Nanocrystal Alignment in a Magnetic Field. *Langmuir* **2016**, *32* (30), 7564-7571.
198. Frka-Petesic, B.; Radavidson, H.; Jean, B.; Heux, L., Dynamically Controlled Iridescence of Cholesteric Cellulose Nanocrystal Suspensions Using Electric Fields. *Advanced Materials* **2017**, *29* (11), 1606208.
199. Frka-Petesic, B.; Guidetti, G.; Kamita, G.; Vignolini, S., Controlling the Photonic Properties of Cholesteric Cellulose Nanocrystal Films with Magnets. *Advanced Materials* **2017**, *29* (32), 1701469.
200. Diaz, J. A.; Wu, X.; Martini, A.; Youngblood, J. P.; Moon, R. J., Thermal Expansion of Self-Organized and Shear-Oriented Cellulose Nanocrystal Films. *Biomacromolecules* **2013**, *14* (8), 2900-2908.
201. Frka-Petesic, B.; Sugiyama, J.; Kimura, S.; Chanzy, H.; Maret, G., Negative Diamagnetic Anisotropy and Birefringence of Cellulose Nanocrystals. *Macromolecules* **2015**, *48* (24), 8844-8857.
202. Sanchez-Botero, L.; Dimov, A. V.; Li, R.; Smilgies, D.-M.; Hinestroza, J. P., In Situ and Real-Time Studies, via Synchrotron X-ray Scattering, of the Orientational Order of Cellulose Nanocrystals during Solution Shearing. *Langmuir* **2018**, *34* (18), 5263-5272.
203. Beck, S.; Bouchard, J.; Berry, R., Controlling the Reflection Wavelength of Iridescent Solid Films of Nanocrystalline Cellulose. *Biomacromolecules* **2011**, *12* (1), 167-172.
204. Liu, D.; Wang, S.; Ma, Z.; Tian, D.; Gu, M.; Lin, F., Structure-color mechanism of iridescent cellulose nanocrystal films. *RSC Advances* **2014**, *4* (74), 39322-39331.
205. Giese, M.; Khan, M. K.; Hamad, W. Y.; MacLachlan, M. J., Imprinting of Photonic Patterns with Thermosetting Amino-Formaldehyde-Cellulose Composites. *ACS Macro Letters* **2013**, *2* (9), 818-821.
206. Wan, H.; Li, X.; Zhang, L.; Li, X.; Liu, P.; Jiang, Z.; Yu, Z.-Z., Rapidly Responsive and Flexible Chiral Nematic Cellulose Nanocrystal Composites as Multifunctional Rewritable Photonic Papers with Eco-Friendly Inks. *ACS Appl. Mater. Interfaces* **2018**.
207. He, Y.-D.; Zhang, Z.-L.; Xue, J.; Wang, X.-H.; Song, F.; Wang, X.-L.; Zhu, L.-L.; Wang, Y.-Z., Biomimetic Optical Cellulose Nanocrystal Films with Controllable Iridescent Color and Environmental Stimuli-Responsive Chromism. *ACS Appl. Mater. Interfaces* **2018**.

208. Yao, K.; Meng, Q.; Bulone, V.; Zhou, Q., Flexible and Responsive Chiral Nematic Cellulose Nanocrystal/Poly(ethylene glycol) Composite Films with Uniform and Tunable Structural Color. *Advanced Materials* **2017**, *29* (28), 1701323.
209. Lukach, A.; Thérien-Aubin, H.; Querejeta-Fernández, A.; Pitch, N.; Chauve, G.; Méthot, M.; Bouchard, J.; Kumacheva, E., Coassembly of Gold Nanoparticles and Cellulose Nanocrystals in Composite Films. *Langmuir* **2015**, *31* (18), 5033-5041.
210. Querejeta-Fernández, A.; Kopera, B.; Prado, K. S.; Klinkova, A.; Methot, M.; Chauve, G.; Bouchard, J.; Helmy, A. S.; Kumacheva, E., Circular Dichroism of Chiral Nematic Films of Cellulose Nanocrystals Loaded with Plasmonic Nanoparticles. *ACS Nano* **2015**, *9* (10), 10377-10385.
211. Liu, H.; Song, J.; Shang, S.; Song, Z.; Wang, D., Cellulose Nanocrystal/Silver Nanoparticle Composites as Bifunctional Nanofillers within Waterborne Polyurethane. *ACS Appl. Mater. Interfaces* **2012**, *4* (5), 2413-2419.
212. Querejeta-Fernández, A.; Chauve, G.; Methot, M.; Bouchard, J.; Kumacheva, E., Chiral Plasmonic Films Formed by Gold Nanorods and Cellulose Nanocrystals. *Journal of the American Chemical Society* **2014**, *136* (12), 4788-4793.
213. Liu, P.; Guo, X.; Nan, F.; Duan, Y.; Zhang, J., Modifying Mechanical, Optical Properties and Thermal Processability of Iridescent Cellulose Nanocrystal Films Using Ionic Liquid. *ACS Applied Materials & Interfaces* **2017**, *9* (3), 3085-3092.
214. Yang, D.; Lu, Z.; Qi, X.; Yan, D.; Gao, Q.; Zhan, D.; Jiang, Y.; Liu, X. Y., Fabrication of a uniaxial cellulose nanocrystal thin film for coassembly of single-walled carbon nanotubes. *RSC Advances* **2016**, *6* (45), 39396-39400.
215. Habibi, Y.; Hoeger, I.; Kelley, S. S.; Rojas, O. J., Development of Langmuir–Schaeffer Cellulose Nanocrystal Monolayers and Their Interfacial Behaviors. *Langmuir* **2010**, *26* (2), 990-1001.
216. Holmberg, M.; Berg, J.; Stemme, S.; Ödberg, L.; Rasmusson, J.; Claesson, P., Surface Force Studies of Langmuir–Blodgett Cellulose Films. *Journal of Colloid and Interface Science* **1997**, *186* (2), 369-381.
217. Podsiadlo, P.; Sui, L.; Elkasabi, Y.; Burgardt, P.; Lee, J.; Miryala, A.; Kusumaatmaja, W.; Carman, M. R.; Shtein, M.; Kieffer, J.; Lahann, J.; Kotov, N. A., Layer-by-Layer Assembled Films of Cellulose Nanowires with Antireflective Properties. *Langmuir* **2007**, *23* (15), 7901-7906.
218. Kontturi, E.; Johansson, L.-S.; Kontturi, K. S.; Ahonen, P.; Thüne, P. C.; Laine, J., Cellulose Nanocrystal Submonolayers by Spin Coating. *Langmuir* **2007**, *23* (19), 9674-9680.
219. Notley, S. M.; Eriksson, M.; Wågberg, L.; Beck, S.; Gray, D. G., Surface Forces Measurements of Spin-Coated Cellulose Thin Films with Different Crystallinity. *Langmuir* **2006**, *22* (7), 3154-3160.
220. Cranston, E. D.; Gray, D. G., Birefringence in spin-coated films containing cellulose nanocrystals. *Colloids and Surfaces A: Physicochemical and Engineering Aspects* **2008**, *325* (1), 44-51.
221. Mu, X.; Gray, D., Droplets of cellulose nanocrystal suspensions on drying give iridescent 3-D “coffee-stain” rings. *Cellulose* **2015**, *22* (2), 1103-1107.

222. Gençer, A.; Schütz, C.; Thielemans, W., Influence of the Particle Concentration and Marangoni Flow on the Formation of Cellulose Nanocrystal Films. *Langmuir* **2017**, *33* (1), 228-234.
223. Edgar, C.; Gray, D., Smooth model cellulose I surfaces from nanocrystal suspensions. *Cellulose* **2003**, *10* (4), 299-306.
224. Hoeger, I.; Rojas, O. J.; Efimenko, K.; Velev, O. D.; Kelley, S. S., Ultrathin film coatings of aligned cellulose nanocrystals from a convective-shear assembly system and their surface mechanical properties. *Soft Matter* **2011**, *7* (5), 1957-1967.
225. Alizadehgiashi, M.; Khabibullin, A.; Li, Y.; Prince, E.; Abolhasani, M.; Kumacheva, E., Shear-Induced Alignment of Anisotropic Nanoparticles in a Single-Droplet Oscillatory Microfluidic Platform. *Langmuir* **2018**, *34* (1), 322-330.
226. Vollick, B.; Kuo, P.-Y.; Alizadehgiashi, M.; Yan, N.; Kumacheva, E., From Structure to Properties of Composite Films Derived from Cellulose Nanocrystals. *ACS Omega* **2017**, *2* (9), 5928-5934.
227. Osorio-Madrado, A.; Eder, M.; Rueggeberg, M.; Pandey, J. K.; Harrington, M. J.; Nishiyama, Y.; Putaux, J.-L.; Rochas, C.; Burgert, I., Reorientation of Cellulose Nanowhiskers in Agarose Hydrogels under Tensile Loading. *Biomacromolecules* **2012**, *13* (3), 850-856.
228. Xu, H.-N.; Tang, Y.-Y.; Ouyang, X.-K., Shear-Induced Breakup of Cellulose Nanocrystal Aggregates. *Langmuir* **2017**, *33* (1), 235-242.
229. Le, E. A.; Wang, W. C.; Liu, C. S.; Wang, C. W. In *Effect of Fiber Alignment on Optical Properties of Cellulose Nanocrystal Films*, 2014 International Symposium on Optomechatronic Technologies, 5-7 Nov. 2014; 2014; pp 305-309.
230. Kontturi, E.; Österberg, M., Cellulose Model Films: Challenges in Preparation. In *Model Cellulosic Surfaces*, American Chemical Society: 2009; Vol. 1019, pp 57-74.
231. Prathapan, R.; Berry, J. D.; Fery, A.; Garnier, G.; Tabor, R. F., Decreasing the Wettability of Cellulose Nanocrystal Surfaces Using Wrinkle-Based Alignment. *ACS Appl. Mater. Interfaces* **2017**, *9* (17), 15202-15211.
232. Nyström, G.; Fall, A. B.; Carlsson, L.; Wågberg, L., Aligned cellulose nanocrystals and directed nanoscale deposition of colloidal spheres. *Cellulose* **2014**, *21* (3), 1591-1599.
233. Pazos-Perez, N.; Ni, W.; Schweikart, A.; Alvarez-Puebla, R. A.; Fery, A.; Liz-Marzan, L. M., Highly uniform SERS substrates formed by wrinkle-confined drying of gold colloids. *Chemical Science* **2010**, *1* (2), 174-178.
234. Cataldi, U.; Caputo, R.; Kurylyak, Y.; Klein, G.; Chekini, M.; Umeton, C.; Burgi, T., Growing gold nanoparticles on a flexible substrate to enable simple mechanical control of their plasmonic coupling. *Journal of Materials Chemistry C* **2014**, *2* (37), 7927-7933.
235. Saha, P.; Davis, V. A., Photonic Properties and Applications of Cellulose Nanocrystal Films with Planar Anchoring. *ACS Applied Nano Materials* **2018**, *1* (5), 2175-2183.
236. Tardy, B. L.; Ago, M.; Guo, J.; Borghei, M.; Kämäräinen, T.; Rojas, O. J., Optical Properties of Self-Assembled Cellulose Nanocrystals Films Suspended at Planar-Symmetrical Interfaces. *Small* **2017**, *13* (47), 1702084.

237. Chakkresit, C.; Diethelm, J., An anisotropic ink based on crystalline nanocellulose: Potential applications in security printing. *Journal of Applied Polymer Science* **2014**, *131* (22).
238. K., K. M.; Anas, B.; Konrad, W.; Y., H. W.; J., M. M., Photonic Patterns Printed in Chiral Nematic Mesoporous Resins. *Angewandte Chemie International Edition* **2015**, *54* (14), 4304-4308.
239. Shopsowitz, K. E.; Qi, H.; Hamad, W. Y.; MacLachlan, M. J., Free-standing mesoporous silica films with tunable chiral nematic structures. *Nature* **2010**, *468*, 422.
240. Kelly, J. A.; Shukaliak, A. M.; Cheung, C. C. Y.; Shopsowitz, K. E.; Hamad, W. Y.; MacLachlan, M. J., Responsive Photonic Hydrogels Based on Nanocrystalline Cellulose. *Angewandte Chemie International Edition* **2013**, *52* (34), 8912-8916.
241. Zhang, Y. P.; Chodavarapu, V. P.; Kirk, A. G.; Andrews, M. P., Structured color humidity indicator from reversible pitch tuning in self-assembled nanocrystalline cellulose films. *Sensors and Actuators B: Chemical* **2013**, *176*, 692-697.
242. Domingues, R. M. A.; Gomes, M. E.; Reis, R. L., The Potential of Cellulose Nanocrystals in Tissue Engineering Strategies. *Biomacromolecules* **2014**, *15* (7), 2327-2346.
243. Song, W.; Lee, J.-K.; Gong, M. S.; Heo, K.; Chung, W.-J.; Lee, B. Y., Cellulose Nanocrystal-Based Colored Thin Films for Colorimetric Detection of Aldehyde Gases. *ACS Applied Materials & Interfaces* **2018**, *10* (12), 10353-10361.
244. Siqueira, G.; Kokkinis, D.; Libanori, R.; Hausmann, M. K.; Gladman, A. S.; Neels, A.; Tingaut, P.; Zimmermann, T.; Lewis, J. A.; Studart, A. R., Cellulose Nanocrystal Inks for 3D Printing of Textured Cellular Architectures. *Adv. Funct. Mater.* **2017**, *27* (12), 1604619.
245. Palaganas, N. B.; Mangadlao, J. D.; de Leon, A. C. C.; Palaganas, J. O.; Pangilinan, K. D.; Lee, Y. J.; Advincula, R. C., 3D Printing of Photocurable Cellulose Nanocrystal Composite for Fabrication of Complex Architectures via Stereolithography. *ACS Appl. Mater. Interfaces* **2017**, *9* (39), 34314-34324.
246. Li, V. C.-F.; Dunn, C. K.; Zhang, Z.; Deng, Y.; Qi, H. J., Direct Ink Write (DIW) 3D Printed Cellulose Nanocrystal Aerogel Structures. *Sci. Rep.* **2017**, *7* (1), 8018.
247. Hoeng, F.; Denneulin, A.; Bras, J., Use of nanocellulose in printed electronics: a review. *Nanoscale* **2016**, *8* (27), 13131-13154.
248. Nishiyama, Y.; Langan, P.; Chanzy, H., Crystal Structure and Hydrogen-Bonding System in Cellulose I β from Synchrotron X-ray and Neutron Fiber Diffraction. *Journal of the American Chemical Society* **2002**, *124* (31), 9074-9082.
249. Thygesen, A.; Oddershede, J.; Lilholt, H.; Thomsen, A. B.; Ståhl, K., On the determination of crystallinity and cellulose content in plant fibres. *Cellulose* **2005**, *12* (6), 563-576.
250. Nam, S.; French, A. D.; Condon, B. D.; Concha, M., Segal crystallinity index revisited by the simulation of X-ray diffraction patterns of cotton cellulose I β and cellulose II. *Carbohydrate Polymers* **2016**, *135*, 1-9.
251. Ahvenainen, P.; Kontro, I.; Svedström, K., Comparison of sample crystallinity determination methods by X-ray diffraction for challenging cellulose I materials. *Cellulose* **2016**, *23* (2), 1073-1086.

252. Winston, P. W.; Bates, D. H., Saturated Solutions For the Control of Humidity in Biological Research. *Ecology* **1960**, *41* (1), 232-237.
253. Wang, H.; Fang, J.; Cheng, T.; Ding, J.; Qu, L.; Dai, L.; Wang, X.; Lin, T., One-step coating of fluoro-containing silica nanoparticles for universal generation of surface superhydrophobicity. *Chemical Communications* **2008**, (7), 877-879.
254. Lamour, G.; Hamraoui, A.; Buvailo, A.; Xing, Y.; Keuleyan, S.; Prakash, V.; Eftekhari-Bafrooei, A.; Borguet, E., Contact Angle Measurements Using a Simplified Experimental Setup. *Journal of Chemical Education* **2010**, *87* (12), 1403-1407.
255. Stalder, A. F.; Kulik, G.; Sage, D.; Barbieri, L.; Hoffmann, P., A snake-based approach to accurate determination of both contact points and contact angles. *Colloids and Surfaces A: Physicochemical and Engineering Aspects* **2006**, *286* (1-3), 92-103.
256. Harris, J. W.; Stöcker, H., *Handbook of Mathematics and Computational Science*. Springer New York: 1998.
257. Dong-Hyeok, L.; Nahm-Gyoo, C., Assessment of surface profile data acquired by a stylus profilometer. *Measurement Science and Technology* **2012**, *23* (10), 105601.
258. Berry, J. D.; Neeson, M. J.; Dagastine, R. R.; Chan, D. Y. C.; Tabor, R. F., Measurement of surface and interfacial tension using pendant drop tensiometry. *J. Colloid Interface Sci.* **2015**, *454*, 226-237.
259. Lenfant, G.; Heuzey, M.-C.; van de Ven, T. G. M.; Carreau, P. J., A comparative study of ECNC and CNC suspensions: effect of salt on rheological properties. *Rheol. Acta* **2017**, *56* (1), 51-62.
260. Dhont, J. K. G., *An Introduction to Dynamics of Colloids*. Elsevier Science: 1996.
261. De Souza Lima, M. M.; Wong, J. T.; Paillet, M.; Borsali, R.; Pecora, R., Translational and Rotational Dynamics of Rodlike Cellulose Whiskers. *Langmuir* **2003**, *19* (1), 24-29.
262. Hassan, P. A.; Rana, S.; Verma, G., Making Sense of Brownian Motion: Colloid Characterization by Dynamic Light Scattering. *Langmuir* **2015**, *31* (1), 3-12.
263. Lehner, D.; Lindner, H.; Glatter, O., Determination of the Translational and Rotational Diffusion Coefficients of Rodlike Particles Using Depolarized Dynamic Light Scattering. *Langmuir* **2000**, *16* (4), 1689-1695.
264. Clogston, J.; Patri, A., Zeta Potential Measurement. In *Characterization of Nanoparticles Intended for Drug Delivery*, McNeil, S. E., Ed. Humana Press: 2011; Vol. 697, pp 63-70.
265. Tscharnuter, W. W., Mobility measurements by phase analysis. *Appl. Opt.* **2001**, *40* (24), 3995-4003.
266. Prathapan, R.; Thapa, R.; Garnier, G.; Tabor, R. F., Modulating the zeta potential of cellulose nanocrystals using salts and surfactants. *Colloids and Surfaces A: Physicochemical and Engineering Aspects* **2016**, *509*, 11-18.
267. Miller, J. F.; Schätzel, K.; Vincent, B., The determination of very small electrophoretic mobilities in polar and nonpolar colloidal dispersions using phase analysis light scattering. *Journal of Colloid and Interface Science* **1991**, *143* (2), 532-554.

268. Wyman, J., The dielectric constant of mixtures of ethyl alcohol and water from -5°C to 40°C. *Journal of the American Chemical Society* **1931**, 53 (9), 3292-3301.
269. Bhattacharjee, S., DLS and zeta potential – What they are and what they are not? *Journal of Controlled Release* **2016**, 235, 337-351.
270. Bakker, H. E.; Besseling, T. H.; Wijnhoven, J. E. G. J.; Helfferich, P. H.; van Blaaderen, A.; Imhof, A., Microelectrophoresis of Silica Rods Using Confocal Microscopy. *Langmuir* **2017**, 33 (4), 881-890.
271. Ohshima, H., Henry's Function for Electrophoresis of a Cylindrical Colloidal Particle. *Journal of Colloid and Interface Science* **1996**, 180 (1), 299-301.
272. Okuzono, T.; Kobayashi, M.; Doi, M., Final shape of a drying thin film. *Phys. Rev. E: Stat., Nonlinear, Soft Matter Phys.* **2009**, 80 (2), 021603.
273. Demus, D.; Goodby, J. W.; Gray, G. W.; Spiess, H. W.; Vill, V., *Handbook of Liquid Crystals, 4 Volume Set*. Wiley: 1998.
274. Roman, M.; Gray, D. G., Parabolic Focal Conics in Self-Assembled Solid Films of Cellulose Nanocrystals. *Langmuir* **2005**, 21 (12), 5555-5561.
275. Chu, G.; Vilensky, R.; Vasilyev, G.; Martin, P.; Zhang, R.; Zussman, E., Structure Evolution and Drying Dynamics in Sliding Cholesteric Cellulose Nanocrystals. *The Journal of Physical Chemistry Letters* **2018**, 1845-1851.
276. Narayanan, S.; Wang, J.; Lin, X.-M., Dynamical Self-Assembly of Nanocrystal Superlattices during Colloidal Droplet Evaporation by in situ Small Angle X-Ray Scattering. *Physical Review Letters* **2004**, 93 (13), 135503.
277. Stoiber, R. E.; Morse, S. A., *Crystal Identification with the Polarizing Microscope*. Springer US: 2012.
278. Wayne, R. O., *Light and Video Microscopy*. Elsevier Science: 2010.
279. Stoiber, R. E.; Morse, S. A., *Crystal Identification with the Polarizing Microscope*. Springer US: 1994.
280. Kai Yang, F. H., Ping Cheng, A fully coupled numerical simulation of sessile droplet evaporation using Arbitrary Lagrangian–Eulerian formulation. *International Journal of Heat and Mass Transfer* **2014**, 70, 409.
281. Chen, P.; Harmand, S.; Ouenzerfi, S.; Schiffler, J., Marangoni Flow Induced Evaporation Enhancement on Binary Sessile Drops. *J. Phys. Chem. B* **2017**, 121 (23), 5824-5834.
282. Kaplan, C. N.; Mahadevan, L., Evaporation-driven ring and film deposition from colloidal droplets. *J. Fluid Mech.* **2015**, 781, R2.
283. Kirby, B. J., Chapter 1: Kinematics, conservation equations, and boundary conditions. In *Micro- and Nanoscale Fluid Mechanics: Transport in Microfluidic Devices*, Press, C. U., Ed. Cambridge University Press: New York, 2010.
284. Leal, L. G., *Advanced Transport Phenomena: Fluid Mechanics and Convective Transport Processes*. Cambridge University Press: 2007.
285. Sempels, W.; De Dier, R.; Mizuno, H.; Hofkens, J.; Vermant, J., Auto-production of biosurfactants reverses the coffee ring effect in a bacterial system. *Nat. Commun.* **2013**, 4, 1757.
286. Tatsumi, M.; Teramoto, Y.; Nishio, Y., Different orientation patterns of cellulose nanocrystal films prepared from aqueous suspensions by shearing under evaporation. *Cellulose* **2015**, 22 (5), 2983-2992.

287. Mewis, J.; Wagner, N. J., *Colloidal Suspension Rheology*. Cambridge University Press: 2012.
288. Boluk, Y.; Danumah, C., Analysis of cellulose nanocrystal rod lengths by dynamic light scattering and electron microscopy. *J Nanopart Res* **2014**, *16* (1), 1-7.
289. Hoath, S. D., *Fundamentals of Inkjet Printing: The Science of Inkjet and Droplets*. Wiley: 2016.
290. Capello, C.; Fischer, U.; Hungerbuhler, K., What is a green solvent? A comprehensive framework for the environmental assessment of solvents. *Green Chemistry* **2007**, *9* (9), 927-934.
291. Vazquez, G.; Alvarez, E.; Navaza, J. M., Surface Tension of Alcohol Water + Water from 20 to 50 .degree.C. *Journal of Chemical & Engineering Data* **1995**, *40* (3), 611-614.
292. Horn, F. M.; Richtering, W.; Bergenholtz, J.; Willenbacher, N.; Wagner, N. J., Hydrodynamic and Colloidal Interactions in Concentrated Charge-Stabilized Polymer Dispersions. *Journal of Colloid and Interface Science* **2000**, *225* (1), 166-178.
293. Wagner, N. J., The High-Frequency Shear Modulus of Colloidal Suspensions and the Effects of Hydrodynamic Interactions. *Journal of Colloid and Interface Science* **1993**, *161* (1), 169-181.
294. Shikata, T.; Pearson, D. S., Viscoelastic behavior of concentrated spherical suspensions. *Journal of Rheology* **1994**, *38* (3), 601-616.
295. Bruckner, J. R.; Kuhnhold, A.; Honorato-Rios, C.; Schilling, T.; Lagerwall, J. P. F., Enhancing Self-Assembly in Cellulose Nanocrystal Suspensions Using High-Permittivity Solvents. *Langmuir* **2016**, *32* (38), 9854-9862.
296. D'Avila, S. G.; Silva, R. S. F., Isothermal vapor-liquid equilibrium data by total pressure method. Systems acetaldehyde-ethanol, acetaldehyde-water, and ethanol-water. *Journal of Chemical & Engineering Data* **1970**, *15* (3), 421-424.
297. Beebe, A. H.; Coulter, K. E.; Lindsay, R. A.; Baker, E. M., Equilibria in Ethanol-Water System at Pressures Less Than Atmospheric. *Industrial & Engineering Chemistry* **1942**, *34* (12), 1501-1504.
298. Talbot, E., Bain, C. , De Dier, R. , Sempels, W. and Vermant, J., Droplets Drying on Surfaces. In *Fundamentals of Inkjet Printing*, 2015.
299. Tarek, M.; Tobias, D. J.; Klein, M. L., Molecular dynamics investigation of the surface/bulk equilibrium in an ethanol-water solution. *Journal of the Chemical Society, Faraday Transactions* **1996**, *92* (4), 559-563.
300. Wilson, M. A.; Pohorille, A., Adsorption and Solvation of Ethanol at the Water Liquid-Vapor Interface: A Molecular Dynamics Study. *The Journal of Physical Chemistry B* **1997**, *101* (16), 3130-3135.
301. Routh, A. F.; Zimmerman, W. B., Distribution of particles during solvent evaporation from films. *Chemical Engineering Science* **2004**, *59* (14), 2961-2968.
302. Alexander, F. R., Drying of thin colloidal films. *Reports on Progress in Physics* **2013**, *76* (4), 046603.
303. Talbot, E. L.; Yang, L.; Berson, A.; Bain, C. D., Control of the Particle Distribution in Inkjet Printing through an Evaporation-Driven Sol-Gel Transition. *ACS Appl. Mater. Interfaces* **2014**, *6* (12), 9572-9583.

304. Seo, C.; Jang, D.; Chae, J.; Shin, S., Altering the coffee-ring effect by adding a surfactant-like viscous polymer solution. *Sci. Rep.* **2017**, 7 (1), 500.
305. Cui, L.; Zhang, J.; Zhang, X.; Huang, L.; Wang, Z.; Li, Y.; Gao, H.; Zhu, S.; Wang, T.; Yang, B., Suppression of the Coffee Ring Effect by Hydrosoluble Polymer Additives. *ACS Appl. Mater. Interfaces* **2012**, 4 (5), 2775-2780.
306. Yang, J.; Xu, F.; Han, C.-R., Metal Ion Mediated Cellulose Nanofibrils Transient Network in Covalently Cross-linked Hydrogels: Mechanistic Insight into Morphology and Dynamics. *Biomacromolecules* **2017**, 18 (3), 1019-1028.
307. Gruber, M. F.; Johnson, C. J.; Tang, C. Y.; Jensen, M. H.; Yde, L.; Hélix-Nielsen, C., Computational fluid dynamics simulations of flow and concentration polarization in forward osmosis membrane systems. *J. Membr. Sci.* **2011**, 379 (1), 488-495.
308. Grønbech-Jensen, N.; Mashl, R. J.; Bruinsma, R. F.; Gelbart, W. M., Counterion-Induced Attraction between Rigid Polyelectrolytes. *Physical Review Letters* **1997**, 78 (12), 2477-2480.
309. Bizmark, N.; Ioannidis, M. A., Effects of Ionic Strength on the Colloidal Stability and Interfacial Assembly of Hydrophobic Ethyl Cellulose Nanoparticles. *Langmuir* **2015**, 31 (34), 9282-9289.
310. Singh, K. B.; Bhosale, L. R.; Tirumkudulu, M. S., Cracking in Drying Colloidal Films of Flocculated Dispersions. *Langmuir* **2009**, 25 (8), 4284-4287.
311. Hirai, A.; Inui, O.; Horii, F.; Tsuji, M., Phase Separation Behavior in Aqueous Suspensions of Bacterial Cellulose Nanocrystals Prepared by Sulfuric Acid Treatment. *Langmuir* **2009**, 25 (1), 497-502.
312. Kang, K.; Dhont, J. K. G., Glass Transition in Suspensions of Charged Rods: Structural Arrest and Texture Dynamics. *Phys. Rev. Lett.* **2013**, 110 (1), 015901.
313. Håkansson, K. M. O.; Fall, A. B.; Lundell, F.; Yu, S.; Krywka, C.; Roth, S. V.; Santoro, G.; Kvik, M.; Prahl Wittberg, L.; Wågberg, L.; Söderberg, L. D., Hydrodynamic alignment and assembly of nanofibrils resulting in strong cellulose filaments. *Nat. Commun.* **2014**, 5, 4018.
314. Honorato-Rios, C.; Kuhnhold, A.; Bruckner, J. R.; Dannert, R.; Schilling, T.; Lagerwall, J. P. F., Equilibrium Liquid Crystal Phase Diagrams and Detection of Kinetic Arrest in Cellulose Nanocrystal Suspensions. *Frontiers in Materials* **2016**, 3 (21).
315. Stoiber, R. E.; Morse, S. A., Anisotropic crystals. In *Crystal Identification with the Polarizing Microscope*, Hall, C., Ed. Springer US: 2012; pp 102-115.
316. Gebauer, D.; Oliynyk, V.; Salajkova, M.; Sort, J.; Zhou, Q.; Bergstrom, L.; Salazar-Alvarez, G., A transparent hybrid of nanocrystalline cellulose and amorphous calcium carbonate nanoparticles. *Nanoscale* **2011**, 3 (9), 3563-3566.
317. Xu, F.; Crooker, P. P., Chiral nematic droplets with parallel surface anchoring. *Physical Review E* **1997**, 56 (6), 6853-6860.
318. Basu, S.; Bansal, L.; Miglani, A., Towards universal buckling dynamics in nanocolloidal sessile droplets: the effect of hydrophilic to superhydrophobic substrates and evaporation modes. *Soft Matter* **2016**, 12 (22), 4896-4902.
319. Popov, Y. O., Evaporative deposition patterns: Spatial dimensions of the deposit. *Physical Review E* **2005**, 71 (3), 036313.

320. Tsapis, N.; Dufresne, E. R.; Sinha, S. S.; Riera, C. S.; Hutchinson, J. W.; Mahadevan, L.; Weitz, D. A., Onset of Buckling in Drying Droplets of Colloidal Suspensions. *Physical Review Letters* **2005**, *94* (1), 018302.
321. Pauchard, L.; Allain, C., Mechanical instability induced by complex liquid desiccation. *Comptes Rendus Physique* **2003**, *4* (2), 231-239.
322. Pauchard, L.; Couder, Y., Invagination during the collapse of an inhomogeneous spheroidal shell. *EPL (Europhysics Letters)* **2004**, *66* (5), 667.
323. Palmer, S. J., The effect of temperature on surface tension. *Physics Education* **1976**, *11* (2), 119.
324. Tam, D.; von Arnim, V.; McKinley, G. H.; Hosoi, A. E., Marangoni convection in droplets on superhydrophobic surfaces. *Journal of Fluid Mechanics* **2009**, *624*, 101-123.
325. Gittens, G. J., Variation of surface tension of water with temperature. *Journal of Colloid and Interface Science* **1969**, *30* (3), 406-412.
326. Pradhan, T. K.; Panigrahi, P. K., Evaporation induced natural convection inside a droplet of aqueous solution placed on a superhydrophobic surface. *Colloids and Surfaces A: Physicochemical and Engineering Aspects* **2017**, *530*, 1-12.
327. Hoeng, F.; Bras, J.; Gicquel, E.; Krosnicki, G.; Denneulin, A., Inkjet printing of nanocellulose-silver ink onto nanocellulose coated cardboard. *RSC Advances* **2017**, *7* (25), 15372-15381.
328. Chinga-Carrasco, G., Potential and Limitations of Nanocelluloses as Components in Biocomposite Inks for Three-Dimensional Bioprinting and for Biomedical Devices. *Biomacromolecules* **2018**, *19* (3), 701-711.
329. Linge Johnsen, S. A.; Bollmann, J.; Lee, H. W.; Zhou, Y., Accurate representation of interference colours (Michel-Lévy chart): from rendering to image colour correction. *Journal of Microscopy* **2017**, *269* (3), 321-337.
330. Plawsky, J. L., *Transport Phenomena Fundamentals*. Taylor & Francis: 2001.

Curriculum Vitae

Alican GENÇER

genceralican@gmail.com

Education

Ph.D. in Chemistry	KU Leuven	2014-2018
M.Sc. in Chemistry	KU Leuven	2012-2014
B.Sc. in Chemistry	Boğaziçi University	2007-2012
Erasmus Exchange	Ghent University	2011

Research Visits

X-ray scattering measurements	European Synchrotron Radiation Facility	November 2016
DDLS measurements	Forschungszentrum Jülich	May 2017

Extra-Curricular Activities & Internships

Representative Interdisciplinary Research Facility	Kulak, Kortrijk, Belgium	2017-2018
Student Leader	Sint Jans Community House, Leuven, Belgium	2012-2013
Intern at R&D	Gülçiçek Int. Fragrance, Istanbul, Turkey	2010
Quality Controller	Bilim Pharmaceuticals, Istanbul, Turkey	2010
Representative School of Foreign Language	Boğaziçi University, Istanbul, Turkey	2007-2008

List of Publications

International Publications

- Gençer, A.; Schütz, C.; Thielemans, W., Influence of the Particle Concentration and Marangoni Flow on the Formation of Cellulose Nanocrystal Films. *Langmuir* 2017, 33 (1), 228-234
- Gençer, A.; Van Rie, J.; Lombardo, S.; Kang, K.; Thielemans, W., Effect of Gelation on the Colloidal Deposition of Cellulose Nanocrystal Films. *Biomacromolecules* 2018, 19 (8), 3233-3243
- Schütz, C.; Van Rie, J.; Eyley, S.; Gençer, A.; van Gorp, H.; Rosenfeldt, S.; Kang, K.; Thielemans, W., Effect of Source on the Properties and Behavior of Cellulose Nanocrystal Suspensions. *ACS Sustainable Chemistry & Engineering* 2018, 6 (7), 8317-8324
- Van Rie, J.; Schütz, C.; Gençer, A.; Lombardo, S.; Kang, K.; Thielemans, W., Anisotropic Diffusion and Phase Behavior of Cellulose Nanocrystal Suspensions. *Langmuir*, Submitted.

Communications at International Conferences and Symposia

- Influence of the Particle Concentration and Marangoni Flow on the Formation of Cellulose Nanocrystal Films, Poster presentation at Cellulosic materials - processing, properties and promising applications working groups, Budapest, Hungary (September 22-23, 2016)
- Influence of the Particle Concentration and Marangoni Flow on the Formation of Cellulose Nanocrystal Films, Poster presentation at Twisted conference, University of Luxemburg (May 10-12, 2017)
- Control of the Deposition and the Optical Properties of Cellulose Nanocrystal Films, Oral presentation at “Cellulosic material properties and industrial potential –COST FP1205” in Stockholm, Sweden (7-9 March 2017) and at UK Colloids 2017 in Manchester, UK (10-12 July 2017)
- Control of the Colloidal Deposition of Cellulose Nanocrystal Films towards Photonic Crystal Applications, Oral presentation at Chemical Research in Flanders – CRF (24-26 October 2016) and ChemCYS in Belgium (21-23 February 2018)